공학박사 학위논문

Fundamental Study on the Mechanism of High Temperature Oxidation and Cr Evaporation Behavior of SOFC Interconnect Materials

SOFC 금속 분리판 재료의 고온 산화 및 Cr 휘발 거동 근원적 기구에 대한 연구

2018 년 2 월

서울대학교 대학원

재료공학부

김 병 규

Fundamental Study on the Mechanism of High Temperature Oxidation and Cr Evaporation Behavior of SOFC Interconnect Materials

SOFC 금속 분리판 재료의 고온 산화 및 Cr 휘발 거동 근원적 기구에 대한 연구

지도교수 이 경 우

이 논문을 공학박사 학위논문으로 제출함
2018 년 2 월

서울대학교 대학원
재료공학부
김병규

김병규의 박사 학위논문을 인준함
2017 년 12 월

위 원 장	김 영 운	(인)
부 위 원 장	이 경 우	(인)
위 원	한 흥 남	(인)
위 원	서 진 유	(인)
위 원	김 동 익	(인)

Abstract

Fundamental Study on the Mechanism of High Temperature Oxidation and Cr Evaporation Behavior of SOFC Interconnect Materials

Byung Kyu Kim

Department of Materials Science and Engineering

The Graduate School

Seoul National University

A fuel cell is the device that converts electrochemical energy into electrical energy *via* electrochemical processes using hydrogen containing fuel and oxygen or other oxidants. Among various types of fuel cells, a solid oxide fuel cell (SOFC) is classified as one of the high temperature fuel cell due to its high operating temperature in the range of 700 to 1000 ºC.

To generate a required power output, a single SOFC cell is combined to form a stack separated by either ceramic or metallic interconnects. New Fe-base alloy design featuring a high Cr content (> 23 wt. %) was introduced and commercialized by ThyssenKrupp specifically for SOFC application. Due to the high operating temperature, oxidation and subsequent Cr evaporation phenomena are directly associated with long-term stability and thus the commercialization of the SOFC. Therefore, the author attempted to enhance not only the oxidation resistance of the commercial interconnect material but also to suppress its Cr evaporation, adopting two different approaches: a metallurgical method and surface modification.

In the first part, the effect of alloy grain size on oxidation behavior was investigated using a sheet (t = 2 mm) and plate (t = 22 mm) of commercial high Cr ferritic stainless steel. The weight gain tests were conducted at 800 ºC in air + 2 % H_2O which simulated the atmosphere of a SOFC cathodic side. The average grain size of the sheet and plate specimen was measured as ~ 25 μm and ~ 500 μm, respectively. The plate specimen showed the reduced oxidation rate by 30 % compared to the sheet specimen. Such difference was mainly attributed to the grain boundary (GB) of the alloy which acts as a preferential reaction site for penetrating intergranular oxide. Fast metal and oxygen diffusion along the GBs formed relatively thick outer oxide scales and microscale intergranular oxides, consequently augmenting the oxidation rate. The crystallization of the internal intergranular oxide was accompanied with the protrusion of surrounding alloy relieved by a surface ridge. The aim of the first part of this study is to understand the oxidation behavior of high Cr ferritic stainless steel by relating it with the inhomogeneous oxidation phenomena at the alloy GB. Furthermore, the formation of intergranular oxidation is discussed in terms of thermodynamic stability dependent on varying oxygen partial pressure.

In the second part, Co electrodeposition was adopted to address the Cr evaporation issue of the commercial metallic interconnect material under the SOFC cathodic condition at an operating temperature of 800 ºC. The electroplated Co layer with a thickness of 400 nm decreased the Cr release from high Cr ferritic stainless steel by one order of magnitude. In-depth microstructure analysis was carried out to understand the root cause of the evaporation reduction (primary reduction) and governing mechanism accounting for the evaporation behavior change (secondary reduction) of the coated sample. The reduction of Cr release was primarily ascribed to the rapid phase transformation of Co to Co_3O_4 which prevented Cr_2O_3 from direct exposure to oxidants. The time sequential oxide characterization for the coated sample showed that the complete phase transformation of Co_3O_4 to $Mn_xCo_{3-x}O_4$

occurred through dominant Mn diffusion in the Co oxide layer. The post-processed TEM compositional map revealed the presence of the Cr affected fringes in the vicinity of the GBs of the Co oxide which completely diminished at the end of oxidation. On the basis of such findings, the second part of this study proposes the underlying mechanism for the overall oxidation and associated Cr evaporation process of the Co coated sample in light of the cation diffusion scheme and gas mass transport.

Keywords : ferritic stainless steel, solid oxide fuel cell, metallic interconnect, Cr evaporation, high temperature oxidation, grain size effect, oxide characterization

Student Number : 2012-30154

Table of Contents

List of Figures

List of Tables

Chapter 1.

Introduction

A fuel cell is the device that converts electrochemical energy into electrical energy *via* electrochemical processes using hydrogen containing fuel and oxygen or other oxidants. Among various types of fuel cells, a solid oxide fuel cell (SOFC) has the advantages of flexible fuel selection and high efficiency, and has no need of fuel reformers, which allows it to be developed as a combined cycle system.

To generate a required power output, a single SOFC cell is combined to form a stack separated by either ceramic or metallic interconnects, the two main roles of which are to act as the physical barrier and electrical connector. Use of metallic interconnects for an electrode-supported type SOFC has been enabled as the operating temperature of SOFC was reduced to a range of 600 to 800 °C [1, 2]. Nonetheless, the modified temperature range is still high enough to change the surface state of a metallic interconnect, which has a considerable impact on overall cell efficiency and long-term stability

Assessment of the alloys of various materials in former comprehensive studies showed that chromia (Cr_2O_3) forming alloys (Cr- or Fe-base) are the most adoptable candidate for SOFC application from the perspective of technical requirements: electrical conductivity, easy fabrication, coefficient of thermal expansion (CTE), and material cost [2-4]. For the sake of economic feasibility and easy fabrication, the Fe-based alloys have been provisionally concluded as the desirable choice for SOFC application under 1000 °C [5].

1.1 Metallurgical approach

In the early stage of the development of interconnect materials for SOFCs, a focus was mainly put on the family of complex ceramic oxide with perovskite structure (e.g. doped lanthanum chromite, $La_xSr_{1-x}CrO_3$) [1, 2]. Such ceramic based interconnects were intended for usage in electrolyte-supported planar type SOFCs which operate in the temperature range above 1000 °C. However, the high cost of raw material, difficulties of fabrication and instability of chromite in reducing atmospheres deter the commercialization of SOFCs [3]. With the advent of the electrode-supported planar type SOFC with thin electrolyte (5 ~ 20 μm) [2, 4, 5] and new electrolyte (e.g. doped lanthanum gallate, $LaGaO_3$) with enhanced conductivity [6, 7], its operating temperature could be reduced to the range of 600 ~ 800 °C, expanding the span of material selection to metals instead of ceramics.

The development of metallic interconnects used for SOFCs has been one of the main issues for material scientists and metallurgists for the two last decade [8-10]. The heat-resistant metallic alloys considered for the selection can be normally classified according to their base metals: Ni, Cr, Co, and Fe. Of the 4 bases, Fe based stainless steels are currently considered the most viable candidate due to low material cost, and easier fabrication (better machinability and weldability), good thermal expansion coefficient (11×10^{-6} °C^{-1}) matching other ceramic components ($9 \sim 23 \times 10^{-6}$ °C^{-1}) [8], and better thermal and electrical conductivities.

High temperature oxidation resistance of metallic interconnects has been regarded as one of the main technical requirements for the following reasons. The electrical loss of interconnect materials has been commonly evaluated by area specific resistance that is proportional to thickness of an oxide layer (i.e. oxidation rate) [10, 11]. Also, according to the life prediction based on stress analysis, the critical oxide layer thickness tolerable until spallation was estimated around 11 μm, which would

be reached after a lifetime of 5000 h under the typical SOFC condition at 800 ºC [12]. This previous work adduces that retardation of inevitable oxidation must be accomplished to secure the long-term performance of a SOFC stack including Fe-base interconnect materials

The simple metallurgical solution for improving oxidation resistance of certain alloys is to vary grain size of the alloys. This is because alloy GBs have been known as a rapid diffusion path for cation and anion [13]. The effect of alloy grain size on oxidation kinetics exhibit an inconsistent trend depending on which system alloy belongs to. In case of austenitic stainless steel [14-16], large alloy grain size was found to compromise oxidation resistance while the contrary effect was reported for low Cr ferritic steel [17, 18] and Al containing 18Cr ferritic stainless steel [19]. Therefore, it is considered worthwhile assessing the effect of alloy grain size on oxidation behavior specifically for commercial Crofer22 APU.

Of the numerous oxidation studies specifically pertinent to Crofer22 APU [20-25], to the author's best knowledge, only one research group published the study addressing the effect of alloy grain size on the log-term oxidation of Croferr22 APU [23]. They discovered that the oxidation rate of Crofer22 APU oxidized in static air at 800 °C decreased with increasing alloy grain size, which is in good agreement with the author's finding. Their elucidation for the phenomenon, however, rests on different oxidation behavior (e.g. oxide morphology) of intragranular regions of the alloy. In contrary, the present study gives more weight to oxidation behavior associated with GB regions of the alloy in an attempt to reason out the root cause of the reduction in oxidation kinetics.

This study presents the influence of alloy grain size on the oxidation of Crofer22 APU employing a weight gain test followed by multiscale microstructure analysis. Additionally, the oxygen partial pressures corresponding to the observed oxides are predicted in light of thermodynamics to offer a theoretical base relevant to the

oxidation of Crofer22 APU. As stated, the author puts the primary focus on the intergranular oxidation phenomena in order to assert that the GB of Crofer22 APU be detrimental to oxidation resistance.

1.2 Surface modification

Use of metallic interconnects for an anode-support type SOFC has been enabled as the operating temperature of SOFC was reduced to a range of 600 to 800 °C [2, 5]. However, the modified temperature range still gives rise to changes in the surface state of a metallic interconnect, which considerably affects overall cell efficiency and long-term stability. Assessment of the alloys of various materials in former comprehensive studies showed that chromia (Cr_2O_3) forming alloys (Cr- or Fe-base) are the most adoptable candidate for SOFC application from the perspective of technical requirements: electrical conductivity, easy fabrication, coefficient of thermal expansion (CTE) matching, and material cost [2, 8, 9]. For the sake of economic feasibility and easy fabrication, the Fe-based alloys have been provisionally concluded as the desirable choice for SOFC application under 1000 °C [26].

The commercially available Fe-base alloys for SOFC interconnects are best characterized as ferritic stainless steel alloyed with a Cr content greater than 20 wt. % to form a protective Cr-rich oxide layer and, thereby, secure high temperature oxidation resistance. Nevertheless, the Cr_2O_3 layer reacts to supply gas (O_2 and H_2O), especially at the cathodic side, and produces gaseous hexavalent Cr in the compound form of CrO_3 and $CrO_2(OH)_2$ [27, 28] which are potentially detrimental to overall cell efficiency [29-33] and structural integrity [34].

The Cr evaporation issue can be treated by modification of either alloy composition or surface states. The latter is more essential according to Stanislowski et al. who quantified the Cr release from the various commercially available Ni-, Cr-, and Fe-base alloys and revealed that the Cr-dominant oxide formers cannot be free from Cr evaporation without surface modification [35, 36]. Co has been known as one of the most promising coating materials transformable into single or complex spinel oxide.

Surface modification using Co spinel oxides, such as Co_3O_4 or $(Co,Mn)_3O_4$, was found to be beneficial to oxidation resistance [37-41]. Moreover, the oxides themselves possess relatively high electrical conductivities (6.7 and 60 $S \cdot cm^{-1}$) and appropriate values of CTEs (9.3 and 9.6 $\times 10^{-6}$ $°C^{-1}$) compatible with those of both Cr_2O_3 (9.6 $\times 10^{-6}$ $°C^{-1}$) and ferritic stainless steels (11 $\times 10^{-6}$ $°C^{-1}$) [26, 42].

The methodology of surface modification and its effects on interconnect and cell properties have been the main subject of the numerous recent papers over the last few years. The methods relevant to Co coating include physical vapor deposition [43-45], spray and screen printing [37, 46-48], sol-gel coating [41], magnetron sputtering [36, 49, 50], plasma spray [37, 51], pack cementation [38, 40], and electroplating followed by subsequent heat treatments [52-56]. Among the various coating methods mentioned above, DC pulse electroplating for Co coating draws our attention due to its cost-effectiveness, simple process and suitability for coating an interconnect of complex design [56].

In most of the aforementioned studies, the coating methodology itself was given more weight and the effectiveness of coating was explored mainly in terms of oxidation resistivity or electrical conductivity (area specific resistance). A few did sufficiently provide fair quantitative evaluations on Cr evaporation to prove the Cr retention capability of spinel Co oxide. However, those studies seem to be somewhat technically oriented in that they hardly dealt with the change in evaporation kinetics and underlying mechanism of the unavoidable Cr evaporation from the coated materials. To better reflect actual phenomena, it will be worthwhile to lay emphasis on the fundamental origin of the inevitable Cr evaporation from the coated interconnect materials.

The aims of Part B are to show the effect of Co electroplating on the Cr evaporation of the stainless steel interconnect material and to discover the correlation between its oxidation behavior and Cr evaporation kinetics. To investigate the oxide evolution

of the Co coated specimen, the characterizations on the oxide layers were performed by diverse microstructural analysis methods: scanning electron microscopy (SEM), energy dispersive X-ray spectrometry (EDS), electron backscattered diffraction (EBSD), and transmission electron microscopy (TEM). On the basis of these microstructural observations, linked with the consideration of gas phase mass transport, the present study will discuss the behavior of the evaporation kinetics change of the Co coated interconnect materials.

Chapter 2.

Theoretical and technical background

2.1 Mechanism of oxidation

The formation of oxide films or scales results from high temperature oxidation of metals under most conditions. The nature of oxide determines the mechanisms of oxidation weather it is liquid or solid with or without partial evaporation of the oxide. When oxide is solid, its oxidation behavior is also dependent on the degree of compactness, or porosity. If the scale is compact enough to act as a diffusion barrier, i.e. the scale is continuous separating the parental alloy and gaseous oxidation, the rate of oxidation will be mainly limited by a solid-state diffusion through a compact oxide scale. This implies that the growth phenomena of the oxide scale will slow down with increasing scale thickness and oxidation time. Therefore, from an industrial point of view, the formation of the compact, continuous oxide scale on the metal surface is most targeted for best oxidation resistance.

2.1.1 Oxidation rates

When an oxidation reaction proceeds as shown below

$$\frac{x}{y}M + \frac{1}{2}O_2 \rightarrow \frac{1}{y}M_xO_y \tag{2.1}$$

it follows a kinetic rate law

$$\frac{d\xi}{dt} = f(t) \tag{2.2}$$

where ξ is a measure of the extent of reaction at time, *t*. Thus,

$$d\xi = dn_{M_xO_y} = -\frac{dn_m}{x} = -\frac{2dn_{O_2}}{y} \tag{2.3}$$

where n_i is the number of moles of the species, *i*. Now, *f(t)* needs to be determined in a quantitative form [57]. Several techniques are available for assessing the oxidation reaction kinetics as described in [58]. By far, the measurement of weight accumulation with time is considered the most common technique. The measurement can be done by both continuously and discontinuously. Continuous assessment is performed gravimetrically with a microbalance while discontinuous weighing of a series of samples is also practicable. However, when *t* is very small, it is highly recommended to use a high-quality microbalance for measurement precision [57].

2.1.2 Rate equations

The most common rate equations are classified as logarithmic, linear and parabolic.

Logarithmic rate equation

Logarithmic rate equations represents the oxidation of metals at low temperatures generally below 300 ~ 400 °C. This rate is observed when the initial oxidation reaction (up to the 100 nm range [8]) proceeds rapidly, followed by a drop in the rate to a small value. The graphical presentation of the logarithmic rate equations is given in Fig. 2.1 a). This behavior follows the direct logarithmic or inverse logarithmic rate equation as shown below [9].

$$\text{Direct logarithmic: } x = k_{log} \log(t + t_0) + A \tag{2.4}$$

$$\text{Inverse logarithmic: } \frac{1}{x} = B - k_{il} \log(t) \tag{2.5}$$

where x may denote the amount of oxygen consumed per unit surface, metal transformed to oxide, or thickness of the oxide layer, t denotes the time, and k denotes the rate constant. Although the logarithmic rate equation generically represent the oxidation of metal at low temperature, one who studies the high temperature oxidation needs to grasp the logarithmic behavior, since the behavior may be encountered during the heating period of the oxidation process at high temperature.

A number of rate-determining mechanisms has been suggested to interpret the logarithmic oxidation behavior. The mechanisms include the adsorption of reactive species, the effects of electric fields developed across oxide layers, quantum mechanical tunneling of electrons through the thin scales, progressive blocking of low resistance diffusion paths (pores or cavities), non-isothermal conditions in the oxide layer, and nucleation and growth processes [58]. The details of the theories

based on the above mechanisms will not be addressed here. One may refer to the concise summary written by Kofstad for understanding of different mechanisms [59].

Linear rate equation

The rate of linear oxidation is constant so it can be described by

$$x = k_l t \tag{2.6}$$

where x is the scale thickness and k_l is the linear rate constant.

The condition leading to the linear oxidation is that the phase boundary (gas-oxide or oxide-metal) reaction is a rate-determining step in the oxidation process. For instance, the overall reaction may be governed by the adsorption of oxidants at the gas-oxide interface or a steady-state formation of oxide at oxide-metal interface. In either case, the formation of cavities of pores by nature or rupture of a compact scale due to stress development result in the above phenomena. If the size of pores is larger than the mean free path of gas molecules, the transport of metal and non-metal through the oxide scale is no longer rate-determining and, hence, scale thickness does not reflect the actual oxidation rate.

Pilling and Bedworth put forward the condition where protective oxide scales are likely to form [60]. The condition indicated in terms of "Pilling-Bedworth ratio" can be expressed as

$$\frac{V_{OX}}{xV_M} \tag{2.7}$$

where V_i is the molar volume of the indicated species. If the ratio is larger than 1, the oxide will be protective. By the criterion, all the metals, except for alkali and alkaline earth metals, should form compact and protective oxide. In fact, the above criteria has a very limited applicability due to many exceptions concisely summarized by Kofstad [59]. The volume difference of metal and oxide is, therefore, one of the many factors which determines the protectiveness of the metal oxide.

The alloy mainly investigated in this study forms a very compact and protective oxide layer; therefore, the phase boundary reaction relevant to the pores inside the oxide scale or at oxide-metal interface is of minor importance. It would rather be practical and instructive to address the gas adsorption process at the gas-oxide interface because it is likely to be late limiting in the very initial stage of oxidation.

The reaction process at the gas-oxide interface consists of several sub-steps. Reactant gas molecules (e.g. O_2) first impinge onto a metal surface, followed by physical adsorption. Then, the molecules dissociate to single oxygen which becomes chemisorbed by attracting electrons from the oxide. Finally, the chemisorbed oxygen is incorporated to frame the oxygen sub-lattice. The whole process can be described below [58].

$$\frac{1}{2}O_2(g) \rightarrow \frac{1}{2}O_2(ad.) \rightarrow O(ad.) \overset{e^-}{\rightarrow} O^-(chem.) \overset{e^-}{\rightarrow} O^{2-}(latt.) \quad (2.8)$$

The condition for the adsorption process to be rate-governing requires sufficiently low oxygen pressure or high temperature [58, 59]. Therefore, it can be assumed that the above process occurs very rapidly in the initial stage of oxidation under the condition used in this study. For a more detailed review of physical adsorption and adsorption equilibria linked to oxidation, one is recommended to consult with Kofstad [59].

The chemisorption step may become rate-limiting when oxidation occurs in a mixture of CO/CO_2 gas. The surface reactions with the oxidizing medium in the CO/CO_2 gas mixture are [58]

$$CO_2(g) \rightarrow CO_2(ad.) \rightarrow \underbrace{CO(ad.)}_{CO(g)} + \overbrace{\underbrace{O(ad.)}_{CO_2(g)}}^{CO(g)} \xrightarrow{e^-} \\ O^-(chem.) \xrightarrow{e^-} O^{2-}(latt.) \tag{2.9}$$

According to Hauffe and Pfeiffer who conducted the oxidation of iron in CO/CO_2 mixtures between 900 and 1000 °C, chemisorption of oxygen is likely to be rate-governing since the rate was constant and proportional to $\left(p_{CO_2}/p_{CO}\right)^{2/3}$ [61]. However, the result of the experiment performed by Pettit et al. under the same condition above shows that the dissociation of CO_2 (ad.) to CO (ad.) and O (ad.) is the rate-governing step [62].

Parabolic rate equation

The oxidation of many metals at high temperature follows a parabolic time dependence as shown in Fig. 2.1 b). The rate-determining step of the parabolic oxidation behavior is a thermal diffusion process through the oxide layer. For the case that cation transport dominantly controls the growth of the oxide layer with thermodynamic equilibrium established at each interface, the process can be simply treated as follows. The outward cation flux ($j_{M^{2+}}$), equal to the inward flux of cation vacancies (j_{V_M}), is expressed by Fick's first law as

$$j_{M^{2+}} = -j_{V_M} = D_{V_M} \frac{C''_{V_M} - C'_{V_M}}{x} \tag{2.10}$$

where x is the oxide thickness, D_{V_M} is the diffusion coefficient for cation vacancies, and C'_{V_M} and C''_{V_M} is the vacancy concentration at the scale-metal and scale-gas interface, respectively. Due to thermodynamic equilibrium at each interface, ΔC_{V_M} is maintained at a constant level. Then, Eq. (2.10) can be expressed as

$$j_{M^{2+}} = \frac{1}{V_{OX}}\frac{dx}{dt} = D_{V_M}\frac{C''_{V_M} - C'_{V_M}}{x} \tag{2.11}$$

$$\frac{dx}{dt} = D_{V_M}\frac{C''_{V_M} - C'_{V_M}}{x} = \frac{k'}{x} \tag{2.12}$$

where dx/dt is the growth rate of the oxide thickness, V_{OX} is the molar volume of the oxide. Integrating Eq. (2.12) gives the common parabolic rate law as

$$x^2 = 2k'_p t + c_p \tag{2.13}$$

where k_p is the rate constant and c_p the integration constant when $x = 0$ at $t = 0$.

a)

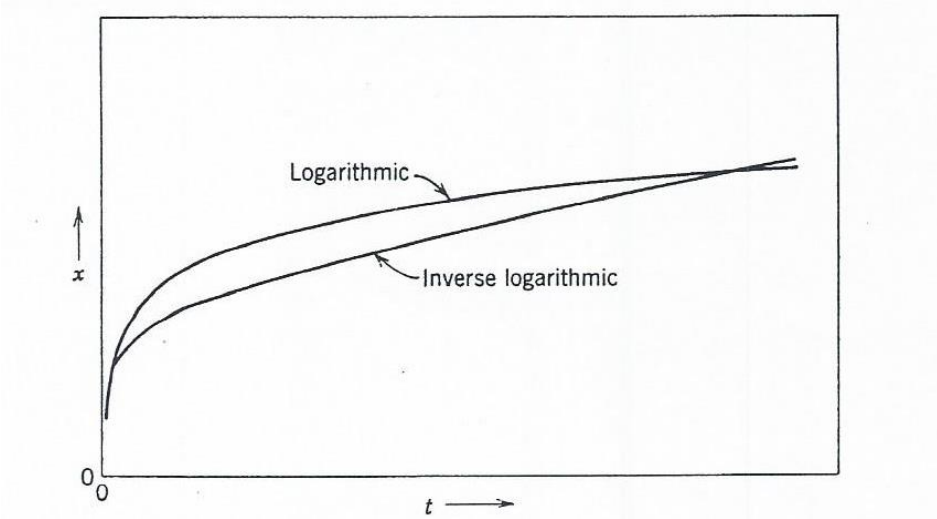

b)

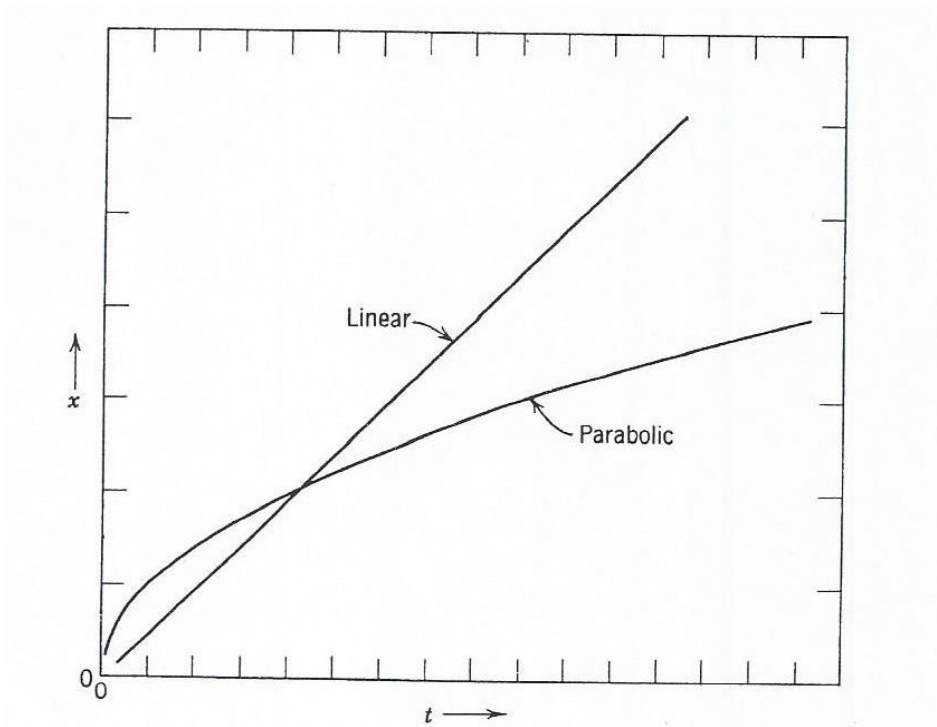

Fig. 2.1. Graphical presentation of the oxidation rate equations [59]: (a) direct logarithmic and inverse logarithmic rate equation and (b) linear and parabolic rate equation.

2.1.3 Wagner oxidation theory

To better understand the parabolic oxidation behavior at high temperature, Wagner developed the theory, namely, "Wagner theory", which has been most widely applied up to date [63]. Even though the theory assumes highly idealized conditions and describes the case where the diffusion of cations or anions is a rate-determining step, it still provides the theoretical basis for enhancing the high temperature oxidation resistance of metals

According to Birks et al. [58], the assumptions which validate the Wagner theory are as follows:

- The oxide layer is a compact and perfectly adherent scale.
- Migration of ions or electrons across the scale is rate controlling
- Thermodynamic equilibrium is established at both the metal0scale and scale0gas interfaces.
- The oxide scale shows only small deviations from stoichiometry and, hence, the ionic fluxes are independent of position within the scale
- Thermodynamic equilibrium is established locally throughout the scale.
- The scale is thick compared with the distances over which space charge effects (electrical double layer) occur.
- Oxygen solubility in the metal may be neglected.

Fig. 2.2 illustrates the thermodynamic equilibrium established at the metal-oxide and oxide-gas interfaces. The volume diffusion of the reacting ions or corresponding point defects is assumed to occur in an opposite direction along with the activity gradients of the metal and non-metal established across the growing oxide layer. See Fig. 2.2 a) [58]. In Fig. 2.2 b) and c), the concentration gradient of metal and non-metal ion vacancies and transport process are illustrated for metal deficit and non-

metal deficit oxide, respectively [59]. For the metal deficit oxide, the defect equilibrium is

$$\frac{1}{2}O_2 = MO + V_M^{p-} + ph^{\cdot} \tag{2.14}$$

For non-metal deficit oxide, the defect equilibrium is

$$O_O = V_O^{q+} + qe^- + \frac{1}{2}O_2 \tag{2.15}$$

For the metal deficit oxide, the metal vacancies are continuously formed at the oxide-gas interface while consumed at the metal-oxide interface and vice versa for the non-metal deficit oxide.

Understanding of Wagner oxidation theory

The diffusion of charged ions and electrons across the oxide layer is influenced by both chemical and electrical potential gradients providing the net driving force for ion migration. The flux of particles carrying a charge, Z_i, responding to the chemical potential gradient, $\frac{\partial \mu_i}{\partial x}$, and electrical potential gradient, $\frac{\partial \phi}{\partial x}$, can be obtained as

$$j_i = C_i v_i = -\frac{C_i B_i}{N_A}\left(\frac{\partial \mu_i}{\partial x} + Z_i F \frac{\partial \phi}{\partial x}\right) \text{ mol cm}^{-2}\text{s}^{-1} \tag{2.16}$$

where C_i is the concentration of particle, i, and B_i is the particle mobility defined as the average drift velocity per unit force, N_A is Avogadro's number and F is the Faraday constant.

The mobility may be related to the conductivity, κ_i, and the self-diffusion coefficient, D_i. The relationships are

$$k_B T B_i = D_i \frac{RT\kappa_i}{C_i (Z_i F)^2} \tag{2.17}$$

where k_B is Boltzmann's constant. Combining Eq. (2.16) and (2.17) gives

$$j_i = -\frac{\kappa_i}{Z_i^2 F^2}\left(\frac{\partial \mu_i}{\partial x} + Z_i F \frac{\partial \phi}{\partial x}\right) \tag{2.18}$$

Eq. (2.18) describes the flux of cations, anions, or electrons across the oxide layer. Due to their different motilities, different species would tend to migrate at different rates. However, consequent electric fields would be set up, opposed to this independence. In fact, the migration rates of the three species are defined by the necessity of maintaining electroneutrality such that no net charge across the oxide scale exists. When the mobility of electrons and electronic defects is very high, such condition can be obtained.

In the majority of oxides and sulphides with high electronic mobility, the motilities of the cations and anions would differ by several orders of magnitude; therefore, the migration of the ionic species with low mobility can be neglected to simplify the treatment [58]. When cations and electrons are the major mobile species, one can express the respective fluxes as

$$j_c = -\frac{\kappa_c}{Z_c^2 F^2}\left(\frac{\partial \mu_c}{\partial x} + Z_c F \frac{\partial \phi}{\partial x}\right) \tag{2.19}$$

$$j_e = -\frac{\kappa_e}{Z_e^2 F^2}\left(\frac{\partial \mu_e}{\partial x} + Z_e F \frac{\partial \phi}{\partial x}\right) \tag{2.20}$$

Electroneutrally is maintained as

$$Z_c j_c + Z_e j_e = 0 \tag{2.21}$$

Substituting Eq. (2.19) and (2.20) into Eq. (2.21) and solving the subsequent equation for $\frac{\partial \phi}{\partial x}$ yields

$$\frac{\partial \phi}{\partial x} = -\frac{1}{F(\kappa_c + \kappa_e)}\left[\frac{\kappa_c}{Z_c}\frac{\partial \mu_c}{\partial x} + \frac{\kappa_e}{Z_e}\frac{\partial \mu_e}{\partial x}\right] \tag{2.22}$$

Using Eq. (2.19) and (2.22), one can eliminate $\frac{\partial \phi}{\partial x}$ to define the flux of cations as

$$j_c = -\frac{\kappa_c \kappa_e}{Z_c^2 F^2(\kappa_c + \kappa_e)}\left[\frac{\partial \mu_c}{\partial x} - \frac{Z_c}{Z_e}\frac{\partial \phi}{\partial x}\right] \tag{2.23}$$

Since Z_e is equal to -1,

$$j_c = -\frac{\kappa_c \kappa_e}{Z_c^2 F^2(\kappa_c + \kappa_e)}\left[\frac{\partial \mu_c}{\partial x} + Z_c\frac{\partial \phi}{\partial x}\right] \tag{2.24}$$

The local chemical reactions taking place in each element of volume of the oxide are considered near enough to equilibrium to utilize the equations of equilibrium thermodynamics. Due to the concentration gradients in the growing oxide, the variation of the concentration of each species does exist. Therefore, equilibrium is assumed to have local relations. Assuming that neutral metal atoms and non-metal atoms react to from neutral oxide, one can use the Gibbs-Duhem relations from

equilibrium thermodynamics. The ionization of the neutral metal atom, M, is written as

$$M = M^{Z_c+} + Z_c e \tag{2.25}$$

At equilibrium, one has the following relation

$$\mu_M = \mu_c + Z_c \mu_e \tag{2.26}$$

From Eq. (2.26), Eq. (2.24) reduces to

$$j_c = -\frac{\kappa_c \kappa_e}{Z_c^2 F^2 (\kappa_c + \kappa_e)} \frac{\partial \mu_M}{\partial x} \tag{2.27}$$

Since κ_c, κ_c, and $\frac{\partial \mu_M}{\partial x}$ in Eq. (2.27) are position-dependent values and thus cannot be readily computed within the theory, Eq. (2.27) needs to be defined in terms of scale thickness and measurable quantities. If j_c leads to no local change in the concentration of cations within the oxide layer, or only marginal stoichiometric deviations, then j_c becomes independent of the position, x. In this case, the integration of j_c from 0 to x gives

$$j_c \int_0^x dx = -\frac{1}{Z_c^2 F^2} \int_{\mu_M'}^{\mu_M''} \frac{\kappa_c \kappa_e}{\kappa_c + \kappa_e} d\mu_M \tag{2.28}$$

$$j_c = -\frac{1}{Z_c^2 F^2 x} \int_{\mu_M'}^{\mu_M''} \frac{\kappa_c \kappa_e}{\kappa_c + \kappa_e} d\mu_M \text{ mol cm}^{-2}\text{s}^{-1} \tag{2.29}$$

According to Fick's fisrt law, the flux of cations may also be defined as

$$j_c = C_M \frac{dx}{dt} \tag{2.30}$$

where C_M is the concentration of metal in the oxide in mol cm^{-3}. Eq. (2.12) shows that the parabolic constant, *k'*, is defined as $\frac{xdx}{dt}$. By comparing Eq. (2.28), (2.29) and (2.30), one can solve them for the parabolic constant which is

$$k' = -\frac{1}{Z_c^2 F^2 C_M} \int_{\mu_M'}^{\mu_M''} \frac{\kappa_c \kappa_e}{\kappa_c + \kappa_e} d\mu_M \tag{2.31}$$

When anions have higher mobility than cations, the parabolic constant may also be defined as

$$k' = -\frac{1}{Z_a^2 F^2 C_X} \int_{\mu_X'}^{\mu_X''} \frac{\kappa_a \kappa_e}{\kappa_a + \kappa_e} d\mu_X \tag{2.32}$$

The transport number of electrons or electron defects is found to be close to unity and the transport number of cations or anions are negligibly small compared to that of electrons or electron defects [58]. Hence,

$$k' = -\frac{1}{Z_c^2 F^2 C_M} \int_{\mu_M'}^{\mu_M''} \kappa_c \, d\mu_M \tag{2.33}$$

$$k' = -\frac{1}{Z_a^2 F^2 C_X} \int_{\mu_X'}^{\mu_X''} \kappa_a \, d\mu_X \tag{2.34}$$

Using Eq. (2.17), Eq. (2.33) and (2.34) is converted to

$$k' = -\frac{1}{RT}\int_{\mu'_M}^{\mu''_M} \mathrm{D}_M \, d\mu_M \tag{2.35}$$

$$k' = -\frac{1}{RT}\int_{\mu'_X}^{\mu''_X} \mathrm{D}_X \, d\mu_X \tag{2.36}$$

Where D_M and D_X are the diffusion coefficients of metal and non-metal in the oxide layer, respectively.

The variables in Eq. (2.35) and (2.36) relatively easily measurable when the diffusion coefficients are assumed to be a function of the chemical potential of the species involved. Therefore, the relevant diffusion coefficient of the species incorporated in the oxide must be known as a function of chemical potential to predict the parabolic constant of the oxide [58]. Applicability of the theory is definitely limited as obtaining the required data is not easy. However, Wagner theory is still valuable in that it provides a fundamental mechanism of high temperature oxidation under the conditions given in the beginning of the chapter 2.

Application of Wagner oxidation theory

This chapter exemplifies the application of the Wagner theory using oxidation of Co to CoO which is p-type metal deficit oxide forming cation vacancies and electron holes [64-66]. The formation of singly charged cation vacancies can be represented as

$$\frac{1}{2}O_2 = O_O + V'_{Co} + h^{\cdot} \tag{2.37}$$

$$C_{h^{\cdot}} C_{V'_{Co}} = K p_{O_2}^{1/2} \tag{2.38}$$

By stoichiometry, $C_{h^{\cdot}} = C_{V'_{Co}}$ for electrical neutrality. Then, the following relation can be achieved:

$$C_{V'_{Co}} = C_{h^{\cdot}} \propto p_{O_2}^{1/4} \tag{2.39}$$

This means that the cationic partial conductivity, κ_c is proportional to $p_{O_2}^{1/4}$.

Assumed that CoO has very small stoichiometric deviations, the relations with regard to the chemical potential of CoO can be formulated as

$$\mu_{Co} + \mu_O = \mu_{CoO} \approx constant \tag{2.40}$$

The chemical potential of oxygen is expressed as

$$\mu_O = \frac{1}{2}\mu^{\circ}_{O_2} + \frac{1}{2}RT \ln p_{O_2} \tag{2.41}$$

Using Eq. (2.40) and (2.41), one can obtain

$$d\mu_{Co} = -\frac{1}{2}RT \ln p_{O_2} \tag{2.42}$$

Given that κ_c is proportional to $p_{O_2}^{1/4}$, substituting Eq. (2.42) into Eq. (2.33) yields the expression of the parabolic constant of CoO as a function of oxygen partial pressure:

$$k' \propto \int_{p'_{O_2}}^{p''_{O_2}} p_{O_2}^{1/4}\, d\ln p_{O_2} \tag{2.43}$$

$$k'_{CoO} \propto [(p''_{O_2})^{1/4} - (p'_{O_2})^{1/4}] \tag{2.44}$$

If p''_{O_2} is sufficiently high enough to neglect p'_{O_2} at the metal-oxide phase boundary and, thus, to avoid the reaction rate controlled by surface reactions or transport in the gas phase, Eq. (2.44) reduces to

$$k'_{CoO} \propto (p''_{O_2})^{1/4} \tag{2.45}$$

The existence of doubly charged cation vacancies can be represented as

$$\frac{1}{2}O_2 = O_O + V''_{Co} + 2h^{\cdot} \tag{2.46}$$

$$C_{h^{\cdot}}^2 C_{V''_{Co}} = K p_{O_2}^{1/2} \tag{2.47}$$

If the similar treatment described above is applied to the case of doubly charged vacancies, the parabolic constant of CoO would have the following relationship to oxygen partial pressure.

$$k'_{CoO} \propto (p''_{O_2})^{1/6} \tag{2.48}$$

Fisher and Tanhauser measured the electrical conductivity of polycrystalline CoO as a function of temperature and oxygen partial pressure which was in the range of 900 ~ 1450 °C and 1 ~ 10^{-12} atm, respectively. [65]. The plot of the conductivity against oxygen partial pressure shows that there are two distinguishable regions

where the conductivity is proportional to $(p''_{O_2})^{1/4}$ and $(p''_{O_2})^{1/6}$. These results indicate that the type of the predominant cation vacancies in CoO at high temperatures is dependent on the level of oxygen partial pressure. The similar results were reported by Eror and Wagner who measured the electrical conductivity of single crystalline CoO over the temperature range of 900 ~ 1200 °C [64].

a)

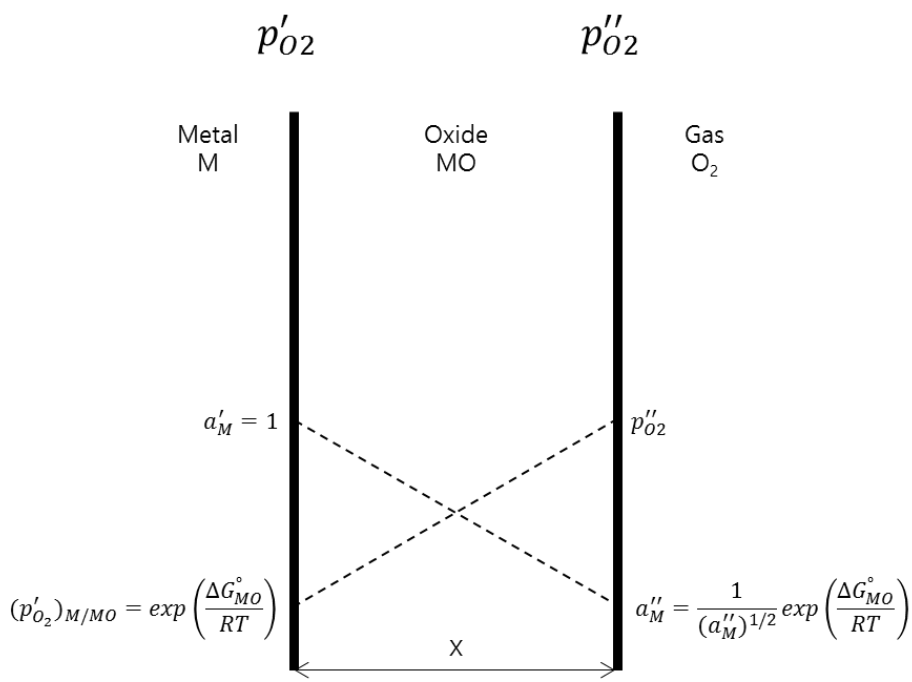
p'_{O2}
p''_{O2}
Metal
M
Oxide
MO
Gas
O_2
$a'_M = 1$
p''_{O2}
$(p'_{O_2})_{M/MO} = exp\left(\frac{\Delta G^\circ_{MO}}{RT}\right)$
$a''_M = \frac{1}{(a''_M)^{1/2}} exp\left(\frac{\Delta G^\circ_{MO}}{RT}\right)$
X

b)

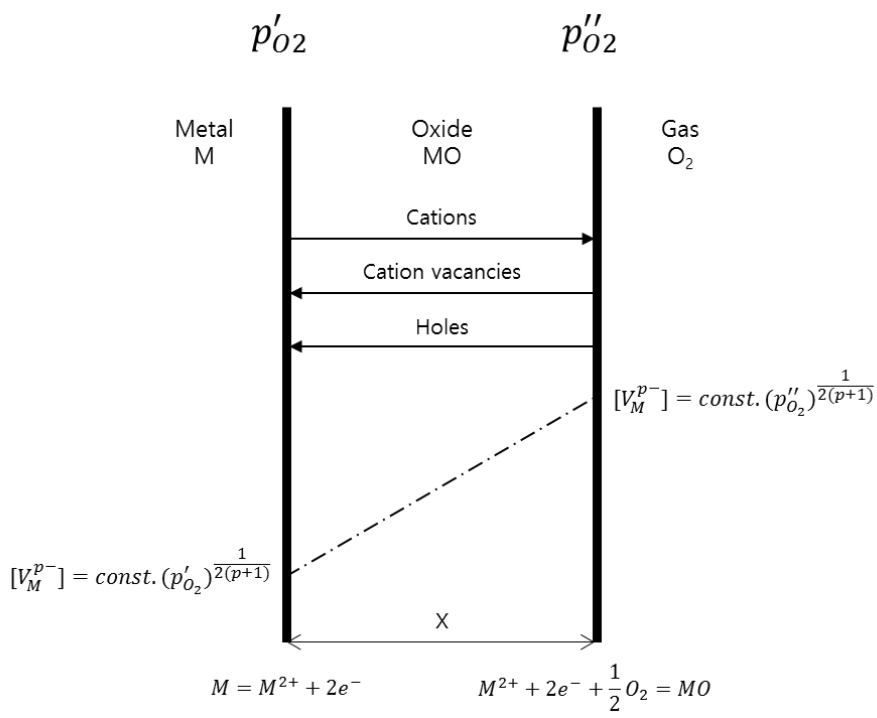
p'_{O2}
p''_{O2}
Metal
M
Oxide
MO
Gas
O_2
Cations
Cation vacancies
Holes
$[V_M^{p-}] = const.(p''_{O_2})^{\frac{1}{2(p+1)}}$
$[V_M^{p-}] = const.(p'_{O_2})^{\frac{1}{2(p+1)}}$
X
$M = M^{2+} + 2e^-$
$M^{2+} + 2e^- + \frac{1}{2}O_2 = MO$

c)

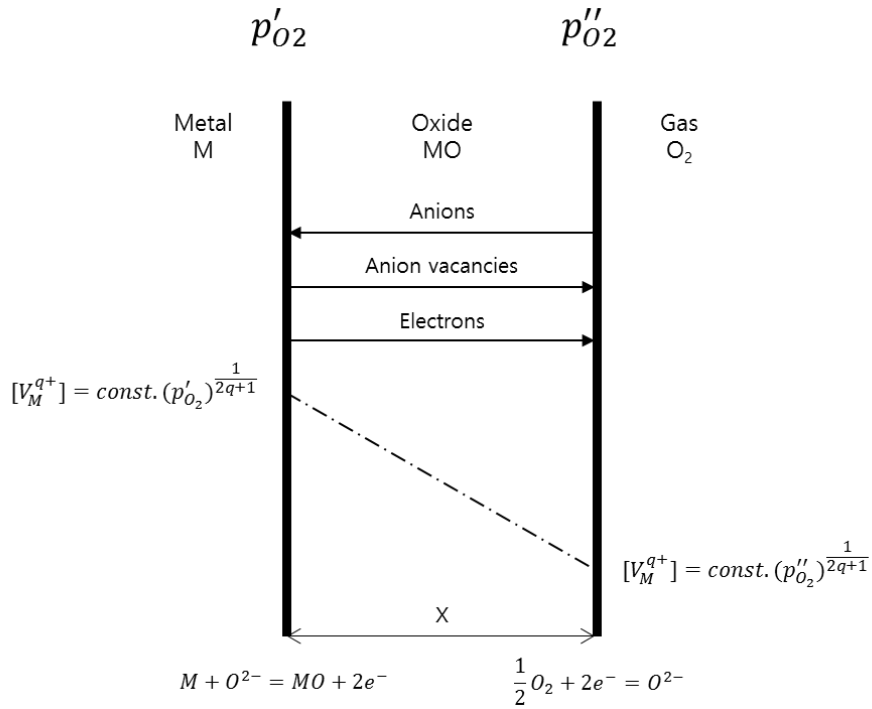

Fig. 2.2. Schematic presentation of scale formation according to the Wagner theory: a) activity gradients of metal and non-metal established across the growing oxide layer [58], b) concentration gradient of metal ion vacancies and transport processes in the metal deficit oxide and c) concentration gradient of non-metal ion vacancies and transport processes in the non-metal deficit oxide [59].

2.1.4 Internal oxidation

Internal oxidation of alloy occurs when oxygen permeates into the alloy, leading to sub-surface precipitation of the oxide of alloying elements. The process of internal oxidation proceed as follows. First, oxygen dissolves in the base metal matrix. This step may occur either at the external surface of the metal or at the oxide-scale interface if the external oxide scale is already present. For the nucleation of internal oxide precipitates, the inward-diffusing oxygen and outward-diffusing solute metal need to establish the critical activity product of the reactants (solute metal and oxygen) at a reaction front. Once the oxide precipitates nucleates, the growth of the precipitates progresses until the supply of solute metal to the precipitate front is depleted.

The following conditions need to be met for the occurrence of internal oxidation [58].

- ΔG° of formation (per mole O_2) of the solute metal oxide must be more negative than that of the base metal oxide.
- The reaction of the solute metal oxide ($Me + \nu O = BO_\nu$) must be spontaneous. The solubility and diffusivity of oxygen in the base metal need to be sufficient enough to establish the required activity of dissolved oxygen at the reaction front.
- The concentration of the oxidizing alloy element must be low enough to avert the transition from internal to external oxidation.
- No surface layer must prevent the dissolution of oxygen into the alloy at the beginning of oxidation.

Kinetics of internal oxidation

The kinetics of internal oxidation occurring in the planar specimen can be treated

base on Wagner analysis. The case considered for the treatment is that oxygen diffuses into the specimen of metal A-B and reacts with the outward-diffusing alloying element (B) to form oxide precipitate (BO_v). The derivation of the kinetics of internal oxidation requires the assumption that the solubility of the oxide precipitate in the base metal is so low that the concentration of both oxygen and B at the internal oxide front becomes zero. The concentration profile pertaining to the above case is given in Fig. 2.3.

The penetration depth (X) of the internal oxide is dependent on the diffusivity of oxygen (D_O) so X is expressed as

$$X = 2\gamma\sqrt{D_{\mathrm{O}}t} \tag{2.49}$$

where γ denotes the proportionality between X and characteristic diffusion length ($\sqrt{D_O t}$). Using Fick's second law, the diffusion of oxygen is expressed as

$$\frac{\partial N_{\mathrm{O}}}{\partial t} = D_{\mathrm{O}}\frac{\partial^2 N_{\mathrm{O}}}{\partial x^2} \tag{2.50}$$

The boundary conditions for Eq. (2.50) are given below

$$t = 0,\ N_{\mathrm{O}} = N_{\mathrm{O}}^{(\mathrm{S})}, for\ x = 0;\ N_{\mathrm{O}} = 0, for\ x > 0 \tag{2.51}$$

$$t = t,\ N_{\mathrm{O}} = N_{\mathrm{O}}^{(\mathrm{S})}, for\ x = 0;\ N_{\mathrm{O}} = 0, for\ x = 0 \tag{2.52}$$

Applying the boundary conditions to Eq. (2.50) yields the following solution.

$$N_{\mathrm{O}} = N_{\mathrm{O}}^{(\mathrm{S})}\left[1 - \frac{\mathrm{erf}\left(\frac{x}{2\sqrt{D_{\mathrm{O}}t}}\right)}{\mathrm{erf}(\gamma)}\right] \tag{2.53}$$

Using Fick's second law, the diffusion of solute metal can be expressed as

$$\frac{\partial N_{\mathrm{B}}}{\partial t} = D_{\mathrm{B}}\frac{\partial^2 N_{\mathrm{B}}}{\partial x^2} \tag{2.54}$$

The boundary conditions for Eq. (2.54) are given below.

$$t = 0,\ N_{\mathrm{B}} = 0, for\ x < 0;\ N_{\mathrm{B}} = N_{\mathrm{B}}^{(\mathrm{o})}, for\ x > 0 \tag{2.55}$$

$$t = t,\ N_{\mathrm{B}} = 0, for\ x = X;\ N_{\mathrm{B}} = N_{\mathrm{B}}^{(\mathrm{o})}, for\ x = \infty \tag{2.56}$$

Applying the boundary conditions to Eq. (2.54) yields the following solution.

$$N_{\mathrm{B}} = N_{\mathrm{B}}^{(\mathrm{o})} - \frac{N_{\mathrm{B}}^{(\mathrm{o})}\left[1 - \mathrm{erf}\left(\frac{x}{2\sqrt{D_{\mathrm{B}}t}}\right)\right]}{\mathrm{erfc}(\theta^{1/2}\gamma)} \tag{2.57}$$

where $\theta \sim D_{\mathrm{O}}/D_{\mathrm{B}}$. To calculate γ, the flux balance is established as below.

$$\lim_{\varepsilon\to 0}\left(-D_{\mathrm{O}}\frac{\partial N_{\mathrm{O}}}{\partial x}\right)_{x=X-\varepsilon} = v\left(D_{\mathrm{B}}\frac{\partial N_{\mathrm{B}}}{\partial x}\right)_{x=X+\varepsilon} \tag{2.58}$$

Eq. (2.59) and (2.60) are obtained by differentiating Eq. (2.50) and (2.54), respectively.

$$\left(\frac{\partial N_{\mathrm{O}}}{\partial x}\right)_{x=X} = \frac{N_{\mathrm{O}}^{(\mathrm{S})}}{\mathrm{erf}(\gamma)\sqrt{\pi}\sqrt{D_{\mathrm{O}}t}}\exp(-\gamma^2) \tag{2.59}$$

$$\left(\frac{\partial N_{\mathrm{B}}}{\partial x}\right)_{x=X} = \frac{N_{\mathrm{B}}^{(\mathrm{o})}}{\mathrm{erfc}(\theta^{1/2}\gamma)\sqrt{\pi}\sqrt{D_{\mathrm{B}}t}}\exp(-\theta\gamma^2) \tag{2.60}$$

Substituting Eq. (2.59) and (2.60) into Eq. (2.58) yields

$$\frac{N_{\mathrm{O}}^{(\mathrm{S})}}{N_{\mathrm{B}}^{(\mathrm{o})}} = \frac{v}{\theta^{1/2}}\frac{\mathrm{erf}(\gamma)}{\mathrm{erfc}(\theta^{1/2}\gamma)}\frac{\exp(\gamma^2)}{\exp(\theta\gamma^2)} \tag{2.61}$$

Eq. (2.61) can be numerically solved for certain conditions. Two important limiting cases are illustrated here.

- Case 1: *Negligible counter-diffusion of solute metal*

In Case 1, the diffusion of solute metal is very slow compared to that of oxygen and the solubility of oxygen is small compared to the solute metal content of the alloy A-B $\left(\frac{D_{\mathrm{B}}}{D_{\mathrm{O}}} \ll \frac{N_{\mathrm{O}}^{(\mathrm{S})}}{N_{\mathrm{B}}^{(\mathrm{o})}} \ll 1;\ \gamma \ll 1, \gamma\theta^{1/2} \gg 1\right)$. This case allows the simplification of the terms in Eq. (2.61) as shown below.

$$\mathrm{erf}(\gamma) = \frac{2}{\sqrt{\pi}}\gamma \tag{2.62}$$

$$\exp(\gamma^2) = 1 + \gamma^2 \sim 1 \tag{2.63}$$

$$\mathrm{erfc}\left(\theta^{1/2}\gamma\right) = \frac{2}{\sqrt{\pi}}\frac{\exp(-\gamma^2\theta)}{2\gamma\theta^{1/2}} \tag{2.64}$$

Substituting the simplified terms into Eq. (2.61) and solving the resulting equation for γ gives

$$\gamma = \left(\frac{N_{\mathrm{O}}^{(\mathrm{S})}}{2vN_{\mathrm{B}}^{(\mathrm{o})}} t \right)^{1/2} \tag{2.65}$$

- Case 2: *Significant counter-diffusion of solute metal*

When the counter-diffusion of the solute metal is significant, $\gamma \ll 1$ and $\gamma\theta^{1/2} \ll 1$. Accordingly, the approximation of the following terms becomes available.

$$\mathrm{erf}(\gamma) = \frac{2}{\sqrt{\pi}}\gamma \tag{2.66}$$

$$\exp(\gamma^2) \sim \exp(\gamma^2\theta) \sim 1 \tag{2.67}$$

$$\mathrm{erfc}\left(\theta^{1/2}\gamma\right) = 1 - \frac{2}{\sqrt{\pi}}\gamma\theta^{1/2} \sim 1 \tag{2.68}$$

Substituting Eq. (2.66), (2.67) and (2.68) into Eq. (2.61) yields

$$\gamma = \frac{\sqrt{\pi}\theta^{1/2}N_{\mathrm{O}}^{(\mathrm{S})}}{2vN_{\mathrm{B}}^{(\mathrm{o})}} \tag{2.69}$$

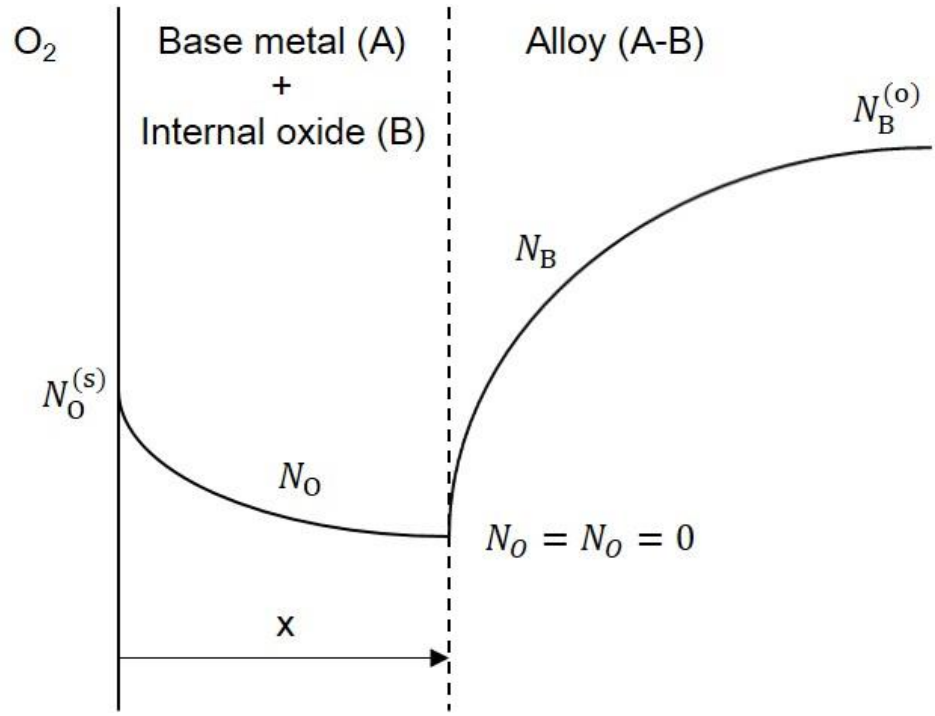

Fig. 2.3. Concentration profile for the treatment of the internal oxidation of the alloy A-B [58].

2.2 Cr evaporation

Cr evaporation is the inevitable phenomenon faced when Cr containing materials is exposed to oxidizing conditions containing oxygen and water vapor. This issue has been a technological problem with both broad technological and environmental implications. The hexavalent Cr is regarded as a carcinogenic hazard of special concern in waste incineration processes [67]. Also, the Cr evaporation is one of the major drawbacks in the development of SOFCs for which chromia forming ferritic stainless steel is used as interconnects [2, 9, 68]

Caplan and Cohen experimentally demonstrated that humidified oxygen promotes the Cr volatility of Cr (s) and Cr_2O_3 (s) [69]. Ebbinghaus reported the thermodynamic properties of various gas phase Cr species, discovering the dominant gaseous Cr species under normal incineration conditions [67] . The major volatile Cr oxide and hydroxide in the presence of water vapor and oxygen have been identified as CrO_3 and $CrO_2(OH)_2$. The chemical reaction for each Cr species is described below [28].

$$\frac{1}{2}Cr_2O_3(s) + \frac{3}{4}O_2(g) = CrO_3(g) \tag{2.70}$$

$$\frac{1}{2}Cr_2O_3(s) + H_2O(g) + \frac{3}{4}O_2(g) = CrO_2(OH)_2(g) \tag{2.71}$$

$$\frac{1}{2}Cr_2O_3(s) + \frac{1}{2}H_2O(g) + \frac{1}{2}O_2(g) = CrO_2(OH)(g) \tag{2.72}$$

Numerous researchers have attempted to establish the thermodynamic dataset related to the aforementioned gaseous Cr species [67, 70, 71]. Some other made use of the dataset for the prediction of the vapor pressure or comparative study [27, 72]. Fig. 2.4 a) shows the comparative plot of the vapor pressure of the Cr species vs. a temperature range, based on the different literature data [73]. In case of CrO_3 (g), the

calculated vapor pressure based on two different data was well agreed while a large discrepancy is observed for $CrO_2(OH)_2$ (g).

As of now, the literatures on the thermodynamics of $CrO_2(OH)_2$ (g) have not been able to give agreeable and reliable data. Opila et al. conducted both theoretical and experimental study on the thermochemistry of $CrO_2(OH)_2$ (g) [71]. Their experimental data lies within the range between Ebbinghaus [67] and Glusko (source data for IVATANTHERMO thermodynamic program) [74]. The experimental data obtained by Kurokawa et al. [46] and Gindolf et al. [27] also falls in the range but below one given by Opila. et al. Therefore, the upper and lower limit of the range can be defined as the Ebbnighaus and Glusko, respectively. It should be noted that the Ebbinghaus data results in the overestimation of the equilibrium vapor pressure of $CrO_2(OH)_2$ (g) [75] and Opila et al. [71] neglect the Glusko data for its too low value.

The partial pressure of $CrO_2(OH)_2$ (g) changes by less than a factor of ten in between 700 and 1200 °C, indicating that its temperature dependency is weak compared to that of CrO_3 (g). However, the change in the equilibrium vapor pressure of $CrO_2(OH)_2$ (g) is very susceptible to humidity change as shown in Fig. 2.4 b). Gindolf et al. [27] claimed that, at a partial pressure of H_2O (g) > 500 Pa, $CrO_2(OH)_2$ (g) becomes predominant as a Cr^{6+} containing gas phase. If the Glusko and Ebbinghaus data for CrO_3 (g) is correct, the transition point lies at around 900 °C and, therefore, gaseous Cr species consist of a considerable amount of $CrO_2(OH)_2$ (g) only under the experimental condition (800 °C, pH_2O ~ 2000 Pa) used for the present study. Since the level of all the experimental data for $CrO_2(OH)_2$ is greater than the equilibrium partial pressure of CrO_3 (g) predicted based on the Glukos and Ebbinghaus data, it is reasonable to regard $CrO_2(OH)_2$ (g) as the dominate Cr^{6+} containing gas phase under the present experimental condition that water vapor is present.

a)

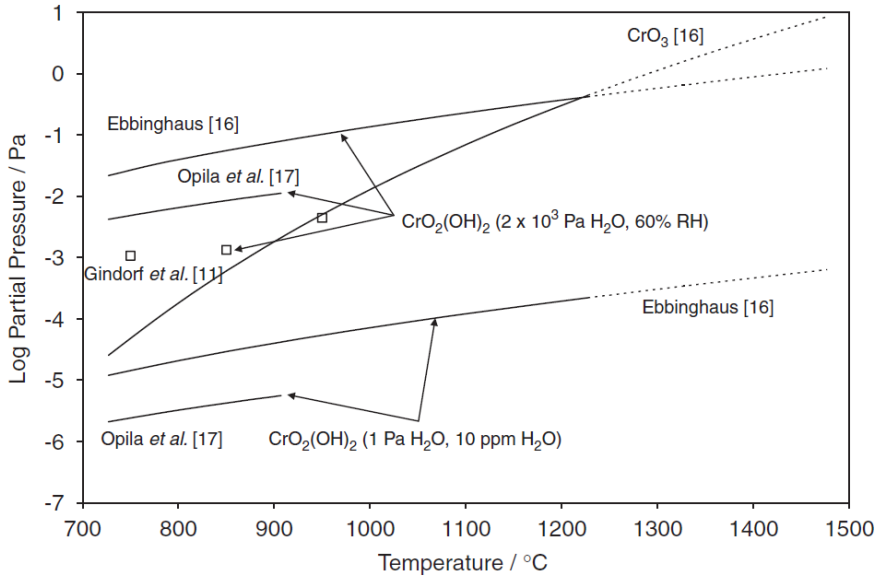

b)

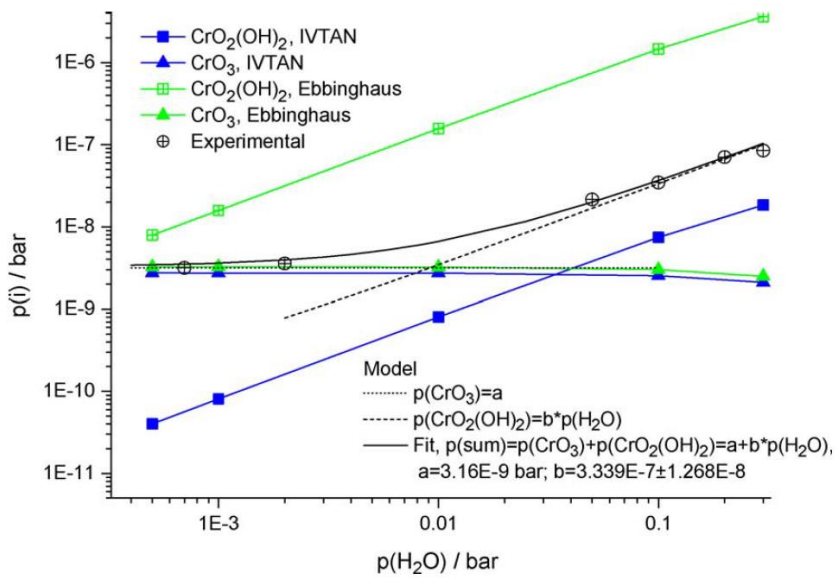

Fig. 2.4 a) Vapor pressure of two dominant volatile Cr species in humid air based on the different thermodynamic database [73] and b) the change in the Cr evaporation from Cr_2O_3 (s) at 950 °C in air over different humidity levels [27].

2.3. Solid oxide fuel cell (SOFC)

The fuel cell is a device that directly converts chemical energy to electrical energy by virtue of electrochemical processes without combustion. Generation of electricity through the electrochemical process offers a clean, low-pollution energy with reduced green-house gas emission in comparison to other nature-dependent resources. The type of the fuel cell can be subdivided according to electrolyte materials, or operating temperature.

The electrolyte of the SOFC is a solid, non-porous metal oxide, usually Y_2O_3-stabilized ZrO_2. The operating temperature of the SOFC ranges from 650 to 1000 °C [1, 76]. Compared to other types of the fuel cells, the SOFC operates at relatively high temperature to facilitate ionic conduction by oxygen ions. SOFCs have the advantages of flexible fuel selection, reliability, modularity and high efficiency. Moreover, the high operating temperature eliminates need of a fuel reformers required for reforming of hydrocarbon fuels and provide high quality exhaust heat for cogeneration. [5].

2.3.1 Operating principle of SOFC

A single cell of the planar type SOFC consists of an ion-conducting electrolyte and two porous electrodes. Fig. 2.5 shows the singles cells stacked in a series requiring interconnects for an increase in the voltage output. As described in Fig. 2.6, oxygen gas or air is supplied to the cathode where reduction occurs to form an oxygen ion.

$$\frac{1}{2}O_2(g) + 2e^- = O^{2-} \tag{2.73}$$

The oxygen ion migrates through the electrolyte to the anode. Fuel gas in form of H_2 or hydrocarbon is fed to the anode, reacting to the oxygen ion to produce water.

$$H_2(g) + O^{2-} = H_2O\ (\mathrm{g,l}) + 2e^- \tag{2.74}$$

The liberated electrons flow through an external circuit to the cathode, which is balanced by the ionic current across the electrolyte. Since all the electrochemical reactions take place at triple phase boundaries (gas-electrolyte-electrode), the cell performance is largely influenced by both the area and catalytic activity of the triple phase boundaries.

The open circuit voltage, E, of the SOFC is defined by the Nernst equation expressed as

$$E = \frac{RT}{4F} ln\left(\frac{pO_2\ in\ oxidant}{pO_2\ in\ fuel}\right) \tag{2.75}$$

where R is the gas constant, T the cell temperature, F the Faraday constant and pO_2

the oxygen partial pressure. The maximum voltage of an ideal sing SOFC cell is in a range of 1 V to 1.2 V. However, a single SOFC cell in reality generates, approximately, 70 % of its maximum voltage with a maximum power density of 0.9 $W \cdot cm^{-2}$ owing to irreversible voltage loss, attributed to activation polarization, concentration polarization, and ohmic loss. The activation polarization arises from charge transfer reactions at the electrode-electrolyte interfaces and the charge collector-electrode interfaces where two oppositely charged surfaces meet. The concentration polarization is associated with the slow mass transport rate of oxygen ions in comparison to that of the charging and discharging current. The ohmic loss is attributed to the resistance to the flow of ions in the electrolyte as well as resistance to the flow of electrons in the electrodes.

The voltage of the actual operating SOFC single cell can be expressed as

$$V = E - IR_i - (\eta_a + \eta_c) \tag{2.76}$$

where I is the cell current and R_i is the internal resistance of the cell; therefore, IR_i denotes the ohmic loss. η_a and η_c is the cathode polarization and the anode polarization, respectively.

Fig. 2.7 shows the plot of operating cell voltage vs. current density [76]. It is evident that the dominance of the polarization depends on the level of current density and the voltage loss is proportional to a level of current density. Accordingly, a compromise between cell voltage and current density has to be made to achieve the optimum cell performance. At peak power density, the ohmic and polarization losses can account for 30 ~ 60 % of the voltage loss. Therefore, the reduction of such polarization losses is one of the main objectives in the field of SOFC academia and industries.

2.3.2 Cell design

The two most common SOFC designs are the tubular and the planer. The schematic illustration of the tubular and planar design is given in Fig. 2.8 [5]. The tubular SOFC designed by Siemens Westinghouse consists of the cell components in the form of thin layers on a doped lanthanum manganite cathode tube fabricated by extrusion and sintering. The yttria-stabilized zirconia (YSZ) electrolyte with a thickness of about 40 μm is deposited by electrochemical vapor deposition and the Ni/YSZ anode is deposited either by nickel slurry application followed by electrochemical vapor deposition of YSZ or by sintering of a Ni/YSZ slurry. The doped lanthanum chromite interconnecting strip is deposited along the length of the tube by plasma spraying. Singhal has electrically tested the tubular cells up to about 25,000 h under various operating conditions [1]. The cell performs satisfactorily with a performance degradation rate less than 0.1 % per 1000 h. However, the cells provide a power density at 1000 °C in a range of 0.25 ~ 0.30 W/cm^2, which makes it suitable only for stationary power generation.

2.3.3 Metallic interconnect for SOFC

The two main functions of interconnects of SOFCs are to provide electrical connection between each cell and physical protection for anode and cathode. Since the interconnect is simultaneously exposed to both reducing and oxidizing atmosphere at high temperature (600 ~ 1000 °C) in direct contact with the electrodes and sealant, the following technical requirements should be considered for material selection [2, 10, 77]:

- Good surface stability under the bipolar condition.
- Thermal expansion matching to ceramic counterparts.
- High electrical conductivity (1 S cm^{-1}) and thermal conductivity (5 $Wm^{-1}K^{-1}$)
- Low oxygen and hydrogen permeability,
- Compatibility with adjacent components such as electrodes and sealing material.
- Mechanical durability at operating temperature (e.g. high creep strength)
- Easy fabrication and low material cost

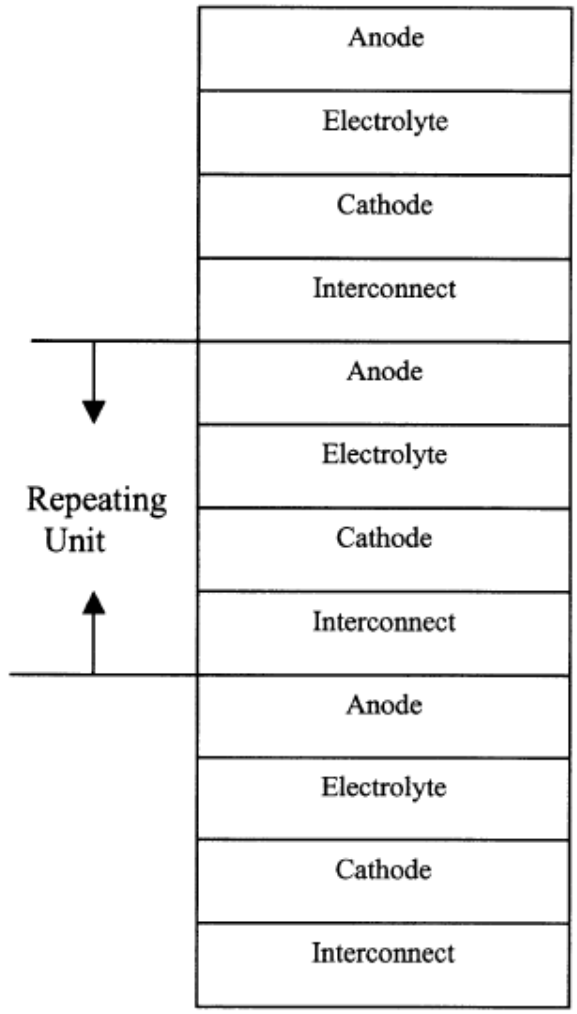

Fig. 2.5. Schematic configuration of SOFC stack.

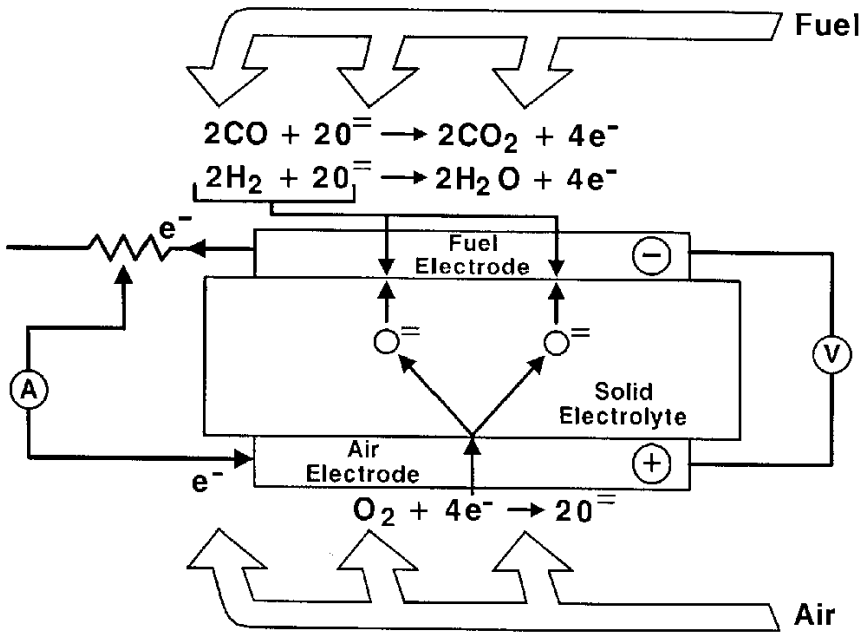

Fig. 2.6. SOFC operating process occurring in each component of a single SOFC cell [76].

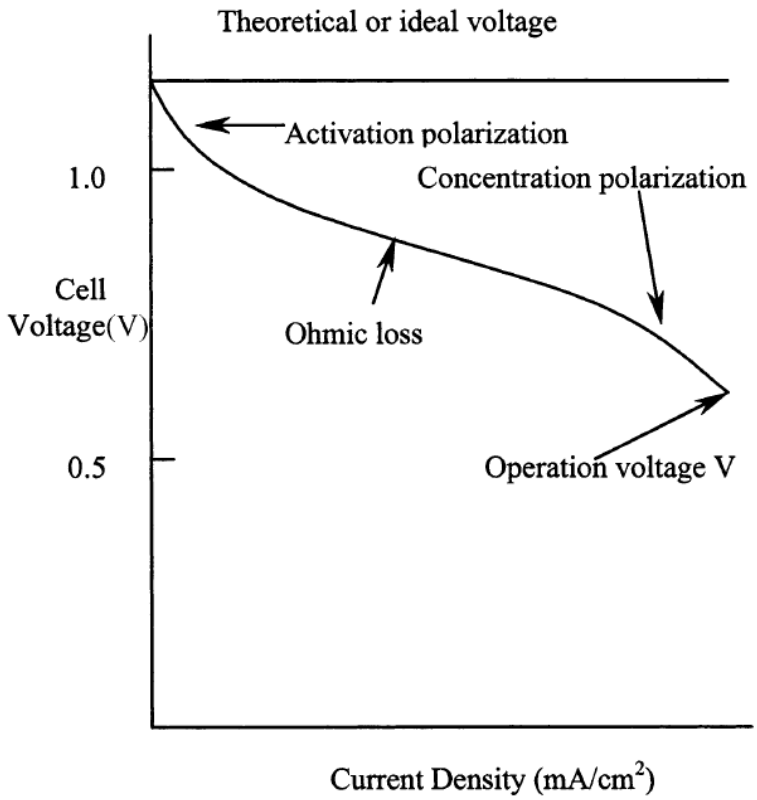

Fig. 2.7. The operating cell voltage characteristics as a function of current density [76].

a)

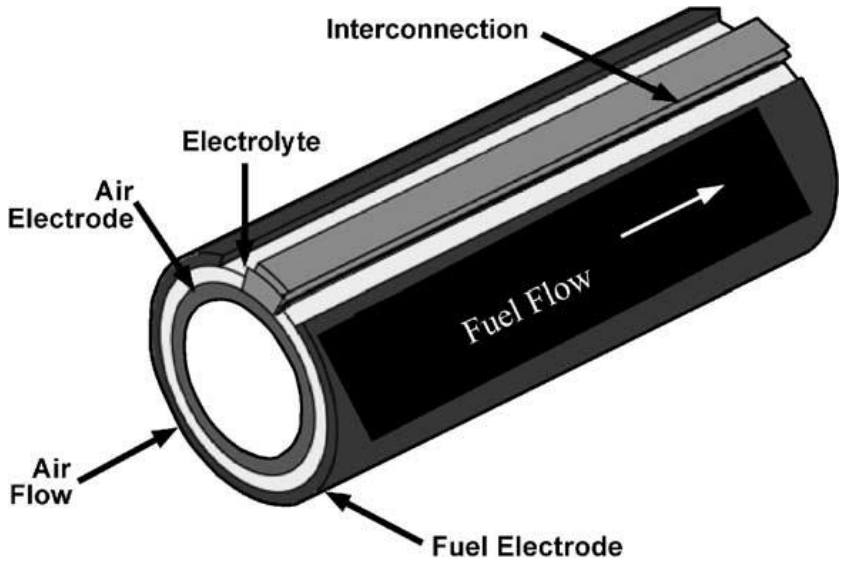

b)

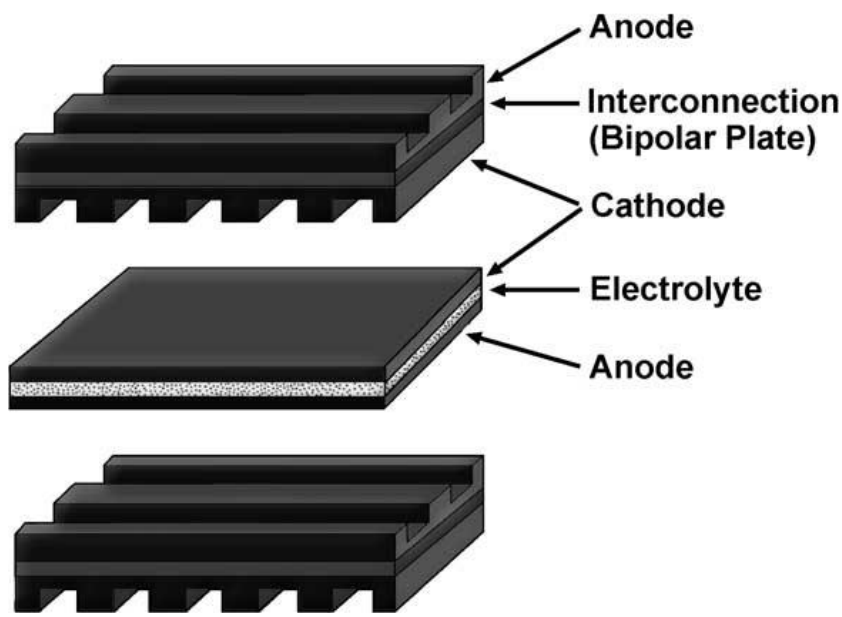

Fig. 2.8. Schematic illustration of (a) the tubular SOFC designed by Siemens Westinghouse and (b) the planar SOFC design.

2.4 Transpiration method

Weir and De Loos state that five methods are widely employed to measure the vaporized substances [78]. The methods are referred to as static, ebulliometric (dynamic), effusion (Knudsen and Langmuir methods), calorimetric and transpiration. In this study, the transpiration method was used for quantification of a Cr release so the details of only the transpiration method will be reviewed.

The transpiration method, also called the transportation or gas saturation method, was first proposed by Regnault in 1845, but was not widely used until the advent of automated chromatographic analytical techniques in 1970s. It is one of the oldest and most versatile ways of studying heterogeneous equilibria involving gases. This method has been applicable to both organic [79, 80] and inorganic [27, 35, 81] substances. The several advantages of the transpiration methods are [78]

- Not affected by a small amount of volatile impurities
- Possible to measure the equilibrium vapor pressure within a short time
- Possible to measure in various atmospheres by changing carrier gas
- Possible to measure vapor pressure over temperature range close to ambient

The method can be applied for the experiment under a low vapor pressure of 7 kPa downward [80] and can be conducted for a wide range of temperature. The thermodynamic property determined from the temperature dependence of the vapor pressure is in good agreement with other established techniques. This is well exemplified by Kulikov et al. who compared the molar enthalpies of vaporization of several organic compounds obtained by the transpiration method with the computed values based on the ERAS model [79].

In the method, either inert or reactive gas is passed over the pure compound of interest or analyte-coated inert support placed in a thermostatically controlled

saturator. The gas is flowed at a sufficiently low rate to reach equilibrium conditions. The gaseous substance of interest in the saturate vapor is collected using impingers, sorbents or cryogenic traps. The amount of the collected substance is quantified by some appropriate methods.

Fig. 2.9 demonstrates the schematic diagram of the transpiration apparatus setup [80]. The saturator packed with the analyte (~ 0.1 – 0.5 g) is fully immersed in a thermo-fluid bath, the temperature of which is maintained by a thermostat. The temperature in the saturator is monitored by a Pt resistance thermometer, or any other appropriate means. The preheated carrier gas is injected through insulated loop line to the saturator and equilibrated with the sample. The vapor saturated with the gasified sample condenses in the cold trap, directly conjunct to the outlet of the saturator. This study slightly modifies the apparatus setup to reproduce the actual SOFC cathodic atmosphere by using a tubular saturator in a furnace. The detailed description of the modified apparatus is given later.

The saturation vapor pressure, p_i, of the sample at certain temperature can be calculated from the mass of the product collected in the cooling trap within a definite period of time, using the following equation [78]

$$p_i = \frac{m_i R T_a}{V M_i} \tag{2.77}$$

$$V = V_{gas} + V_i \; (V_{gas} \gg V_i) \tag{2.78}$$

where R is the gas constant, m_i the mass of transported compound, M_i the molar mass of the compound and V_i its volume contribution to the gaseous phase. V_{gas} is the volume of transporting gas and T_a the temperature of the device used to measure the flow rate.

The transpiration experiments can be divided into two parts. The first is to verify

the plateau in the plot of the vapor density vs. the flow rate at a suitable temperature to grasp saturation conditions. The second is to determine equilibrium vapor pressure at various temperatures to derive the mean enthalpy of vaporization or sublimation. For this study, the first was preliminary performed to set the proper flow rate for the metallic sample and the result was compared with the literature data for its validity.

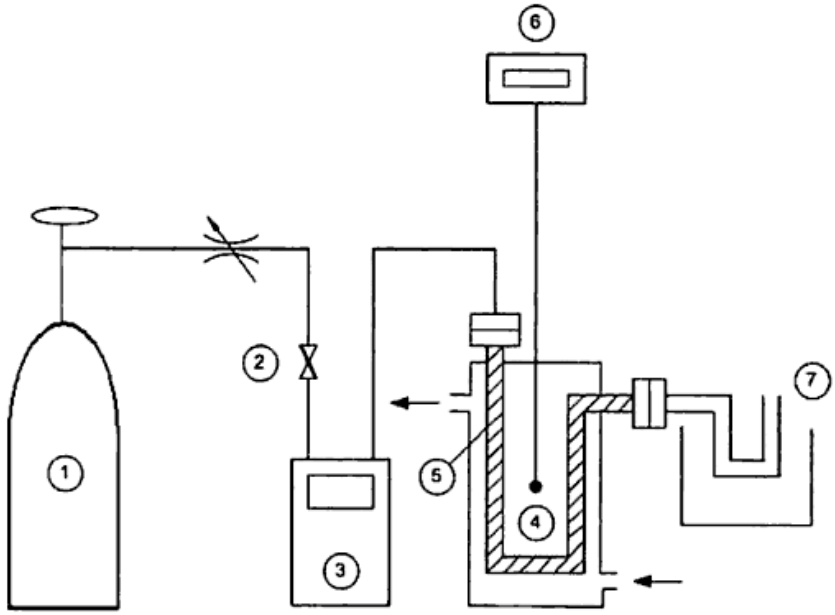

Fig. 2.9. Schematic diagram of the conventional transpiration apparatus setup. 1. Carrier gas cylinder; 2. Flow valve; 3. Digital mass flow meter; 4. Equilibrium cell; 5. Saturator filled with the sample; 6. Thermometer; 7. Cooling trap at T = 243 K [80].

2.5 Miscellaneous information of oxide

2.5.1 A_2O_3 oxide (corundum structure)

The corrosion resistance of stainless steel is determined by the formation of a passive oxide layer on a surface. Passivating the surface of stainless steel with Cr_2O_3 requires a minimum of 10.5 wt. % Cr up to 26 wt. % for extreme environments [82] (e.g. highly humid air). At room temperature, the surface of stainless steel does not look rusty, but a continuous atomic layer of Cr_2O_3 readily develops on the surface [83], prohibiting further oxidation.

Cr_2O_3, which adopts the corundum structure, is one of the main oxides that will repeatedly appear in this thesis. The corundum structure ($A_2^{2+}O_3^{2-}$) consists of a hexagonal close packed array of anions with Cr occupying 2/3 of octahedral sites. The unit cell of the spinel oxide projected on a (001) and (110) plane is illustrated in Fig. 2.10.

Fig. 2.11 shows the coordination polyhedra of octahedral and tetrahedral sites in hexagonal closed packing. A set of octahedra within a layer shares the opposite faces with other sets within neighboring layers, which forms a continuous chain orthogonal to the closest-packed plan. Two different sets of the tetrahedra in each layer make a pair, pointing in the opposite direction. They share the same face while the other three faces are surrounded on by adjacent octahedra, forming a different type of a continuous chain. Contrary to cubic closed packing structure which will be discussed later, cation diffusion in hexagonal closed packing can proceed through diffusion paths composed of like sites if the sites are fully or partly vacant. In case of Cr_2O_3 with 2/3 of the octahedral sites unoccupied by nature, it can be postulated that cation diffusion occurs *via* diffusion paths including octahedral sites.

One of the main roles of a SOFC interconnector is to electrically connect each

SOFC cell. Formation of a continuous, passive oxide layer (particularly Cr_2O_3 for stainless steel) is unavoidable within the range of operating temperatures; accordingly, electrical conductivity of the oxide is the significant property for evaluating material compatibility for SOFC interconnect application. The electrical conductivity of candidate materials has been generally compared in the form of ASR [10, 11, 84-86]. Even though the present study will not cover the effects of alloy gain size and surface modification on ASR, the information on the electrical conductivities of Cr_2O_3 [87-91] and $MnCr_2O_4$ [85, 92] is compiled through literature review. Cr_2O_3 and $MnCr_2O_4$ are selected since these oxides have been known as the stable oxides formed in uncoated Crofer22 APU under common SOFC cathodic conditions [24, 93]. Comparison of the electrical conductivities is given in Fig. 2.12. At 800 ºC, the respective electrical conductivity of Cr_2O_3 considerably differs from one order of magnitude while that of $MnCr_2O_4$ exhibits consistency. Nevertheless, it is verified that Cr_2O_3 possesses higher electrical conductivity than $MnCr_2O_4$.

The conductivity of Cr_2O_3 exhibits extrinsic behavior in the high temperature range (> 1000 ºC) while intrinsic behavior is observed in the low temperature range (< 1000 ºC) [88, 91]. A large discrepancy between each plot of Cr_2O_3 was pronounced in the low temperature range. This is because the intrinsic behavior of Cr_2O_3 is largely dependent of impurities as well as, to some degree, of oxygen activity; moreover, equilibration periods may influence the electrical conductivity due to slow diffusion in oxide in the low temperature region.

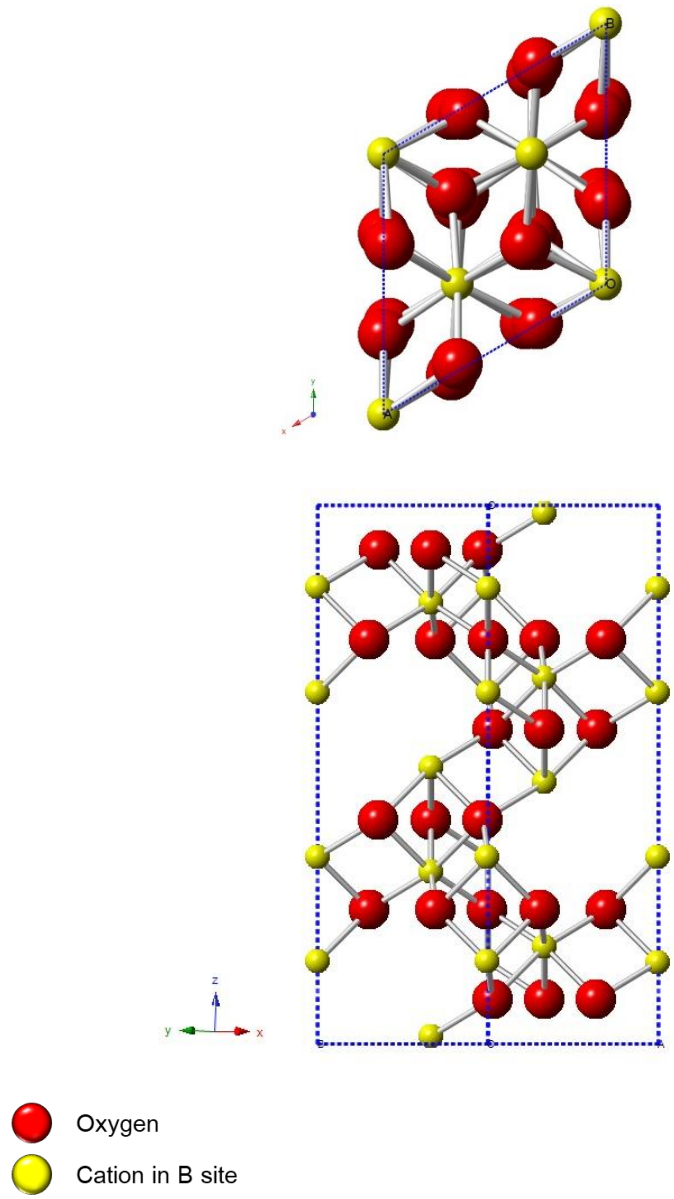

Fig. 2.10. Projection of the unit cell of the trigonal oxide on a (001) plane (top) and (110) plane (bottom).

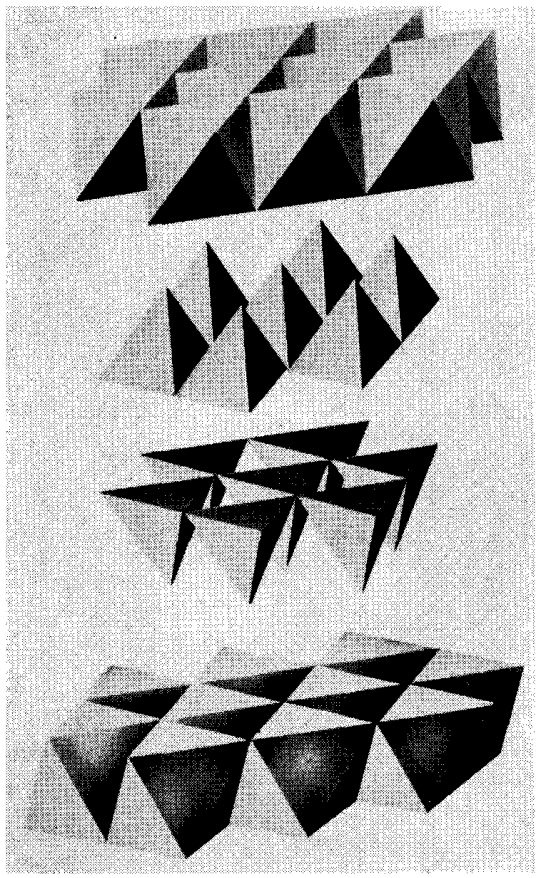

Fig. 2.11. Exploded array of the coordination polyhedra of octahedral and tetrahedral sites in hexagonal closed packing structure [94].

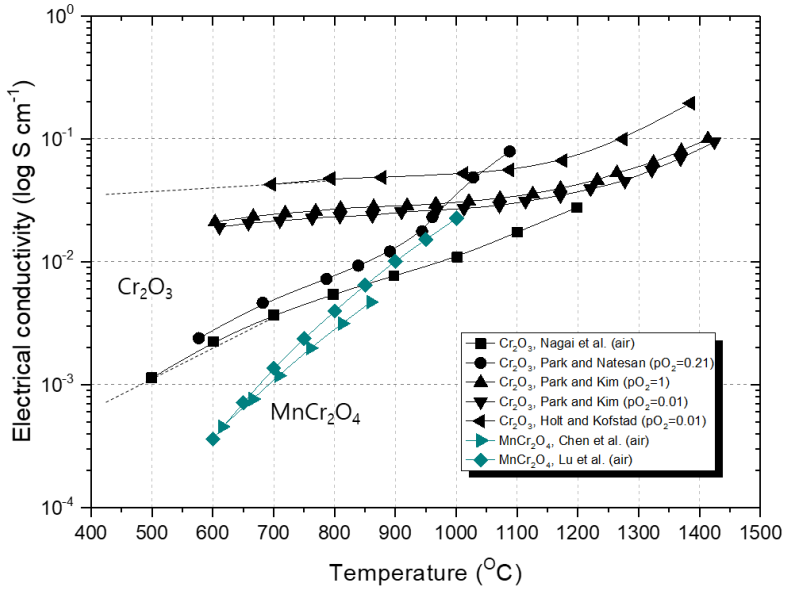

Fig. 2.12. Comparison of the electrical conductivity of Cr_2O_3 [87-91] and $MnCr_2O_4$ [85, 92].

2.5.2 A_3O_4 oxide (spinel structure)

Spinel is the name of the mineral, $MgAl_2O_4$. Its structural arrangement is shared by many transition metal oxides with a general formula of $A^{2+}B_2^{3+}O_4^{2-}$. The spinel oxides are composed of the oxide anions arranged in a cubic-close-packed lattice and the metallic cations occupying the interstices (octahedral and tetrahedral sites). There are 32 oxygen atoms, 64 tetrahedral A sites and 32 octahedral B sites in a single unit cell of the spinel oxide. The tetrahedral spaces are smaller than the octahedral spaces. One eighth of the tetrahedral sites and a half of octahedral sites are occupied by the metallic cations. The unit cell of the spinel oxide projected on a (001) and (110) plane is illustrated in Fig. 2.13 and the layout of the octahedral and tetrahedral sites in [101] projection is presented in the polyhedral scheme in Fig. 2.14.

There exist two different types of the spinel structure: normal and inverse structure. In case of the normal spinel structure, divalent cations occupy the tetrahedral A site while trivalent cations occupy the octahedral B site. The inverse spinel structure has an alternative arrangement where all of the divalent cations and a half of the trivalent cations occupy octahedral sites while the other half of the trivalent cations occupy tetrahedral sites. The general formula of the inverse spinel structure is $B^{3+}A^{2+}B^{3+}O_4^{2-}$.

The main type of the spinel oxide coming to the fore in Part B of this study is $MnCo_2O_4$ gradually transformed from Co_3O_4 with an increasing Mn fraction. Visualizing the lattice structure of a spinel oxide will be helpful in comprehending the transport process of cations through octahedral and tetrahedral sites.

As shown in Fig. 2.15 [94], the polyhedron of each tetrahedral site in spinel oxide is connected by only edges as is that of an octahedral site. On this account, the saddle-point configuration through the faces of the same polyhedra is not favored and, therefore, the cation transport in spinel oxide will readily occur through an

alternating array of octahedral and tetrahedral sites. This indicates that the cationic transport in inorganic compounds will be dependent on its inherited cationic site occupancy.

In the rock salt structure, the metal atoms occupy all the octahedral sites. Since the octahedral sites constitute any conceivable diffusion path, the metal atom must be removed from the octahedral site for diffusion to initiate. This necessitates the formation of either Schottky or Frankel defects [95] if the substance is stoichiometric. On the other hand, the spinel structure already has a large number of innate unoccupied sites as described above. This means that unoccupied octahedral sites may connect with unoccupied tetrahedral sites, forming a continuous diffusion path. For example, Sun applied the similar geometrical concept to the high activation energy of Cr diffusion in $CoCr_2O$ which has normal spinel structure [96].

The above concept is the base of the energy-wise discussion accounting for fast Mn diffusion in $MnCo_2O_4$. The details of the discussion pertaining to $MnCo_2O_4$ will be presented in Chapter 5.

According to the recent research trend, it is necessary to apply surface modification to address many SOFC related issues. To meet the industrial requirements, coating materials need to be thermally compatible with a substrate and electrically conductive. Petric and Ling [42] compared the thermal and electrical properties of various binary spinel oxides (See Table 2.1). In terms of CTE, Fe containing oxide is most compatible with ferritic stainless steel. The Mn-Co oxide exhibited modest CTE matching. However, the electrical conductivity of the Mn-Co oxide ranked second. This renders the Mn-Co oxide suitable for the surface modification of SOFC interconnect materials.

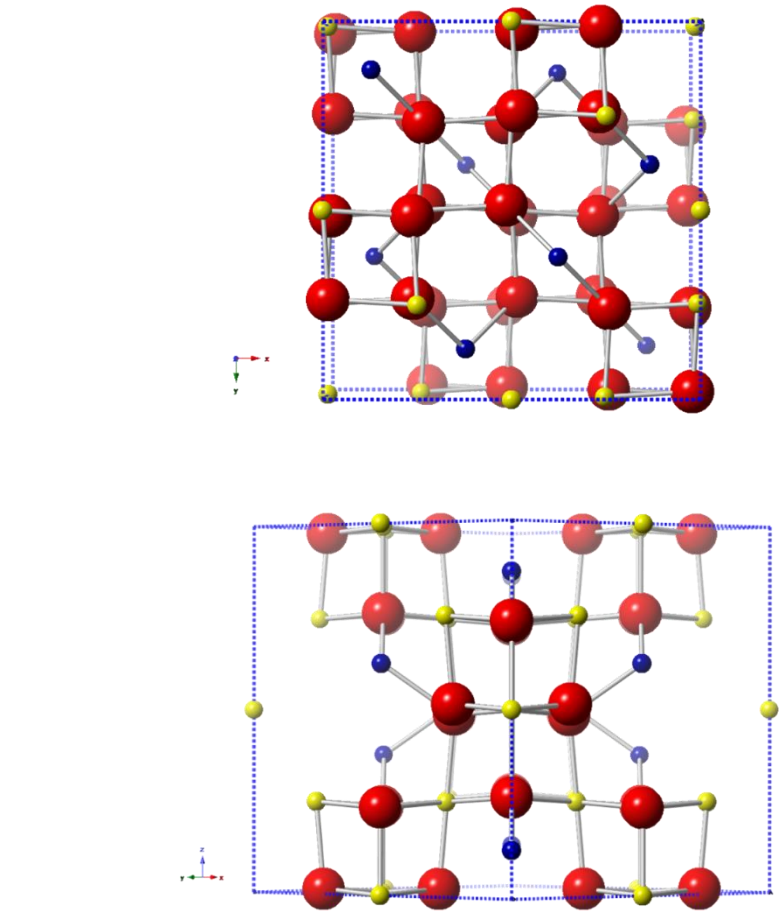

Fig. 2.13. Projection of the unit cell of the spinel oxide on a (001) plane (top) and (110) plane (bottom).

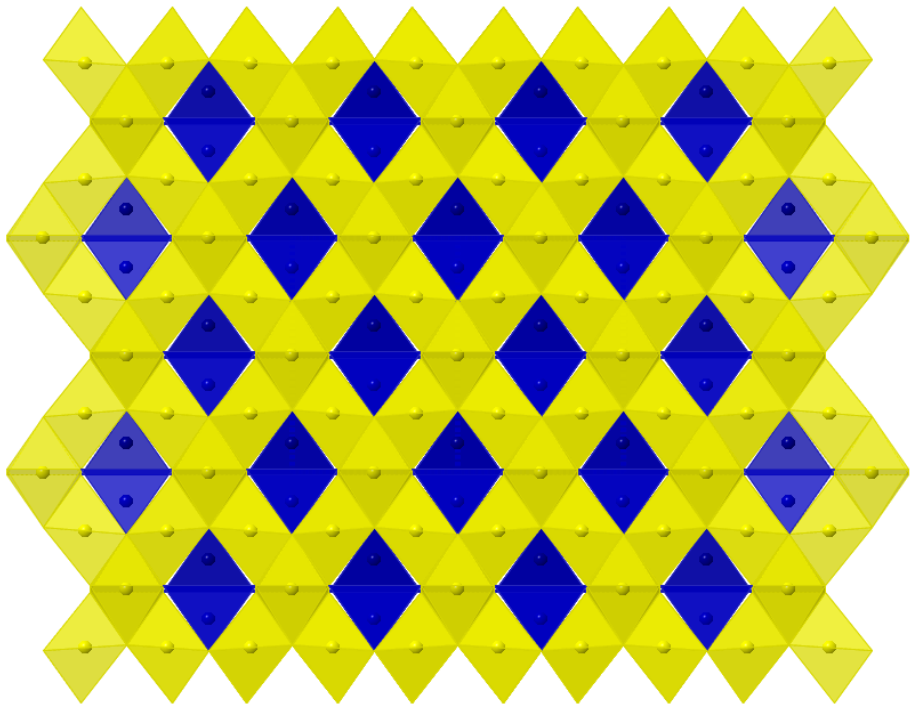

Fig. 2.14. Arrangement of the octahedral (yellow) and tetrahedral (blue) sites in [101] projection.

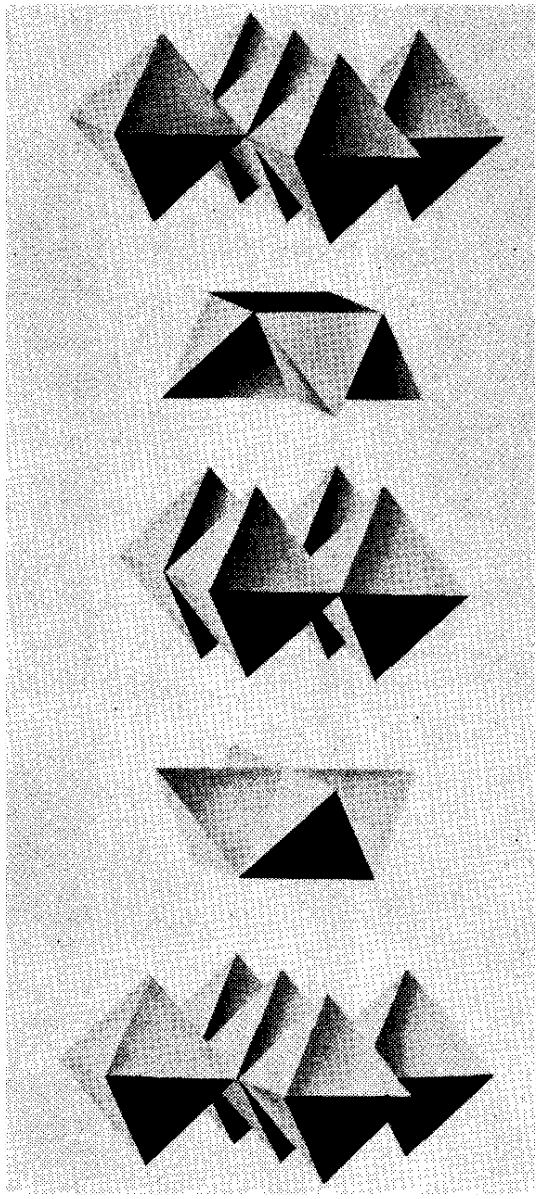

Fig. 2.15. Exploded array of the coordination polyhedra of octahedral and tetrahedral sites in cubic closed packing structure [94]. Each layer is aligned parallel to (001).

		Mg	Mn	Co	Ni	Cu	Zn
Al		$MgAl_2O_4$	$MnAl_2O_4$	$CoAl_2O_4$	$NiAl_2O_4$	$CuAl_2O_4$	$ZnAl_2O_4$
	σ	10E-6	10E-3	10E-5	10E-4	0.05	10E-6
	α	9	7.9	8.7	8.1	-	8.7
Cr		$MgCr_2O_4$	$Mn_{1.2}Cr_{1.8}O_4$	$CoCr_2O_4$	$NiCr_2O_4$	$CuCr_2O_4$	$ZnCr_2O_4$
	σ	0.02	0.02	7.4	0.73	0.4	0.01
	α	7.2	6.8	7.5	7.3	-	7.1
Mn		$MgMn_2O_4$	Mn_3O_4	$CoMn_2O_4$	$NiMn_2O_4$	$Cu_{1.3}Mn_{1.7}O_4$	$ZnMn_2O_4$
	σ	0.97	0.1	6.4	1.4	225 (750°C)	
	α	8.7	8.8	7	8.5	12.2	
Fe		$MgFe_2O_4$	$MnFe_2O_4$	$CoFe_2O_4$	$NiFe_2O_4$	$CuFe_2O_4$	$ZnFe_2O_4$
	σ	0.08	8.0	0.93	0.26	9.1	0.07
	α	12.3	12.5	12.1	10.8	11.2	7.0
Co			$MnCo_2O_4$	Co_3O_4			
	σ		60	6.7			
	α		9.7	9.3			

σ is electrical conductivity (S cm^{-1}).
α is CTE (10^{-6} $°C^{-1}$).

Table 2.1. Comparison of the CTE and electrical conductivity of various binary spinel oxides [42].

Chapter 3.

Materials and methods

3.1 Sample preparation

Crofer22 APU, manufactured by ThyssenKrupp VDM GmbH, was used for high temperature oxidation and evaporation experiment. Its nominal chemical composition, determined by a spark emission spectroscopy analyzer (QSN-750, OBLF GmbH, Germany), is tabulated in Table 3.1.

A Crofer22APU sheet (2 mm) and plate (20 mm), manufactured by ThyssenKrupp VDM GmbH, was used to conduct the study on their oxidation behavior. The rectangular specimens with a dimension of 10 × 10 × 2 mm were prepared by laser cutting for the oxidation study. The specimens from the plate were cut from the center of the plate along a rolling direction; consequently, normal direction (ND) planes take up most of the reaction area. The oxidation specimens were mechanically polished to 800 (P-2400) grit SiC abrasive paper and then ultrasonically rinsed with acetone.

Rectangular sheets rounded at both ends with a radius of 10 mm were wire-cut from a 2 mm thick Crofer22APU sheet. The edges of the specimens were rounded to prevent oxide spallation. The total length, width and thickness of the specimen is 80 mm, 20mm and 2 mm, respectively. The geometry and dimension of the specimen is described in Fig. 3.1 [97]. All the surfaces of the evaporation specimens were mechanically polished to 2000 grit SiC paper. Thickness of the specimen for the evaporation test was individually measured to calculate its specific surface area.

To investigate the effect of surface modification by Co electroplating on Cr evaporation, Co deposition was conducted by DC pulse electroplating. The

experimental parameters for Co pulse electroplating are listed in Table 3.2. The details of the electroplating parameters and procedure used for the present study is given in [98]. Preliminary microstructure analysis by XRD and TEM revealed that hexagonal close-packed Co with a thickness of, approximately, 400 nm was formed through electroplating as shown in Fig. 3.2.

C	Si	Mn	Ni	Cr	Mo
0.008	0.084	0.441	0.052	22.487	0.017
Ti	V	W	N	La	Fe
0.052	0.012	0.104	0.013	0.047	bal.

Table 3.1. Nominal chemical composition of a Crofer22APU sheet.

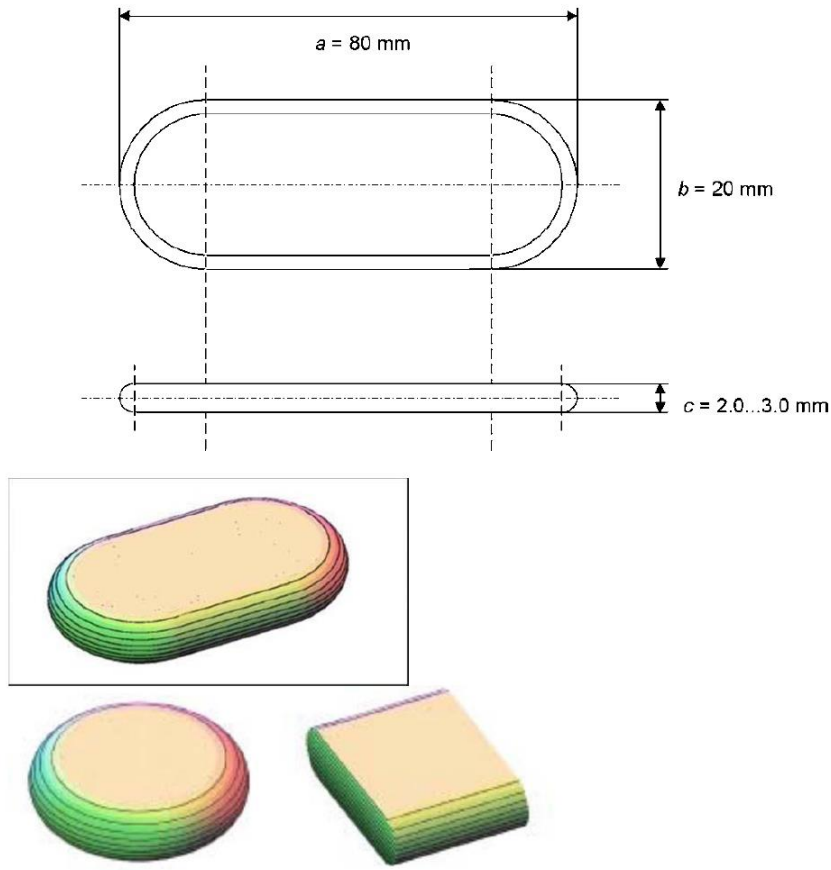

Fig. 3.1. Geometry and dimension of the specimen used for the evaporation experiment [97].

Bath composition	
$CoCl_2 \cdot {}_6H_2O$	100 g
H_3BO_3	35 g
Distilled water	1000 ml
Solution conditions	
pH	3 ~ 3.5
Temperature	25 °C
Operating conditions	
Current density	64 mA/cm^2
Pulse time	0.008 sec. On
	0.002 sec. Off
Operating time	40 sec.

Table 3.2. Electroplating parameters for the Co deposition on Crofer22 APU.

a)

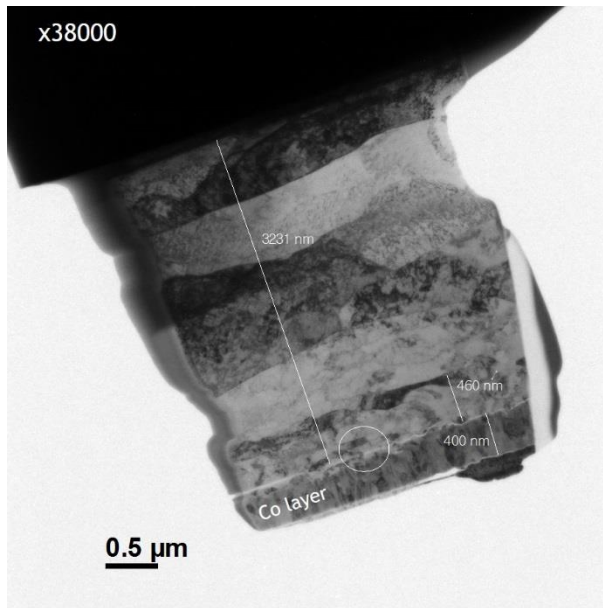

b)

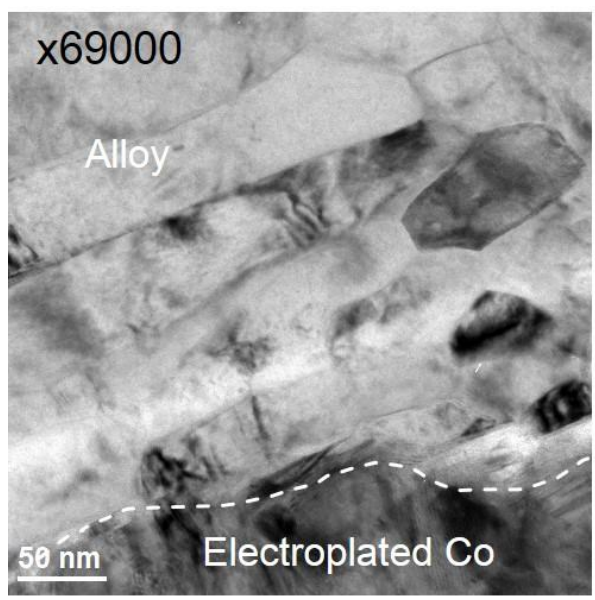

Fig. 3.2. Cross-sectional TEM images of the as-coated Crofer22APU. Fig. 12 b) is the magnified view of the circled area in Fig. 12 a).

3.2 Oxidation and evaporation test

Oxidation and evaporation experiments were carried out in a tubular furnace under a SOFC cathodic (oxidizing) condition at a temperature of 800 °C. The schematic illustration of the experimental setting is given in Fig. 3.3. Using laboratory air as carrier gas, air + 2 % H_2O, equivalent to p_{H_2O}= 2000 Pa (T = 25 °C, RH = 63 %), was prepared by the bubbling chamber coupled with a thermostat. The condition of the humidified air was constantly monitored by a thermo-hygrometer (TH200, KIMO Instruments, France) before injection. The flow rate was fixed at 2000 ml/min in order to eliminate the effect of the flow rate on evaporation kinetics [28, 35, 99].

A transpiration method was employed to investigate the oxidation and evaporation behavior of two different samples for Part A and B. The experiment consists of two processes: firstly, the gaseous Cr species released from the sample is condensed in 'Raschig ring' pieces placed in the tube outlet and, secondly, actual measurement is performed using an inductively coupled plasma optical emission spectrometer (ICP-OES, Varian 720-ES, Varian Inc., USA).

The intervals of cyclic oxidation for the weight gain test were determined identically to the evaporation test. After each period of cyclic oxidation, the samples were removed from the tube and cooled to room temperature in air. The weight gain was manually recorded using a high precision microbalance (Cubis® Micro Balance MSE3.6P, Sartorius, Germany) with an accuracy of ±0.002 mg.

The evaporation experiments were conducted at 800 °C and stopped every 100 h except for the first cycle at 50 h. Tubular Raschig rings were crushed to a sieve mesh size of 10 (aperture size = 2.00 mm). On average, 220 ~ 230 g of the Raschig ring pieces were placed in a quartz tube outlet where the temperature was maintained at 25 °C. The quantification of the collected volatile species was conducted by inductively coupled plasma optical emission spectrometer (ICP-OES, Varian 720-

ES, Varian Inc., USA). Before actual measurement by ICP-OES, the Raschig ring pieces were pre-treated by high purity nitric acid for extraction. Blank tests for the solution were executed to assure that the solution was free of the elements of interest. Five different bare specimens were experimented for 24 h in order confirm with the reproducibility of our apparatus. The average amount of Cr release per unit area was 2.23×10^{-6} g·cm^{-2} with a standard deviation of 1.63×10^{-7} g·cm^{-2}, equivalents to an error range of ±8.18 %.

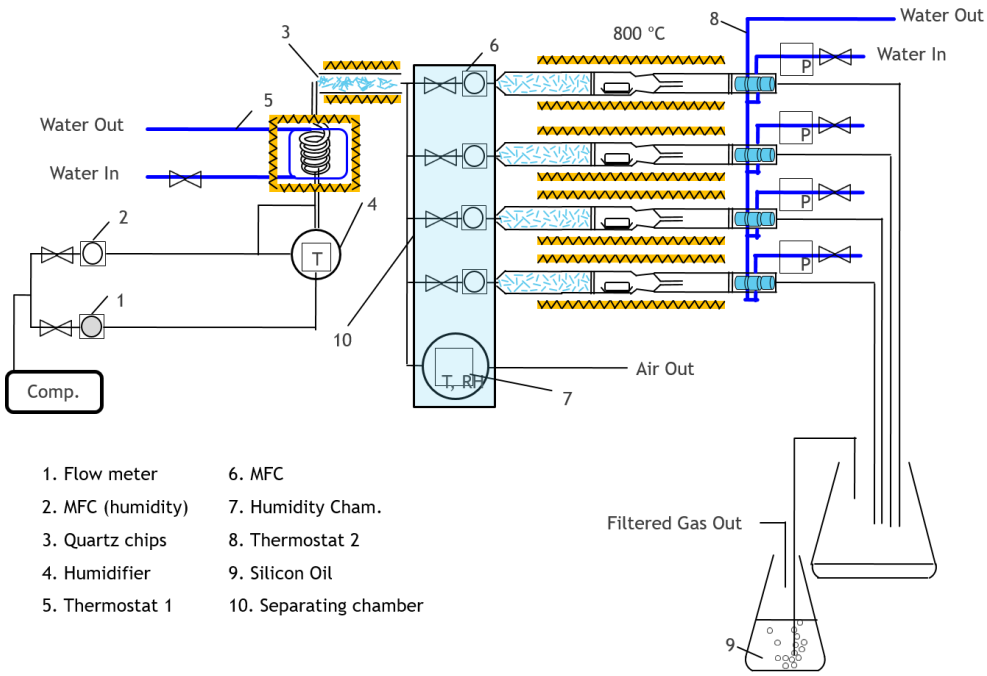

Fig. 3.3. Schematic illustration of the apparatus setup for the oxidation and evaporation experiments.

3.3 Microstructure analysis

3.3.1 Part A

Microstructure analysis was conducted on the as-received samples using an electron backscattered diffraction (EBSD) detector (*e*-Flash^{HR}, Bruker Nano GmbH, Germany). The normal direction plane of samples for EBSD analysis were mechanically polished to 500 (P-1000) grit SiC abrasive paper, followed by electropolishing using an electrolyte solution composed of nitric acid and methanol in the ratio of 60:40. The results of EBSD analysis were post-processed for grain size measurement and GB characterization using Bruker Esprit 2.1 and TSL OIM analysis software 7.0.

A cross-sectional ion milling system (E-3500, Hitachi, Japan) was employed to observe the cross sections of the oxidized samples. The samples for transmission electron microscopy (TEM) analysis were prepared from the oxidized samples using a dual beam focused ion beam (FIB) system (Helios NanoLab, FEI company, USA). Supplementary cross-sectional observations were also performed on the same FIB system. The TEM samples were explored using a chemical analysis dedicated TEM system (Talos F-200X, FEI company, USA), equipped with a high-speed energy dispersive X-ray spectroscopy (EDS) system (Super-X, Bruker Nano GmbH, Germany).

The oxide scale emergent from the GBs of the alloys and corresponding GBs were characterized by a simultaneous EBSD-EDS technique using a field emission scanning electron microscope (S-4300 SE, Hitachi, Japan), equipped with a EBSD-EDS system (*e*-Flash^{HR} and X-Flash, Bruker Nano GmbH, Germany) [100]. To accurately analyze the nanoscale grain size of the oxide scale, transmission Kikuchi diffraction (TKD) [101] was performed on a number of the oxide lamellae prepared

by FIB. The same EBSD system equipped with a horizontal TKD detector head (Optimus, Bruker Nano GmbH, Germany) was used to reduce acquisition time with augmented EBSD signals.

All the thermodynamic information given in this study was computed using FactSage 7.1 thermochemical software. The database used for computation are 'FTOxid', 'FactPS' and 'FSStel' [102, 103].

3.3.2 Part B

Preliminary oxide characterization was performed by XRD and simultaneous electron backscattered diffraction-energy dispersive X-ray spectroscopy (EBSD-EDS) to classify types of oxides formed on the bare and coated specimen [100]. XRD analysis was carried out on Advance D8 equipped with a Sol-X detector (Bruker Nano GmbH, Germany) which reduces the background by fluorescence. The analysis was complemented by simultaneous EBSD-EDS conducted at an acceleration voltage of 20 kV, using field emission SEM (S-4300 SE, Hitachi, Japan) equipped with a EBSD-EDS system (*e*-Flash^{HR} and X-Flash, Bruker Nano GmbH, Germany) [100].

Consecutive out-plane XRD analysis was also carried out for the sole coated specimen oxidized in stages, using Advance D8 diffractometer, equipped with LynxEye detector (Bruker Nano GmbH, Germany) and a Cu target (Cu Kα radiation, $\lambda = 0.154056$ nm). Intensity data was acquired in the 2θ range of 10 to 100° with an angle increment of 0.02° and time step of 4 seconds.

The oxide layer of the coated specimen tested for 500 h was more thoroughly characterized by TEM (Titan, FEI company, USA), operating at an acceleration voltage of 300 kV. Indexing the experimental selected area diffraction pattern (SADP) was facilitated by the JEMS software which simulates the SADPs of candidate oxides. To examine the compositional change over increasing oxidation time, four different coated specimens were separately exposed to the same experimental condition for varying exposure periods: 10, 50, 200, and 500 h. For designated TEM sampling, wide range SEM observations were carried out from ion-milled specimens prepared by a cross-sectional ion milling system (E-3500, Hitachi, Japan), and then TEM samples were collected from desired areas by a dual beam focused ion beam (FIB) system (Helios NanoLab, FEI company, USA). These samples were explored

on a chemical analysis dedicated TEM system (Talos F-200X, FEI company, USA), equipped with a high-speed EDS system (Super-X, Bruker Nano GmbH, Germany). The TEM system is composed of 4 windowless silicon drift detectors and shutters integrated into the objective lens. All the compositional data obtained on TEM-EDS were quantified by atomic percent normalization. Moreover, a set of the EDS mapping data was post-processed using 'Feature (phase analysis program)' embedded in ESprit 1.9 (Bruker Nano GmbH, Germany) for more inclusive presentation rather than a conventional element-based one [104]. As a result, color-coded phase classification by region became available, allowing effective qualitative comparison between the selected oxidation periods. Thermodynamic data was computed to complement our observations when relevant databases were available. A thermodynamic analysis on the stability of oxide formation was performed using FactSage 6.4, thermochemical software [103].

Chapter 4.

Part A: Effect of alloy grain size on oxidation behavior

4.1 Results

4.1.1 Grain size and GB length of parent alloy

The grain size and GB length of the as-received samples was evaluated using EBSD analysis. Fig. 4.1 compares the microstructure of Crofer22APU sheet (Crofer-S) with that of Crofer22APU plate (Crofer-P), indicating low angle (5º ~ 15º) and high angle (> 15º) random GBs in line with coincidence site lattice (CSL or ∑) boundaries. The CSL boundaries were identified according to the Brandon criterion [105]. The results of the EBSD analysis are summarized in Table 4.1.

The average grain size of Crofer-S was found to be, approximately, 26 times smaller than that of Crofer-P. Since surface ridge formation distinctively turned out from the GBs of the alloy, the GB length was also calculated and then normalized by the analyzed area to correlate it with long-term oxidation behavior. Assuming that the GB width was 0.5 nm [106], the GB area fraction of Crofer-S was calculated to be 22 times greater than that of Crofer-P.

The influence of GB characteristics on the surface ridge formation must be considered because GB diffusivities depend on the disorientation angle and fraction of the coincident lattice site [13, 107]. Zhu et al. qualitatively and semi-statistically showed that the scale ridge formation became more pronounced on the high angle GBs (> 15º) and CSL boundaries exceeding ∑19 when a Fe-22 wt. % alloy was oxidized at 800 °C in stagnant dry air [22]. Accordingly, only the GBs with the

aforementioned characteristics were taken into account for the statistical evaluation of GBs.

a)

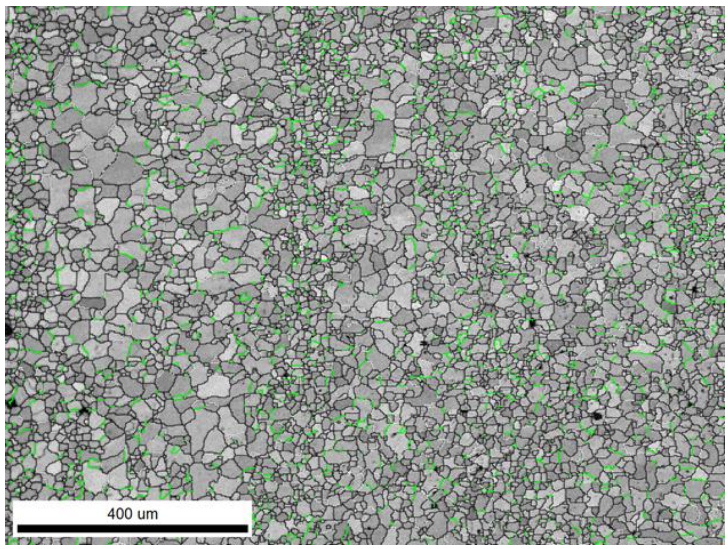

b)

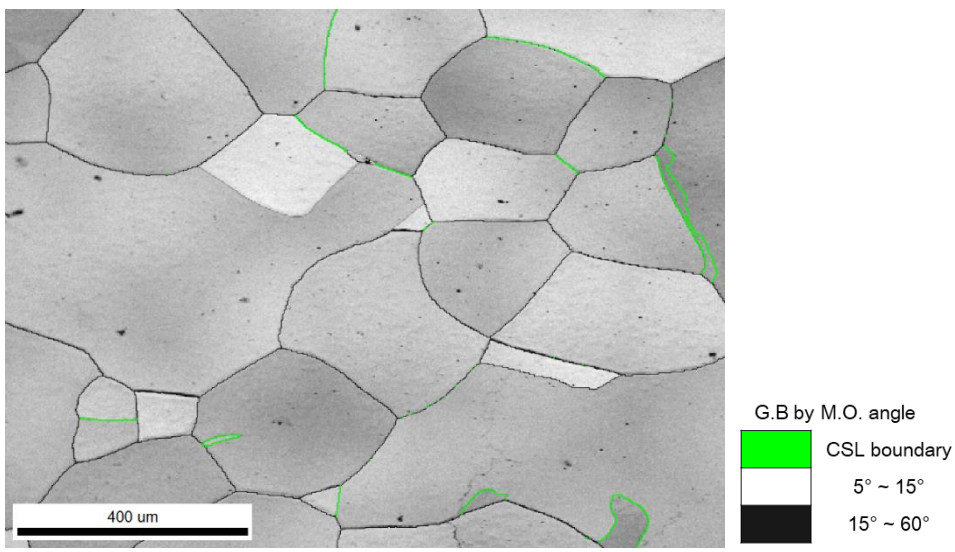

Fig. 4.1. Comparison of the image quality (IQ) maps of a) Crofer-S and b) Crofer-P. Both IQ maps were acquired at the same magnification. The red and black line indicates low angle random GBs and high angle random GBs, respectively, while the yellow line represents CSL boundaries

	Grain size (μm)	Total grain counted	GB length normalized by area* (μm-1)
Crofer-S	19.7	1473	1.77E-01
Crofer-P	511.5	1030	8.18E-03
	CSL boundary fraction** (%)	CSL boundary area density (μm-1)	GB area fraction*** (%)
Crofer-S	8.8	1.56E-02	8.07E-05
Crofer-P	5.1	4.17E-04	3.88E-06

* Disorientation angles greater than 15° were only considered for calculation.
** $\sum 3 \sim \sum 19$ were considered for calculation.
*** The GB width was assumed to be 0.5 nm and the CSL boundary area density was subdued from GB length area density.

Table 4.1. Statistical results obtained from the EBSD analysis with regard to the grain size and GB length of Crofer-S and Crofer-P.

4.1.2 Weight gain and evaporation test

The rectangular samples of Crofer-S and Crofer-P were subject to cyclic oxidation at 800 °C in the dynamic air + 2 % H_2O condition for a total accumulative time of 700 h. No spallation was observed during both cooling and weighing. The oxidized samples were weighed at least five times to ensure reproducibility. The result of the weight gain test is presented in Fig. 4.2. Crofer-P showed the lower oxidation rate than Crofer-S. The weight gain rate of both samples obeyed the parabolic rate law and so can be fitted to the relationship given below.

$$\left(\frac{WG}{Area}\right)^{\mathbf{2}} = k_w t \tag{4.1}$$

where k_w is the parabolic constant and t is time. The k_w of Crofer-S and Crofer-P was calculated to be 4.424e-8 and 2.592e-8 $mg^2 \cdot cm^{-4} \cdot s^{-1}$, respectively; the rates differed by approximately 38 %. The results of the EBSD analysis in Section 4.1.1 and weight gain test signify that the oxidation behavior of Crofer22 APU is connected with the alloy grain size, or GB length.

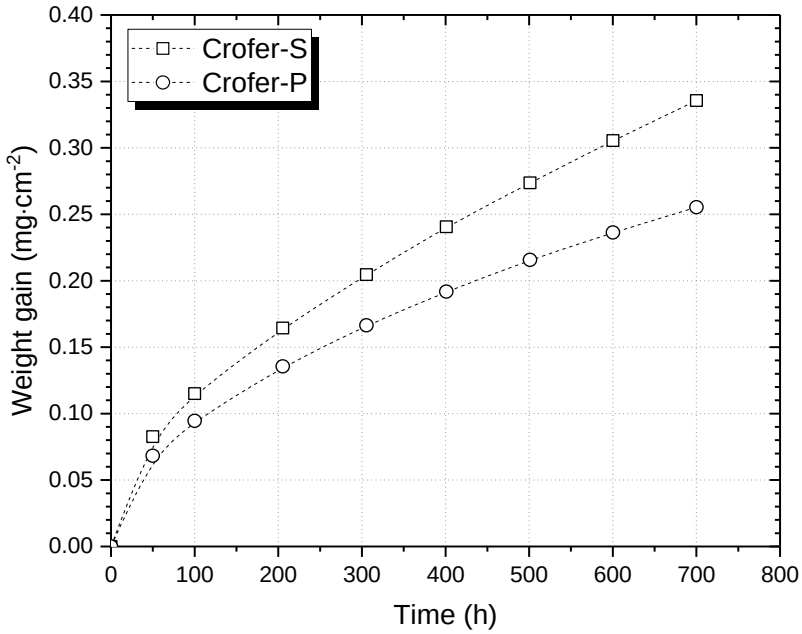

Fig. 4.2. Result of the weight gain test to compare the oxidation rate of Crofer-S and Crofer-P. The samples were exposed to a humid air (2 % H_2O) flow with a flow rate of 2000 ml·min^{-1} at 800 °C for a total of 700 h.

4.1.3 Characterization of oxide and alloy GB

Plan-view observation using SEM was first conducted to investigate the surface morphology of the samples oxidized for 300 h. Fig. 4.3 shows that, on both samples, discernible scale ridge formation locally occurred from certain areas, highly suspected to be the GBs of the parent alloy. To verify that scale ridges originate from GBs of the parent alloy, cross-sectional observation using FIB was performed on the sample of Crofer-S oxidized for 300 h. Fig. 4.4 confirms that scale ridges indeed emerged from GBs of the parent alloy. It was also noticed that intergranular oxidation was manifested beneath the scale surface ridge, forming a round-shaped oxide scale on a micro scale.

For more thorough compositional and crystallographic characterization of the oxide layer and intergranular oxide scale, TEM analysis was carried out on the lamella of the oxide layer formed on Crofer-S after 300 h oxidization. As presented in Fig. 4.5 a) and b), the surface oxide layer consisted of a continuous Cr_2O_3 layer overlaid with a $MnCr_2O_4$ layer on top while the intergranular oxide scale was chemically identified as $MnCr_2O_4$ that resembles the superficial oxide layer. The bright field TEM image and diffraction pattern given in Fig. 4.5 c) reveal that the intergranular oxide scale had a spinel structure and that it was composed of one large grain and some subordinate smaller grains.

The simultaneous EBSD-EDS analysis in cross section was utilized to characterize the underlying GB below a surface ridge. A set of the example EBSD-EDS images is given in Fig. 4.6 and the respective disorientation angles between the marked grains are summarized in Table 4.2. More than 30 scale ridge segments accompanied with intergranular oxide precipitates were examined in the same manner. This analysis consequently provided semi-statistical information on the orientation relation between a couple of grains either surrounding a channel of intergranular

oxide or forming a triple point junction (TPJ) with an intergranular oxide front. Readers are advised to consult the alphabetical marks in Fig. 4.6 to grasp the following results.

- GBs of the grains forming a TPJ with an oxide front were always characterized as non-special high angle GBs. This finding corresponds to the grains indicated by capitals. There was only one exceptional case where intergranular oxidation proceeded along the ∑19 GB.
- Most of the grains enveloping channels of the intergranular oxide have a disorientation angle > 15º. The GBs of these grains are apparently judged as the place where intergranular oxidation initiated.
- Volume expansion due to formation of the intergranular oxide plastically deformed some areas of the surface grains adjacent to GBs. Such phenomenon is well exemplified by the 'I' and 'e' grains in Fig. 4.6. Most of the mechanically rotated grain formed a new GB with a disorientation angle < 15º. Some of the mechanically induced GBs were identified as the non-special high angle GBs, which implies that the newly formed GBs did not act as preferential oxidation sites for intergranular oxidation.

Overall, the above findings indicate that non-special high angle GBs are the cornerstone of intergranular oxidation assisting the formation of more volumetrically pronounced scale ridges.

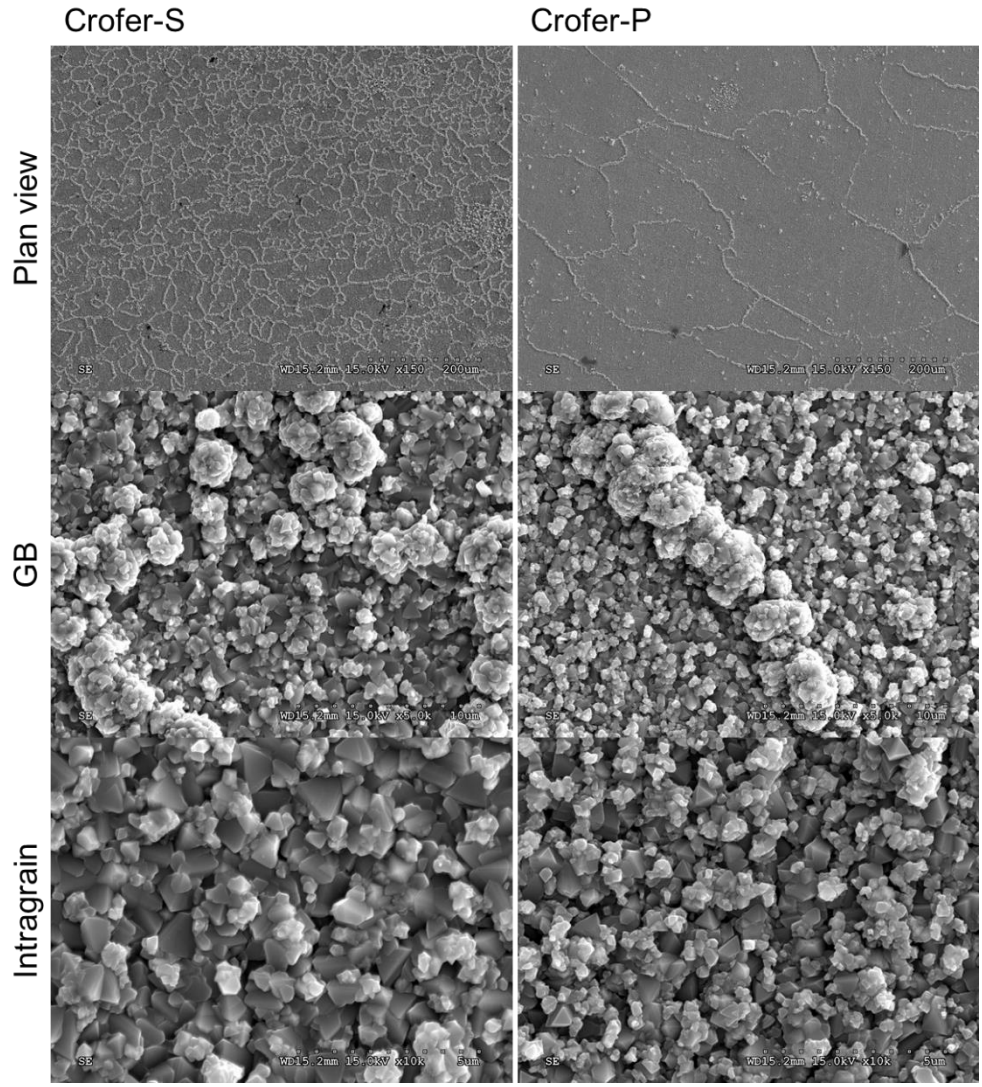

Fig. 4.3. Plan-view observations of Crofer-S and Crofer-P after 300 h of cyclic oxidization. The magnification of each set of the images was intended to be coincident to assure qualitative comparison.

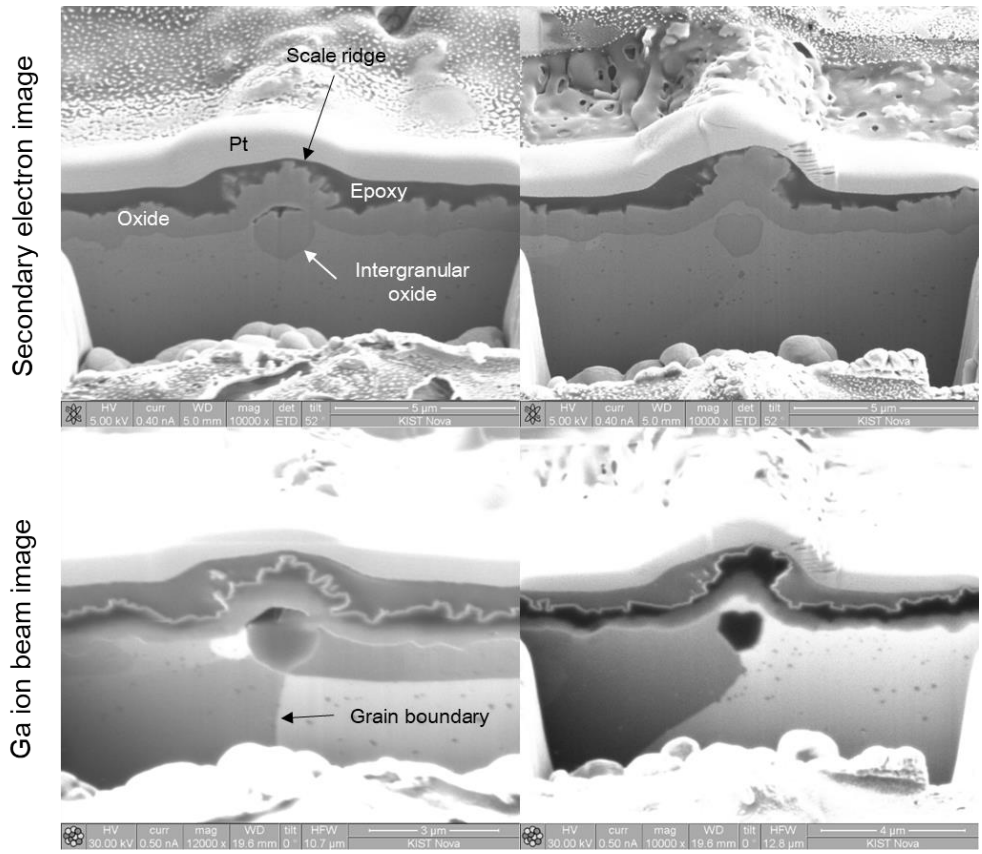

Fig. 4.4. Cross-sectional observation of the scale ridges on Crofer-S after 300 h of cyclic oxidization. A secondary electron image is presented along with a Ga ion beam image to clearly demonstrate the underlying GBs of the parent alloy.

a)

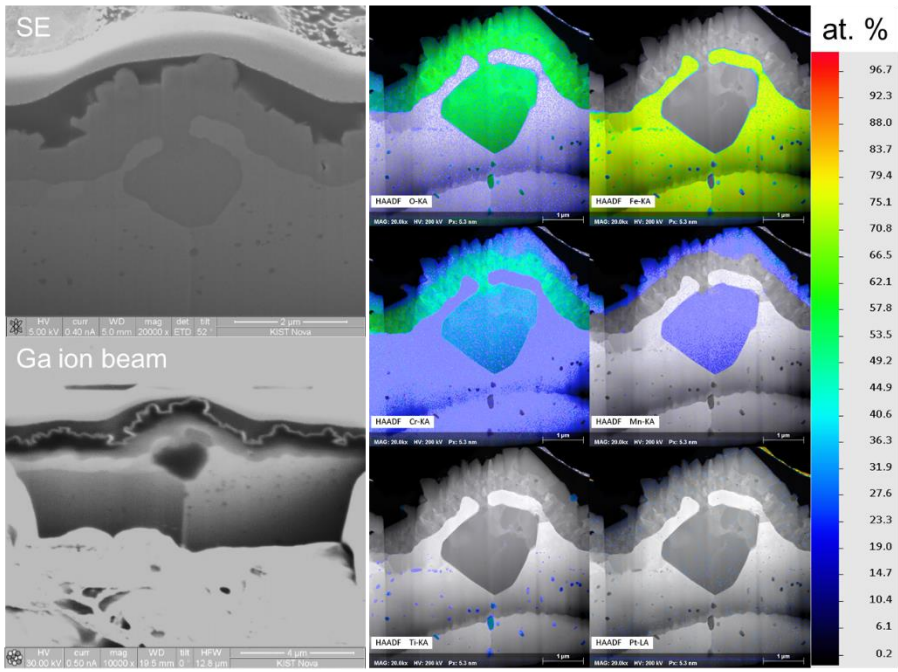
SE
Ga ion beam
HAADF O-KA
HAADF Fe-KA
HAADF Cr-KA
HAADF Mn-KA
HAADF Ti-KA
HAADF Pt-LA
at. %
96.7
92.3
88.0
83.7
79.4
75.1
70.8
66.5
62.1
57.8
53.5
49.2
44.9
40.6
36.3
31.9
27.6
23.3
19.0
14.7
10.4
6.1
0.2

b)

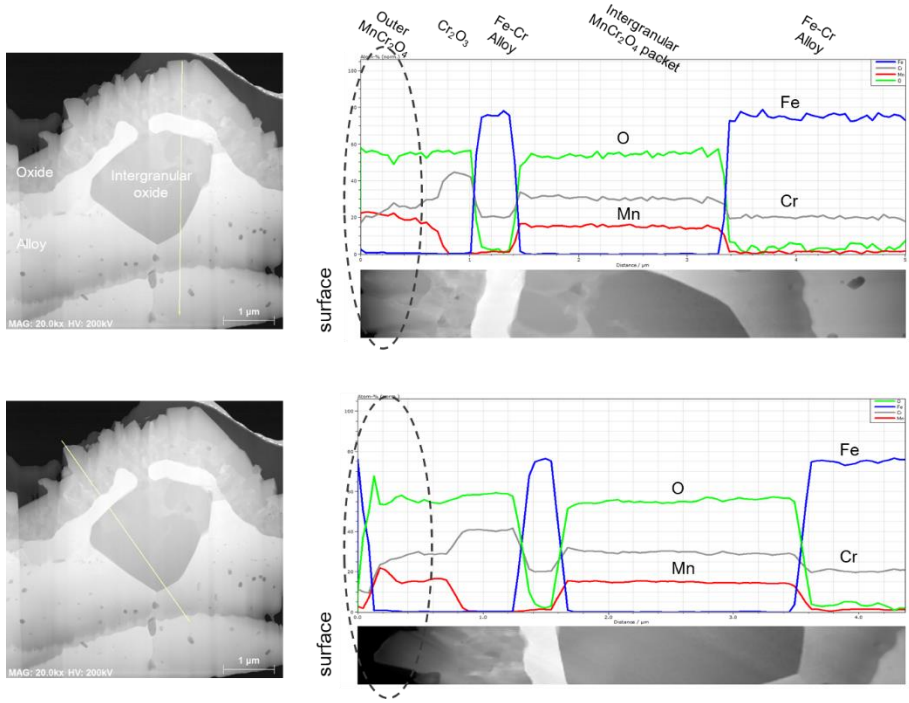
Oxide
Intergranular oxide
Alloy
Outer $MnCr_2O_4$
Cr_2O_3
Fe-Cr Alloy
Intergranular $MnCr_2O_4$ packet
Fe-Cr Alloy
Fe
O
Cr
Mn
surface

c)

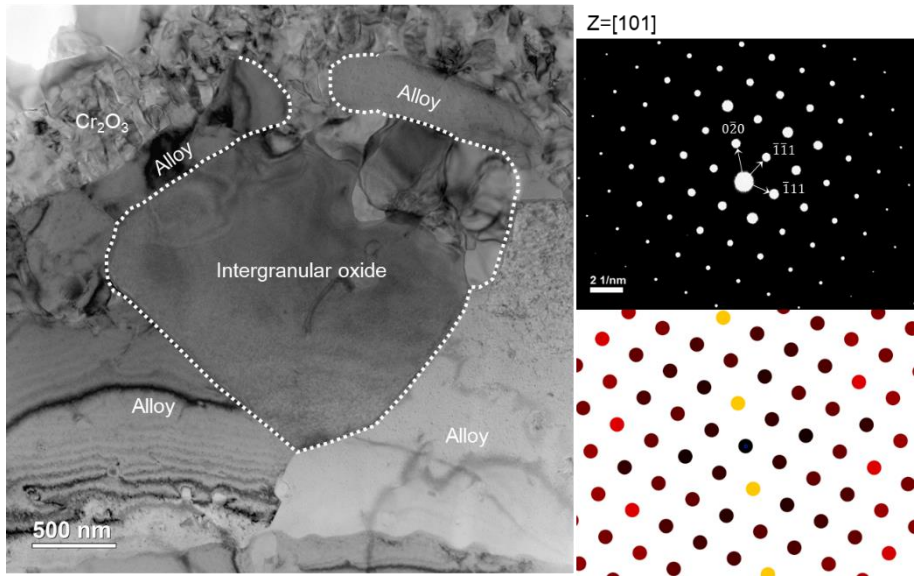

Fig. 4.5. Result of the TEM-EDS analysis: a) quantified composition mapping in scanning TEM mode; b) compositional line profiling; c) structural analysis in TEM mode. The sample of Crofer-S oxidized for 300 h was used for the analysis. The theoretical selected area diffraction pattern (SADP) of spinel $MnCr_2O_4$ in Z=[101] was simulated using JEMS software to index the experimental SADP.

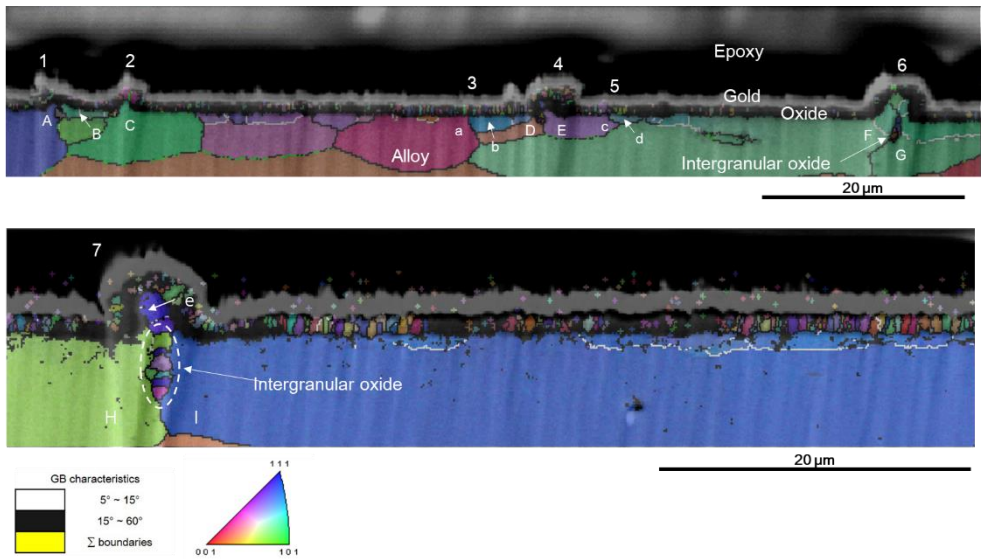

Fig. 4.6. Result of the simultaneous EBSD-EDS analysis in cross section. The sample of Crofer-S oxidized for 700 h was used for the analysis. A SE image and image quality map are superimposed onto an inverse pole figure map (Z-direction) for inclusive presentation. Limited areas of the oxide layer and intergranular oxide scale were indexable due to small grain size which cannot be resolved at given magnifications. The summary of GB characterization is tabulated in Table 4.2.

Ridge number	Grain ID	Disorientation angle	Note
1	A-B	51.1°	
2	B-C	45.2°	
3	a-b	54.4°	No protrusion
4	D-E	48.7°	
5	c-d	19.0°	No protrusion
6	F-G	41.0°	
7	H-e	33.7°	
	H-I	36.2°	
	I-e	5.9°	

Table 4.2. Summary of the characterization of the GBs in connection with the surface scale ridge and intergranular oxide.

4.2 Discussion

4.2.1 Effect of intergranular oxidation on oxidation behavior

This section addresses why the decrease in both weight gain and Cr release of Crofer-P mainly arise from the phenomena pertaining to the GBs of the base alloy.

The microstructure analysis revealed that the GBs of the base alloy near the surface is to be an additional oxidation site where the predominant increase in the value of k_w is ascribed. In the former study concerning the effect of varying heat treatment periods on the oxidation behavior of Crofer22 APU, Magdefrau et al. also reported the comparable experimental result that the larger alloy grain size lead to a reduction in a oxidation rate at 800 ºC in dry air [23]. Nonetheless, they interpreted the reduced oxidation rate in terms of intragranular outer oxidation rather than the oxidation associated with alloy GBs. Thus, the investigations of the intragranular surface oxide layers was carried out to determine which one plays a more decisive role in the present study.

For semi-statistical, quantitative comparison, the average thickness of the intragranular oxide layers of Crofer-S and Crofer-P was estimated from cross-sectional BSE images. Fig. 4.7 shows a set of examples demonstrating the methodology. Due to a difference in Z-contrast in the BSE image, employing PhotoshopGS explicitly enabled the extraction of the images pixels corresponding to a dual phase oxide layer composed of Cr_2O_3 and $MnCr_2O_4$. Dividing a total number of the pixels by a horizontal field of view yields more reliable average layer thickness. After oxidation of 700 h, Crofer-P was found to form a marginally thicker oxide layer than Crofer-S with a difference of 50 nm, equivalent to 3 %.

One may claim that even a difference of 3 % in the average thickness could largely contribute to the reduced oxidation rate in that intergranular regions take up most of

the oxidation surface. To evaluate the influence of the thickness difference on the oxidation behavior, the experimental k_w of oxide, $A_xB_yO_z$, is converted to k_p as [57]

$$k_p = \frac{1}{2}\left(\frac{MW_{oxide}}{z\ MW_O\ \rho_{oxide}}\right)^2 k_w \tag{4.2}$$

where k_p is

$$x^2 = 2k_p t \tag{4.3}$$

In this study, both Crofer-S and Crofer-P formed a duplex, partitioned intragranular oxide layer and so Eq. (4.2) is modified as

$$k_p = \frac{1}{2}\left[f\left(\frac{MW_{Cr_2O_3}}{z\ MW_O\ \rho_{Cr_2O_3}}\right) + (1-f)\left(\frac{MW_{MnCr_2O_4}}{z\ MW_O\ \rho_{MnCr_2O_4}}\right)\right] k_w \tag{4.4}$$

where *MW* stands for molar weight, ρ is density, and *f* is the area fraction of Cr_2O_3 which can be determined from TKD analysis. Using Eq. (4.3) and (4.4), the experimental *x* was converted to a theoretical k_w. A theoretical *x* was also calculated reversely from the experimental k_w for complementary comparison. Note that Eq. (4.2)-(4.4) assume the absence of alloy GBs, or single crystal, and thus that the calculated values were somewhat overestimated. However, the results in Table 4.3 still show that a difference of 3 % in the oxide layer thickness accounts for a difference of 5.5 % in the weight gain at most. Consequently, the GB oxidation phenomena is highly suspected to be the most influential factor leading to the increased weight gain

When the thickness of an oxide layer is assumed the same, the grain size of outer $MnCr_2O_4$ is another effective figure reflective of an oxide growth because the GB of polycrystalline Cr_2O_3 and $MnCr_2O_4$ is a fast diffusion path for Cr, Mn and O [108-111]. Furthermore, the grain size of $MnCr_2O_4$ is associated with initial oxidation behavior (e.g. the nucleation rate of Cr_2O_3) since the nucleation of $MnCr_2O_4$ commences on top of initially formed Cr_2O_3 with an increasing Mn content [112, 113]. For instance, Magdefrau et al. qualitatively elucidated the change in the oxidation kinetics of Crofer22APU in light of the grain size of outermost $MnCr_2O_4$ [23], but their interpretation solely relied on the morphological observations of $MnCr_2O_4$ and initial Cr_2O_3 formed after 5 h of oxidation.

To provide more rigorous and quantitative data, the grain size of $MnCr_2O_4$ was quantified in cross section using TKD. As demonstrated in Fig. 4.8, the grain size of $MnCr_2O_4$ formed on two specimens differ by only 40 nm, equivalent to a difference of 7 %. This is another corroborating evidence confirming that the influence of intragranular oxidation is of insignificance.

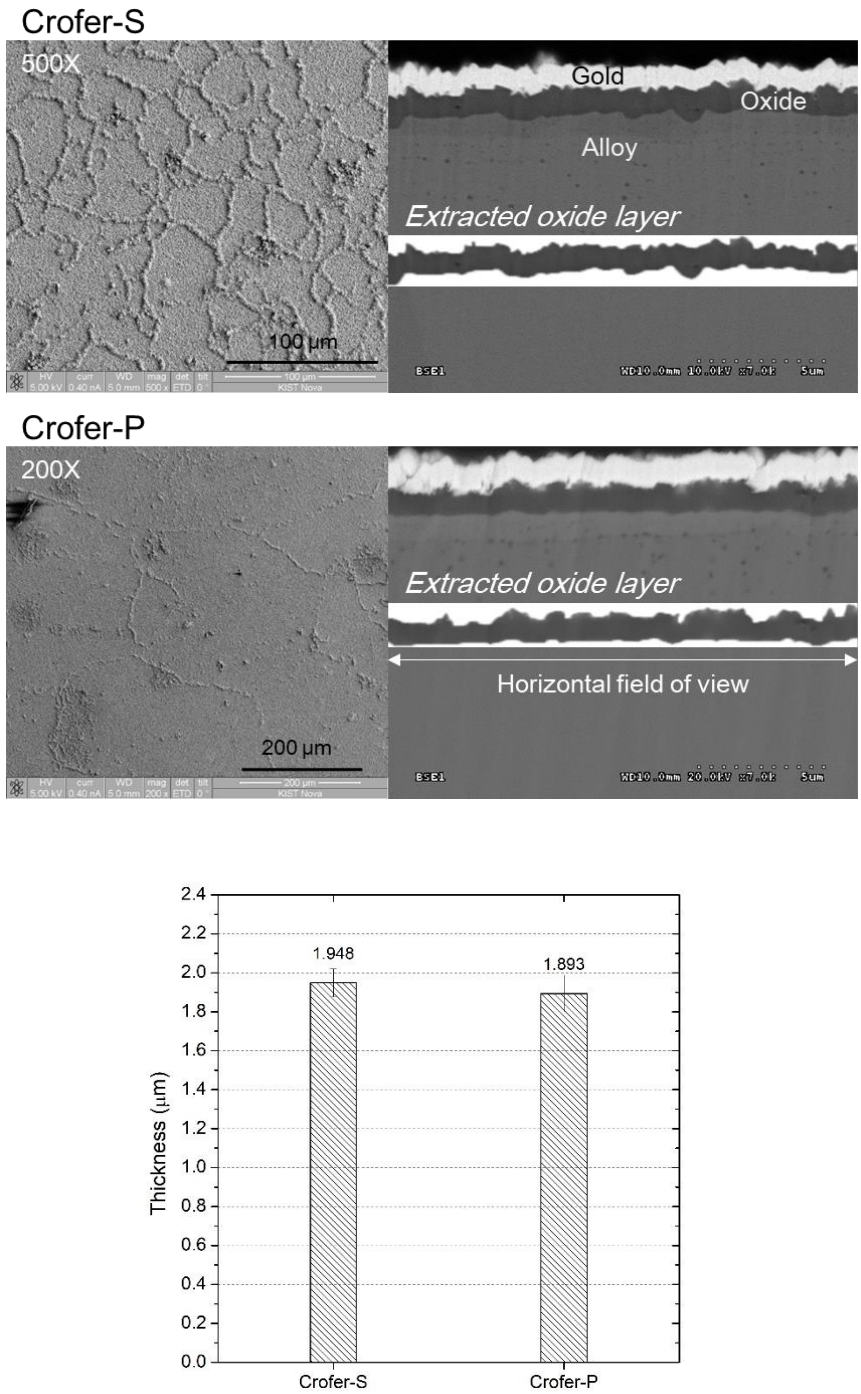

Fig. 4.7. Comparison of the thickness of the intragranular oxide layer.

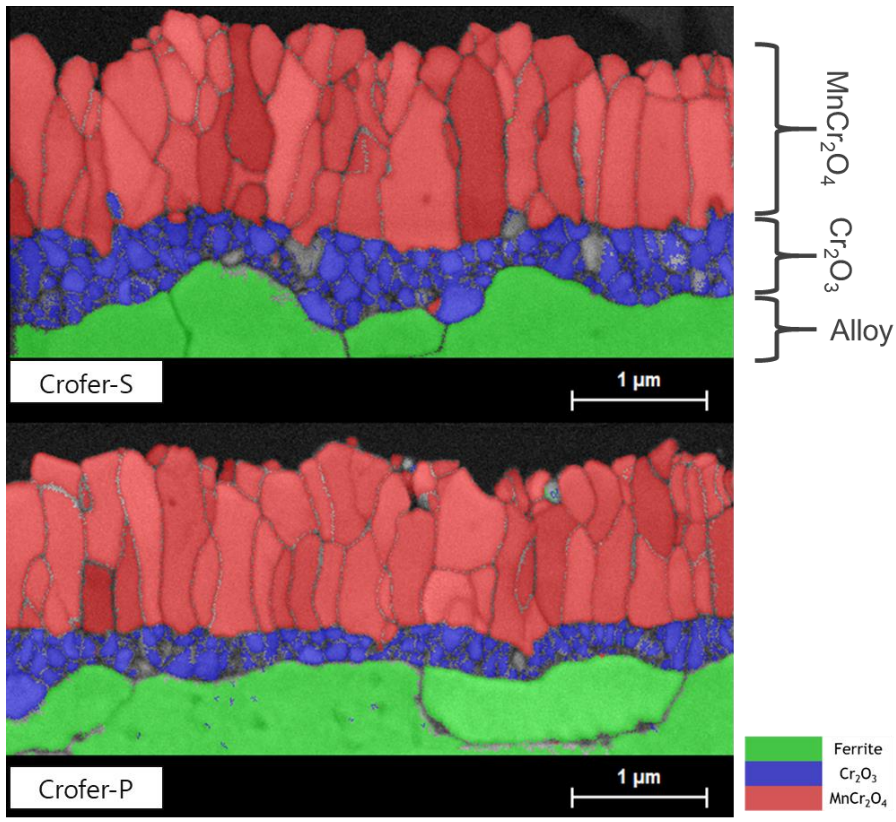

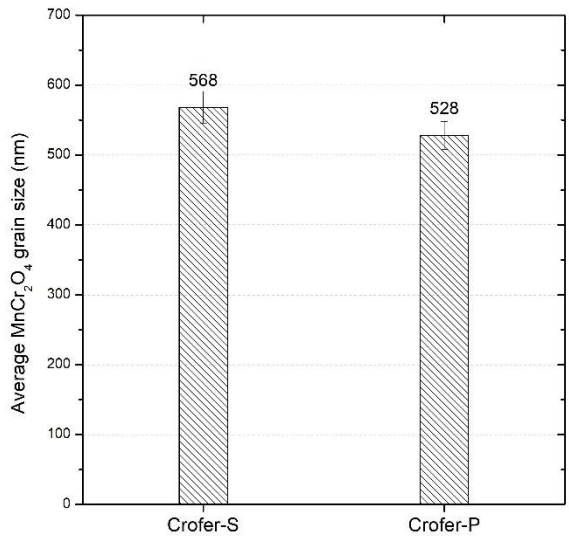

Fig. 4.8. Comparison of the average grain size of spinel $MnCr_2O_4$.

	a) Experimental k_w ($mg^2/cm^4/s$)	b) Converted k_p (cm^2/s)	c) Calculated x (μm)
Crofer-S	4.42E-08	1.52E-14	2.77
Crofer-P	2.83E-08	9.72E-15	2.21
Reduction ratio	35.9%	35.9%	20.2%

	d) Measured x (μm)	e) Calculated k_p (cm^2/s)	f) Converted k_w ($mg^2/cm^4/s$)
Crofer-S	1.95	7.53E-15	2.19E-08
Crofer-P	1.89	7.11E-15	2.07E-08
Reduction ratio	3.1%		5.5%

Table 4.3. Estimation of the theoretical parabolic constant (k_w) and oxide layer thickness (x). The values in column b) and c) were calculated from the experimental k_w in column a) while the values in e) and f) were figured out from the measured x in column d).

4.2.2 Prediction of oxygen partial pressure

The depth variation of oxygen partial pressure (pO_2) was predicted based on the combined results of oxide characterization in Section 3.3 and thermodynamic calculation using the FactSage thermochemical software. Fig. 4.9 a) presents the oxide phase diagram for one mole of 0.765Fe-0.23Cr-0.005Mn exposed to the experimental condition and Fig. 4.9 b) illustrates the schematic map of pO_2 levels where the observed oxide phases are thermodynamically favored.

The results indicate that the minimum pO_2 at the interface of the Cr_2O_3 and alloy is in an order of magnitude of 10^{-27} while the formation of $MnCr_2O_4$ requires a minimum pO_2 of 10^{-28}. The author attempted to cross-check the validity of the prediction using the internal Ti oxides observed underneath the Cr_2O_3 layer. The exact identification of the Ti oxides observed in this study is still in progress. Their size on the tens-of-nanometer scale [23, 24] and stoichiometric instability and structural variation of Ti oxide [114, 115] make it challenging to acquire reliable microstructure information (composition data and diffraction patterns) even with a conventional TEM. Therefore, the correspondence of the equilibrium pO_2 range associated with the Ti oxides will be deduced from the review of the literature and thermodynamic calculation.

Valence of Ti cations of Ti oxide are largely influenced by pO_2 [116]. This implies that its crystal structure and stoichiometry should vary with variations in pO_2. The phase transformation of Ti oxide dependent on pO_2 was simulated using FactSage as represented in Fig. 4.9 c). The dashed line at $\log(pO_2) \sim -28$ atm indicates where the Cr containing oxide is no longer thermodynamically stable. TiO dissociates at $\log(pO_2) \sim -43$ which enables the internal oxidation of Ti in the alloy matrix below Cr_2O_3. It is presumable from the simulation results that the observable types of internal Ti oxide are Ti_3O_5, Ti_2O_3 and TiO.

Froitzheim et al. briefly commented on internal oxidation of Ti in high Cr ferritic stainless steel, JS-3, which has the identical chemical composition to Crofer22APU [24]. On the basis of thermodynamics and compositional information from Ref. [117], they also conjectured that internally formable Ti oxide is either Ti_2O_3 or Ti_3O_5. More thorough TEM analysis for the internal Ti oxide in Crofer22 APU oxidized at 800 °C was carried out by Magdefrau et al. [23]. In their case, the diffraction pattern of the internal Ti oxide corresponded to that of monoclinic $TiO_{9.9\text{-}1.1}$ which is known to be stable below 990 °C [115]. Despite the fact that the Ti oxides of diverse polymorphs can be internally present under the present condition, it is noticeable that the likelihood of internal formation of TiO_2 is very remote and therefore the maximum pO_2 level at the interface of Cr_2O_3-alloy is estimated at less than $\log(pO_2) = -24$. Given that no $MnCr_2O_4$ was detected in the intragrain oxide scale, it is a plausible assertion that the pO_2 level over the alloy matrix be maintained below $\log(pO_2) \sim -28$.

A combination of the thermodynamic interpretation and oxide characterization from the literature review validates the credibility of the pO_2 map given in Fig. 4.9. The presence of internal Ti oxide is advantageous to more accurate inductive prediction of a change in pO_2. The author will elaborate on the pO_2 map in the future, relying on actual microstructure analysis of the Ti oxide observed in the present study.

a)

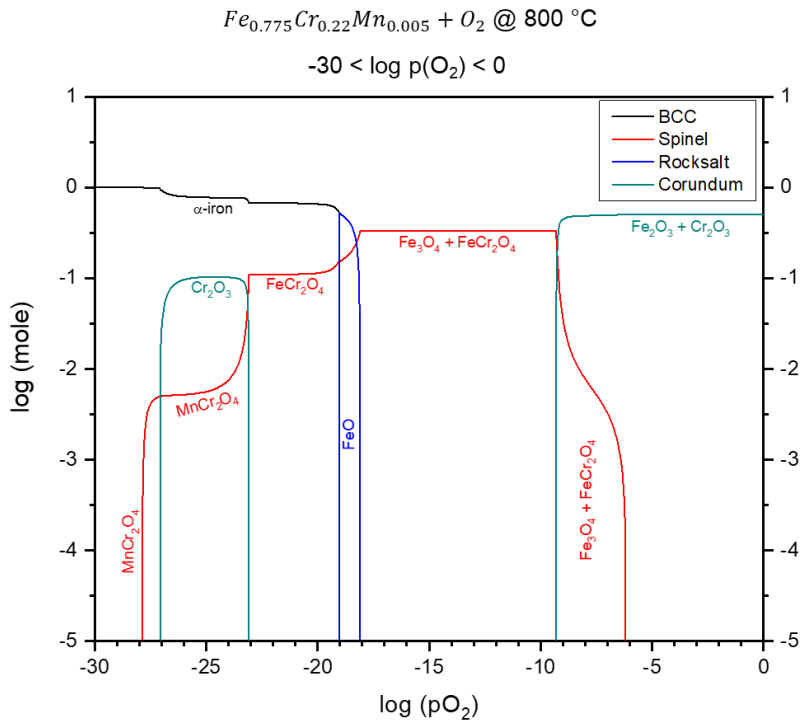
$Fe_{0.775}Cr_{0.22}Mn_{0.005} + O_2$ @ 800 °C
-30 < log p(O_2) < 0
BCC
Spinel
Rocksalt
Corundum
α-iron
Cr_2O_3
$FeCr_2O_4$
$Fe_3O_4 + FeCr_2O_4$
$Fe_2O_3 + Cr_2O_3$
$MnCr_2O_4$
$MnCr_2O_4$
FeO
$Fe_3O_4 + FeCr_2O_4$
log (mole)
log (pO_2)
1
0
-1
-2
-3
-4
-5
-30
-25
-20
-15
-10
-5
0

b)

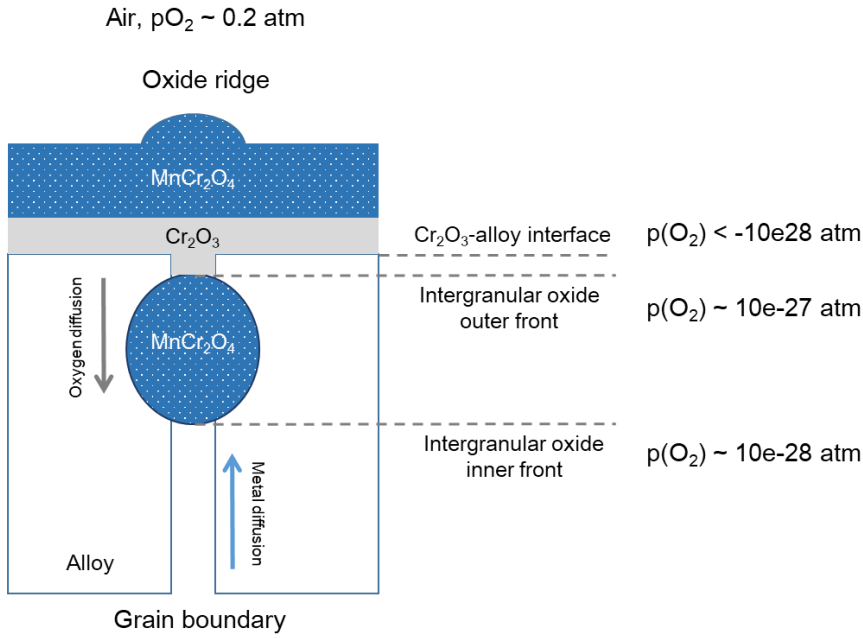
Air, pO_2 ~ 0.2 atm
Oxide ridge
$MnCr_2O_4$
Cr_2O_3
Cr_2O_3-alloy interface
$p(O_2)$ < -10e28 atm
Intergranular oxide outer front
$p(O_2)$ ~ 10e-27 atm
Oxygen diffusion
$MnCr_2O_4$
Intergranular oxide inner front
$p(O_2)$ ~ 10e-28 atm
Metal diffusion
Alloy
Grain boundary

c)

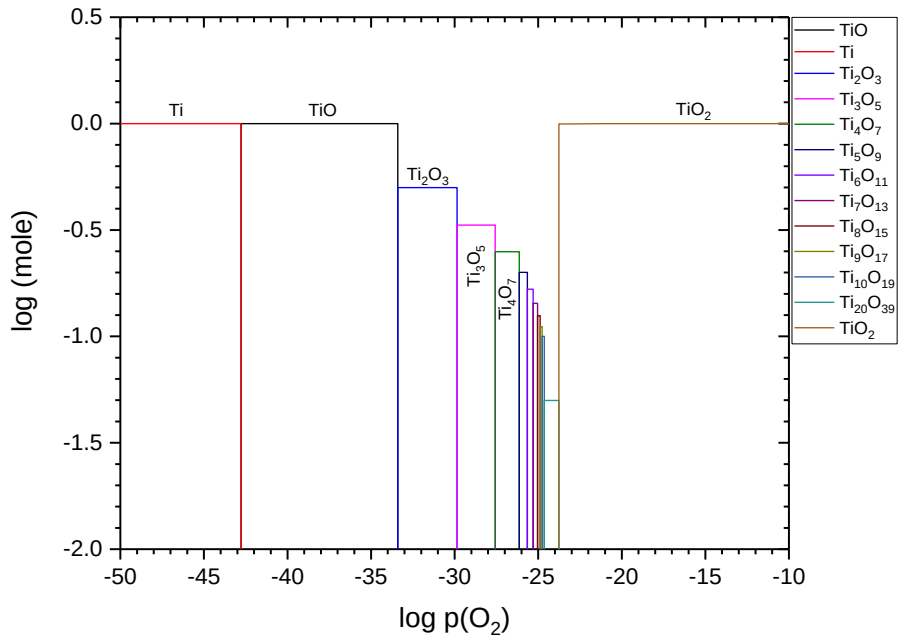

Fig. 4.9. Results of thermodynamic calculation: a) phase diagram showing the thermodynamic stability of oxides dependent on pO_2 levels, b) schematic illustration of the pO_2 levels corresponding to the observed oxide phase and c) stability of various Ti oxides dependent on pO_2.

Chapter 5.

Part B: Suppression of Cr evaporation by Co electroplating

5.1 Results

5.1.1 Evaporation behaviors of volatile Cr and Mn species

The accumulative amount of volatile Cr species released from the bare and Co coated sample is plotted in Fig. 5.1. The application criteria are set in accordance with one suggested by Stanislowski et al. [35, 36]. Co electroplating led to a ten-fold reduction in the Cr evaporation, meeting the standard for the mobile application. Fig. 5.2 demonstrates a time-dependent change in the evaporation rate of Cr and Mn gaseous species. Besides Cr and Mn, Co release was also traced for quantification by ICP-OES, but the outcome was negligible (< 1 μg). The evaporation of Cr and Mn followed a similar tendency, regardless of a surface state. Only the peak of evaporation was dependent on types of elements. The Cr evaporation has been most vigorous for the initial 50 h while the Mn evaporation rate reached a maximum at 100 h.

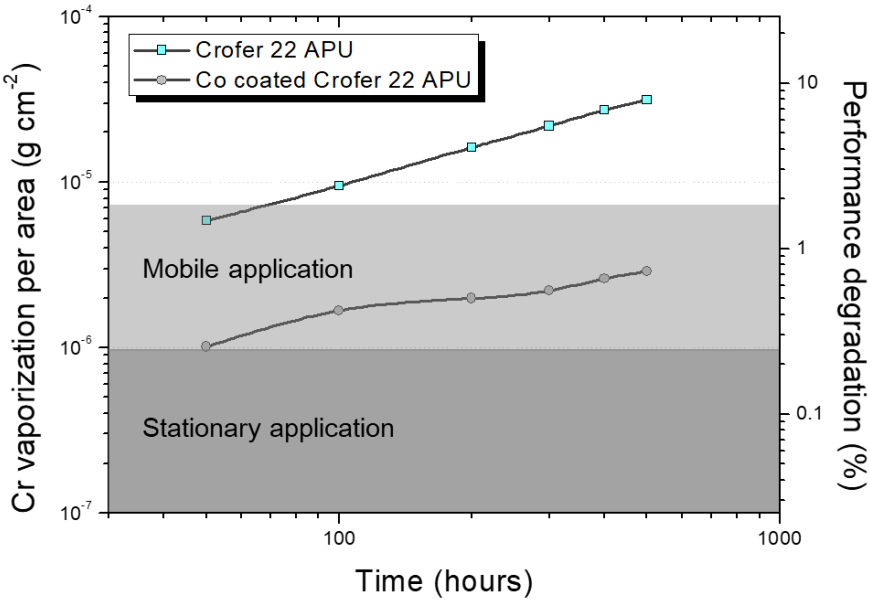

Fig. 5.1. Accumulative amount of Cr release from uncoated and Co-coated Crofer 22 APU sample as a function of test time. The measured value is normalized by the area of each sample. The rate of performance degradation is set up based on the empirical studies conducted in Research Center Jülich, Germany [35]. For mobile application, the performance degradation rate needs to be less than 2 % per 1,000 h while stationary application requires that the rate be less than 0.25 % per 1,000 h.

a)

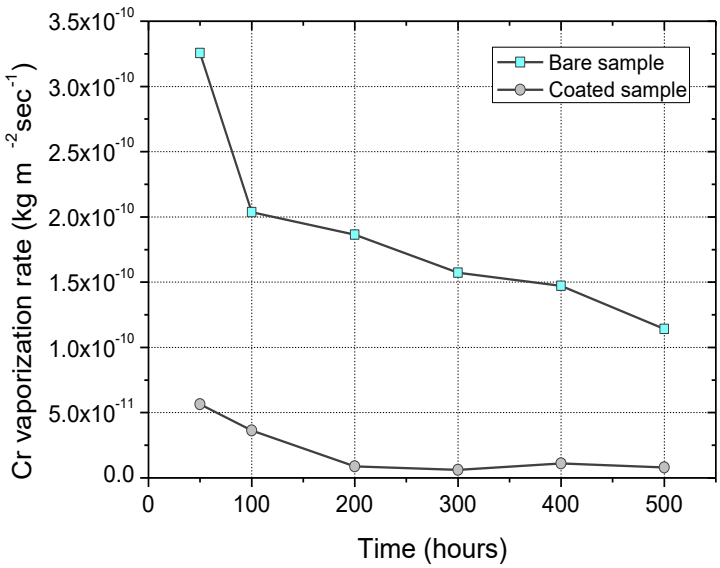

b)

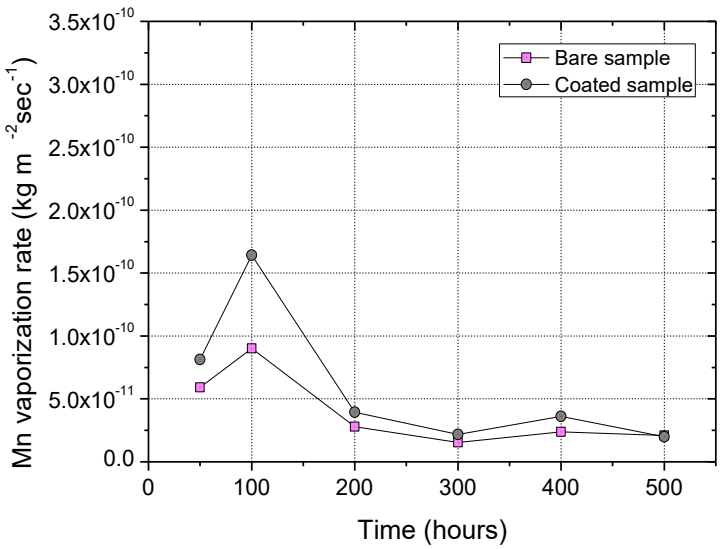

Fig. 5.2. Time-dependent change in the a) Cr and b) Mn vaporization rate for bare and Co-coated samples.

5.1.2 Oxide characterization of Co coated sample

There have been a number of reports with respect to the characterization of oxide layers formed on 23 ~ 24 wt. % Cr ferritic stainless steels under air and SOFC cathodic conditions [9, 35, 47, 97]. The well-known oxide structure of the bare sample consists of two distinct oxide layers, inner Cr_2O_3 and outer $MnCr_2O_4$. The result of preliminary XRD analysis in Fig. 5.3 shows that Cr_2O_3 and $Mn_xCo_{3-x}O_4$ were present after exposure for 500 h. Further investigation by simultaneous EBSD-EDS analysis revealed that the oxide layer of the coated sample had the similar partitioned geometry to the bare one as observed in Fig. 5.4. Such multi-layered phase variation was suspected as an artifact attributed to a combination of poor resolution of EDS-SEM and overly thin oxide layer. The observation by TEM in Fig. 5.5, however, confirms that the atomic ratios of Cr and Mn in the Co spinel did alter by oxide grains in a bimodal way. The closer the grains in the spinel oxide region were to the Cr_2O_3 layer, the more dominant the Cr was as a constituent of the spinel oxide and vice versa. The normalized line profile in atomic percent across the outer oxide region demonstrates that transitional diffusive zones existed at the Cr_2O_3-Co_3O_4 interface. They were characterized as possessing a higher Cr content than Co content, implying that a nanoscale mixed zone (Cr_2O_3 and Co_3O_4) formed in the vicinity of the Cr_2O_3 layer. At the other extreme was the Mn-enriched Co spinel oxide free of Cr. This is, again, indicative of the retention capability ascribed to Mn, which will be discussed in the subsequent section.

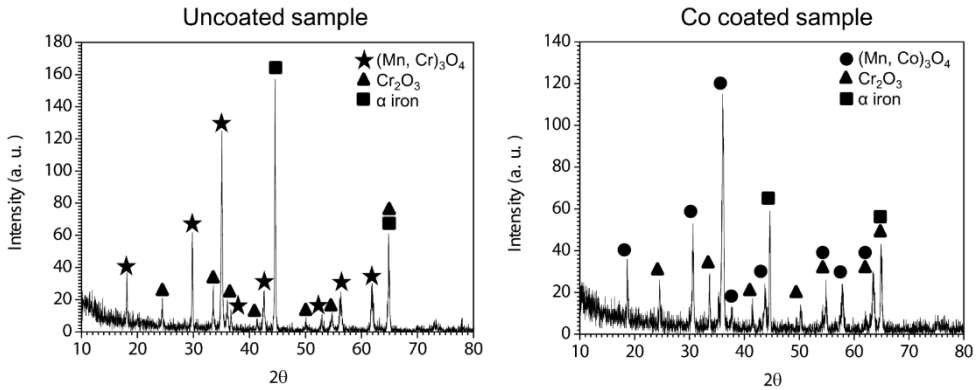

Fig. 5.3. Result of XRD analysis for the uncoated and Co-coated samples oxidized for 500 h.

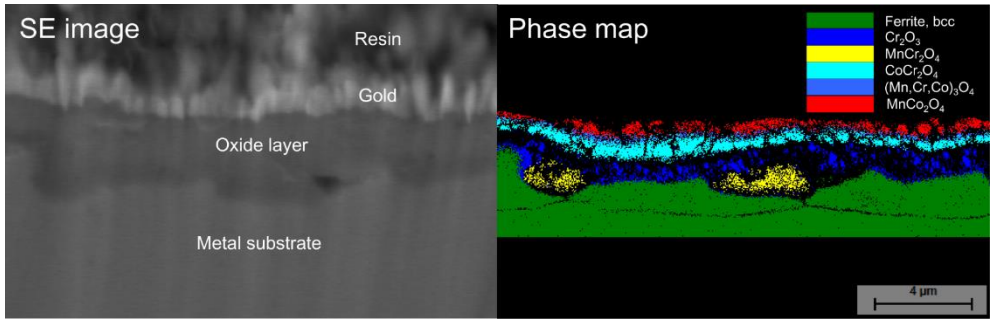

Fig. 5.4. Result of simultaneous EBSD-EDS analysis for the Co-coated sample oxidized for 500 h.

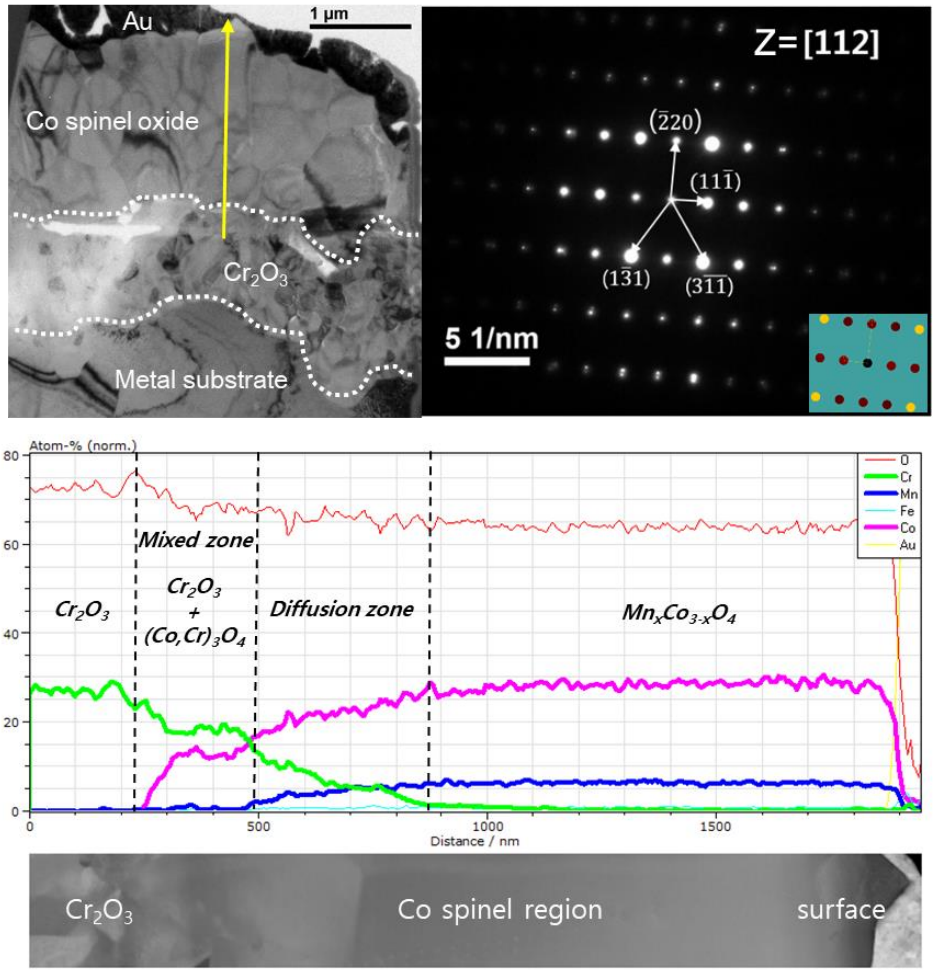

Fig. 5.5. TEM analysis of the Co coated specimen after 500 h of oxidation. The indexed SADP corresponds to the outer Co oxide layer. The arrow marker in the bright field TEM image points to the region of interest for the EDS line profile quantified in normalized at. %.

5.1.3 Sequential crystallographic change of outer Co spinel oxide

Fig. 5.6 shows the result of serial XRD analysis to study the crystallographic evolution of the oxides forming on the coated sample. Oxidation of 1 h transformed the electroplated hexagonal Co into Co_3O_4 (a = 8.084 Å, PDF 00-042-1467). This was confirmed in terms of microstructure and thermodynamics as seen in Fig. 5.7 and Fig. 5.8. However, all the diffraction peaks corresponding to Co_3O_4 were detected at lower diffraction angles than the reference, which indicates the lattice expansion due to element incorporation. In the Co_3O_4 formed at 1 h, the migration of Fe and Mn was, indeed, observed to begin as shown in Fig. 5.7. During the transitional period from 10 to 200 h, the shifting of the diffraction peak A associated with Co_3O_4 to the left side was clearly evident particularly from the (311) diffraction peak. What can be deduced from the observation is that there was a gradual change in the lattice parameter after the first 1 h. Also, the shoulder was detectable on the left side of the peak A of the strongest intensity at the (311) diffraction peak. This shoulder had become gradually pronounced until 300 h and developed to a discrete diffraction peak B that manifested itself at 500 h when no trace of the Co_3O_4 diffraction peaks was found. The newly formed peak was located close to the diffraction angle correspondent to $MnCo_2O_4$ (a = 8.269 Å, PDF 00-023-1237) but slightly shifted to a higher diffraction angle by $2\theta = 0.1458°$.

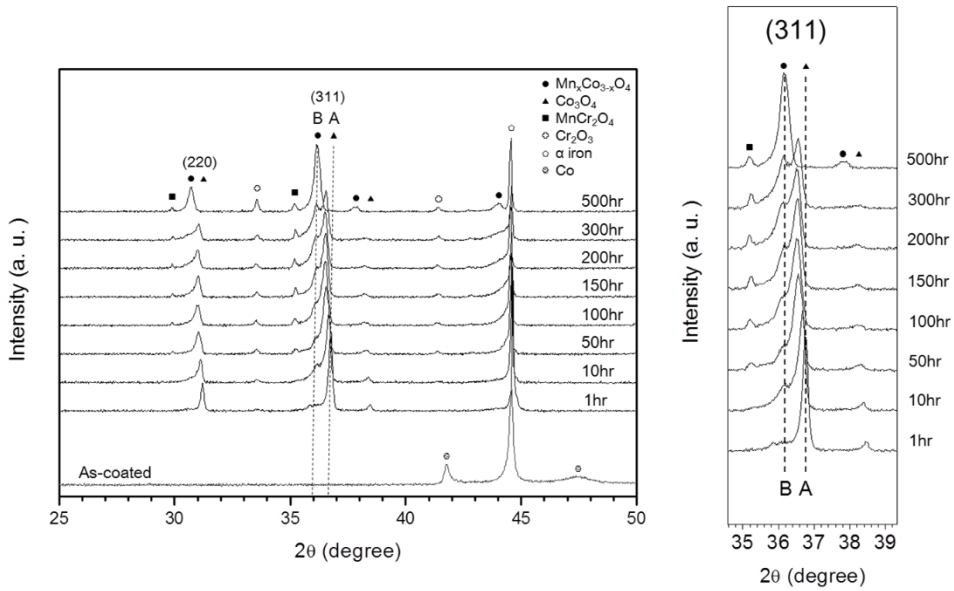

Fig. 5.6. Result of the sequential XRD analysis in the range of 2θ from 25° to 50°. The (311) and (220) peaks of Co_3O_4 are of the first and second strongest intensity. A peak shift and formation of a new peak can be clearly observed in the (311) diffraction peak.

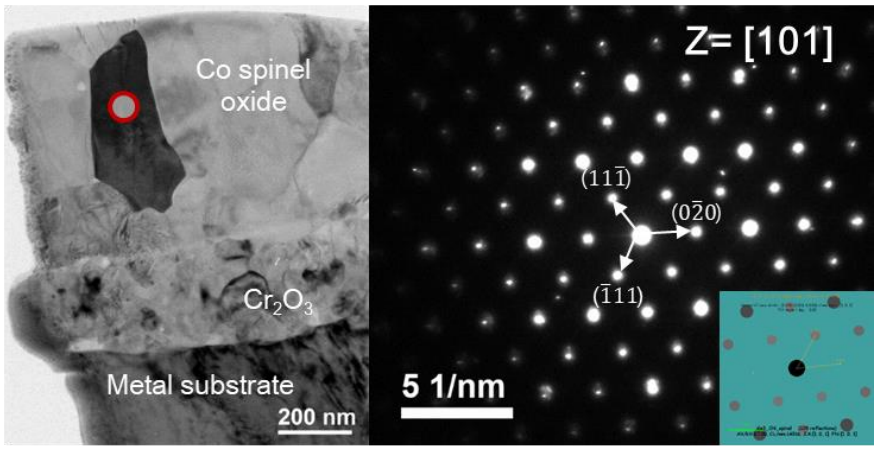

Element	Wt. %	At. %	Uncertainity %
O (K)	30.86	62.09	0.956
Fe (K)	4.84	2.79	0.324
Co (K)	64.29	35.12	1.027
net	99.99	99.98	

Fig. 5.7. Identification of the oxide formed on the sample oxidized for 1 h. Structural and compositional characterization of Co spinel oxide in TEM. The EDS data was obtained from the marked spot in the bright field TEM image.

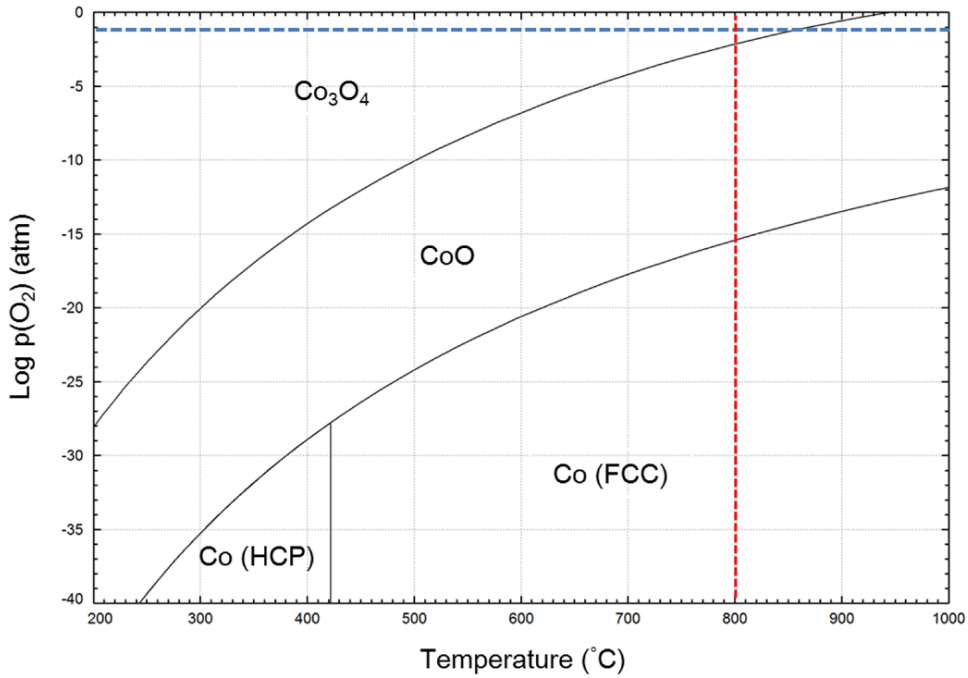

Fig. 5.8. Co-O phase diagram calculated by FactSage using FactPS and FTOxid database. The cross point of the dashed lines indicates the present experimental condition.

5.1.4 Regional phase classification of oxide layers

High speed EDS mapping in TEM was performed for the oxide layers of the coated specimens to examine the compositional change over time. The set of the rendered maps for the 10, 50, 200, and 500 h samples is demonstrated in Fig. 5.9 and the compositional criteria for phase classification are given in Table 5.1. Two significant phenomena were observed in the comparison of the post-processed maps between the transient periods. Mn has predominated as a secondary metallic element ever since 10 h. Especially within the grains of the Co oxide were the regions where Mn was dominating over Cr. Another important observation is that the Co oxide incorporated with both Cr and Mn was localized close to the GBs and at the surface of the Co oxide. These Cr containing regions had gradually diminished and, eventually, disappeared at 500 h. For quantitative comparison, the normalized quantities of the metallic elements were extracted from the three different spots (Spot 1: surface, Spot 2: intra-grain and Spot 3: grain boundary) of the Co oxide layers. The ratios were calculated as below

$$\frac{at.\%\ Metallic\ element}{at.\%\ Co + at.\%\ Cr + at.\%\ Mn + at.\%\ Fe} \qquad (5.1)$$

Fig. 5.10 a), b), and c) exhibit how the ratios of Cr, Mn, and Fe varied over time at different spots: the inside of an oxide grain; superficial area; and GB. The ratios of Mn increased proportionally to time whereas those of Fe reached a maximum at 50 h. Both of them exhibited marginal dependence on the extraction spots. By contrast, the Cr ratio was strongly dependent on the observation spots. The incorporation of Cr was insignificant inside the grains of the Co oxide at all times. The Cr ratios around the GBs were overall greater than that of the oxide intragranular areas. But Cr did not prevail over Mn. On the other hand, the oxide superficial areas were

represented as a highly Cr-incorporated region. This was clearly noticeable in between 10 and 200 h when Cr evaporation was relatively intense.

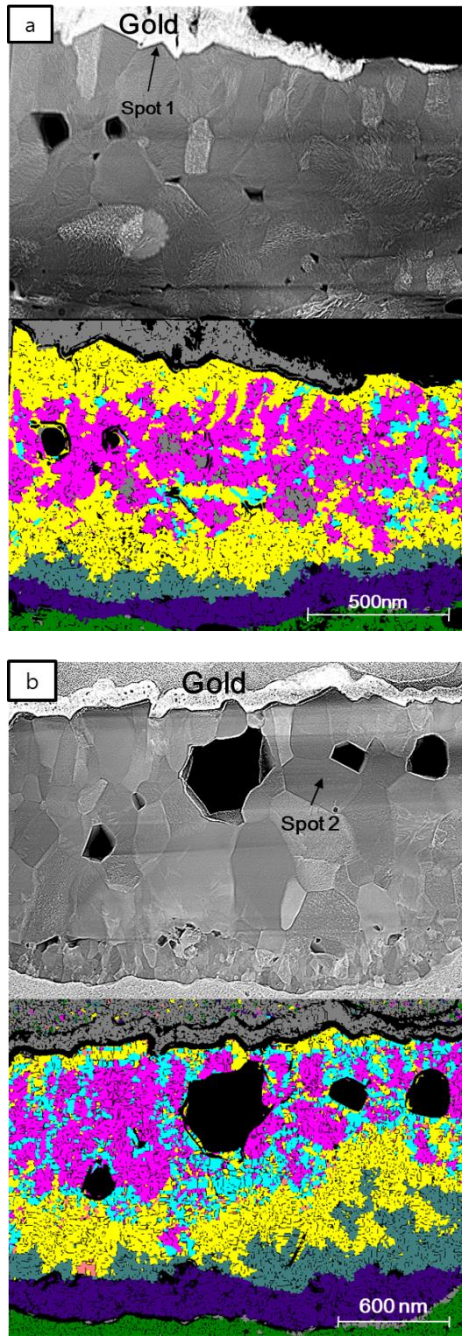
a
Gold
Spot 1
500nm
b
Gold
Spot 2
600 nm

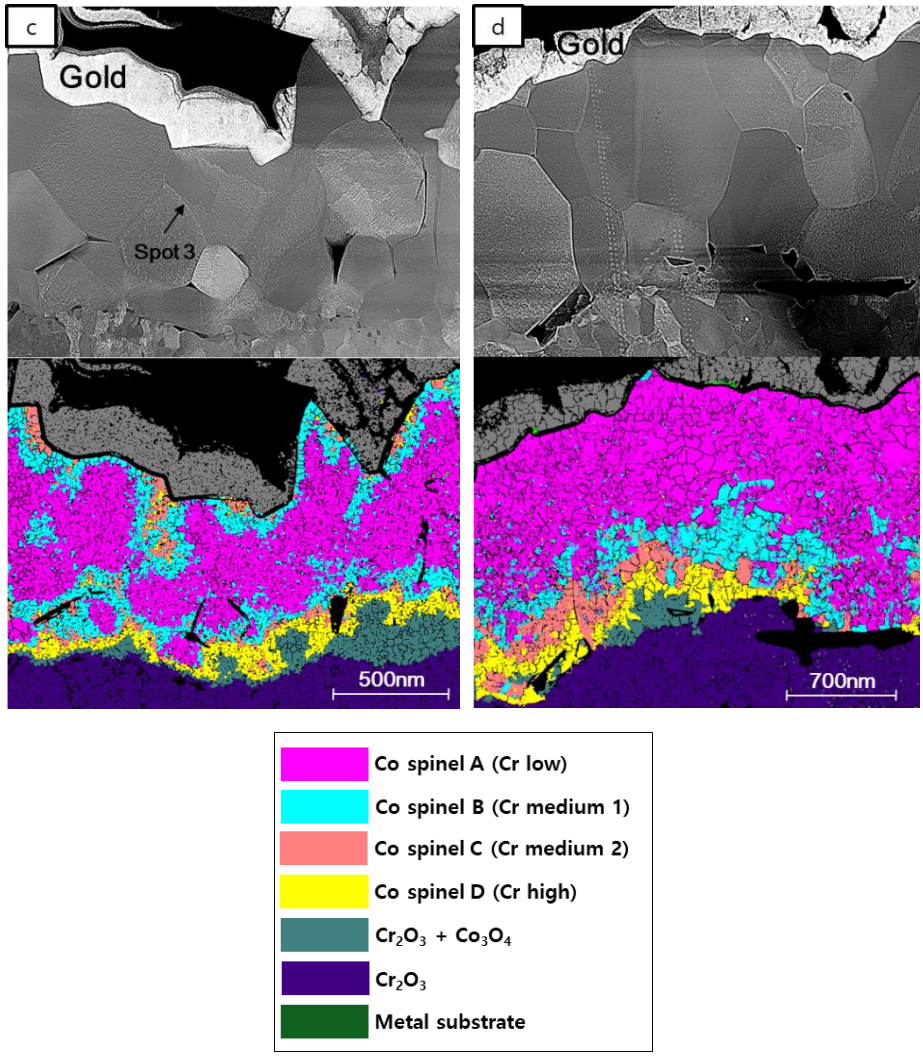

Fig. 5.9. TEM HAADF image and high speed EDS map post-processed by Feature software. a) 10 h, b) 50 h, c) 200 h, and d) 500 h. Refer to Table 5.1 for the compositional classification criteria. Spot 1, 2, and 3 indicate the representative spots used for the quantitative regional EDS analysis, pertaining to an oxide surface, intra-grain and GB, respectively.

Phase	Composition	Note
Co spinel A	$Mn \gg Cr$, $Cr \leq 1$ at. %	Cr low or Mn high
Co spinel B	$Mn > Cr$, $Cr = 1 \sim 3$ at. %	Cr intermediate
Co spinel C	$Mn > Cr$, $Cr \geq 3$ at. %	
Co spinel D	$Mn \leq Cr$	Cr high

Table 5.1. Criteria for the compositional classification of the Co spinel oxide.

a)

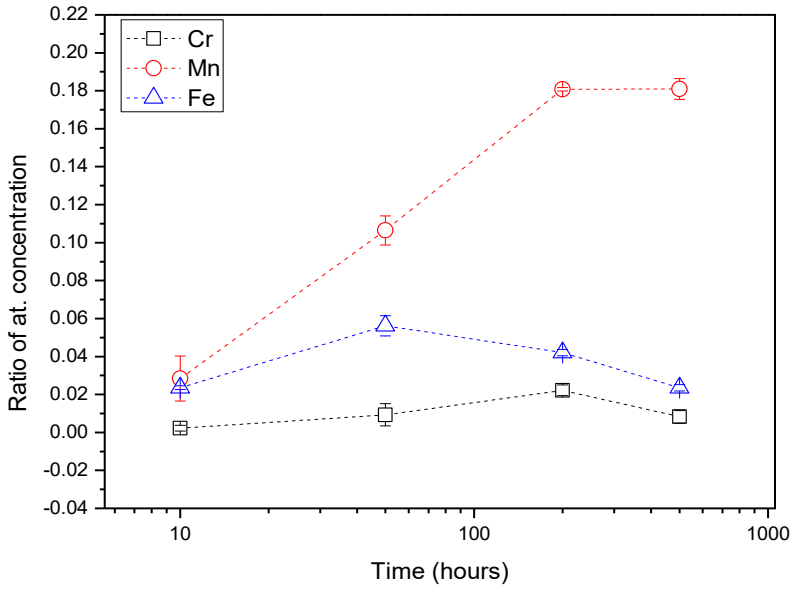
Cr
Mn
Fe
Ratio of at. concentration
0.22
0.20
0.18
0.16
0.14
0.12
0.10
0.08
0.06
0.04
0.02
0.00
-0.02
-0.04
10
100
1000
Time (hours)

b)

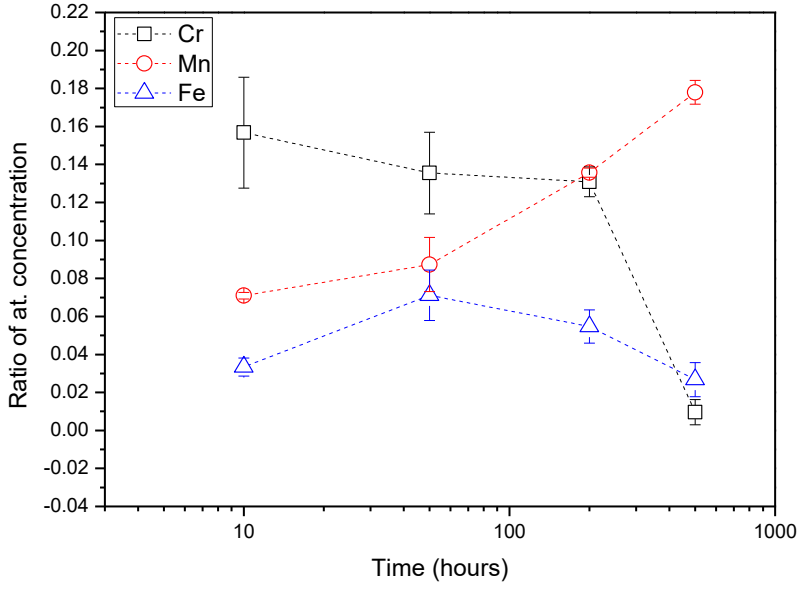
Cr
Mn
Fe
Ratio of at. concentration
0.22
0.20
0.18
0.16
0.14
0.12
0.10
0.08
0.06
0.04
0.02
0.00
-0.02
-0.04
10
100
1000
Time (hours)

c)

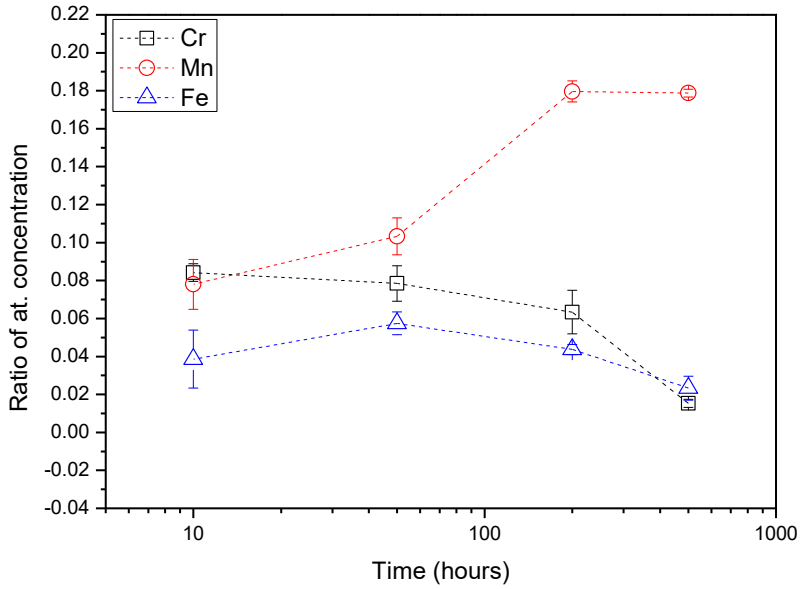

Fig. 5.10. Regional variation of the minor cations comprising the Co spinel oxide: a) Co oxide intra-grain, b) oxide surface and c) GB of oxide.

5.2 Discussion

5.2.1 Evaporation behaviors of volatile Cr and Mn species

Shifting of the diffraction peaks observed in Fig. 5.6 suggests that change in a lattice parameter occurred in the initially formed Co_3O_4. The lattice parameters of the Co spinel oxide were estimated by utilizing the diffraction angles of the (311) diffraction peak and plotted against exposure times as shown in Fig. 5.11. The intra-grain fraction of Co was presented as well to adduce the correlation between minor cation ingress and the lattice parameter change.

It is clearly perceptible from the shift of the peak A that the lattice parameter decreases with the increasing Co ratio until stabilization at 200 h. The minor cationic components migrating to the Co oxide were identified as Fe, Cr, and Mn, the atomic radius of which is greater than that of Co [118]. In general, the lattice parameter of spinel oxide changes in proportion to substitution of a major cation with bigger or smaller minor cations [119]. The lattice expansion of the Co oxide, therefore, mainly results from the gradational migration of the minor cations bigger than Co.

The peak A appears to be associated with the Co spinel oxide mixed with the aforementioned solid-solution cations in that its lattice parameter change is influenced by the time-dependent composition variation. With the increasing Mn content of the Co oxide layer, the Co_3O_4 layer is gradually phase-transformed to $Mn_xCo_{3-x}O_4$ ($x \leq 1$) via solid state reaction. This is manifested by the evolution of the shoulder into the peak B, concurrently exiting with the peak A. Contrary to the peak A, the diffraction angle of the peak B remains unaltered.

The Co-Cr-O phase diagram shows that $Co_{3-x}Cr_xO_4$ has a very large spinel region of homogeneity at 800 °C and $CoCr_2O_4$ becomes the sole equilibrium spinel phase upon reaching a Cr cation fraction of 67 mol. % (See Fig. 5.12). This calculation is

in accord with the experimental result published by Hansson et al. [120]. As shown in Section 5.1.2, the Cr cation fraction of the Co spinel oxide never exceeded 16 % and gradually decreased with increasing oxidation time. Therefore, the occurrence of the peak B is best represented by the phase transformation to Co-Mn spinel oxide (CMO) rather than Co-Cr spinel oxide.

Combinations of TEM and XRD analysis demonstrate, to a first approximation, that the stoichiometric number (x) of Mn falls in a range of 0.6 to 1.0. Known that CMO retains cubic close-packed spinel structure until x reaches 1.0 [121-125], regardless of cooling rates [126], the CMO discovered in this study is determined to have cubic spinel structure. Using the (220), (311), and (222) diffraction peaks, the lattice parameter of the CMO at 500 h was estimated to be 8.230 ± 0.005 Å. Since CMO follows Vegard's law with an increasing Mn content while maintaining cubic spinel structure [121, 127-129], the value for x can be readily obtained by least square linear regression analysis. In addition to Mn, the marginal effect of other pertinent cations on lattice dilation is taken into account, using the following relation expressions [130, 131]

$$\text{Cr - Co}: \ a\ (\pm 0.0002)\ \text{Å} = \ 8.0832 + 0.13205x - 0.00368x^2 \qquad (5.2)$$

$$\text{Fe - Co}: \ a\ (\pm 0.0001)\ \text{Å} = \ 8.086 + 0.166x - 0.08x^2 \qquad (5.3)$$

Finally, in comparison of our experimental value to empirical ones reported by other researchers [127, 128], x is approximated to 0.8, consequently narrowing down the range of x to $0.6 < x < 0.8$.

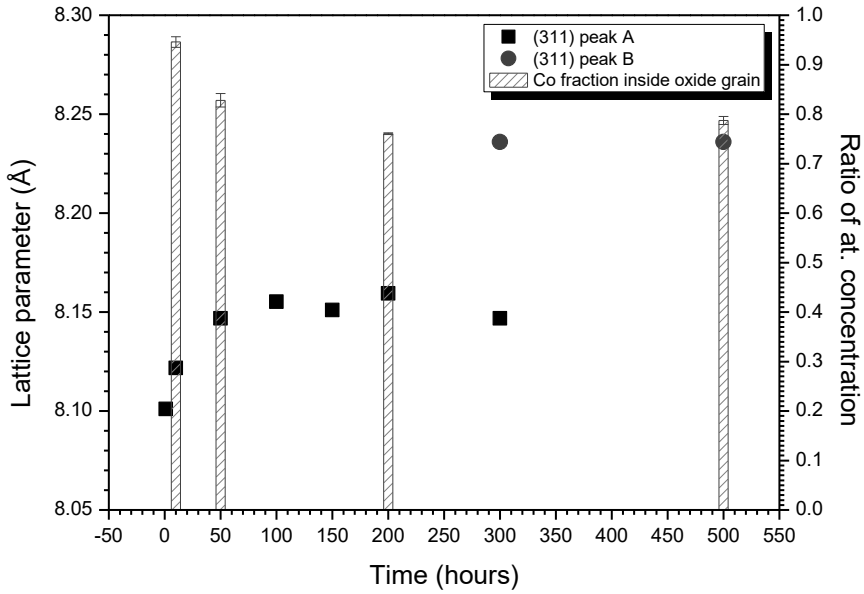

Fig. 5.11. Time-dependent changes in the lattice parameter and Co content of the Co spinel oxide. Only the (311) diffraction peak was used to calculate the lattice parameter. The Co fractions given on the plot represent the compositional ratio of the oxide interior, which is associated with Fig. 5.10 a).

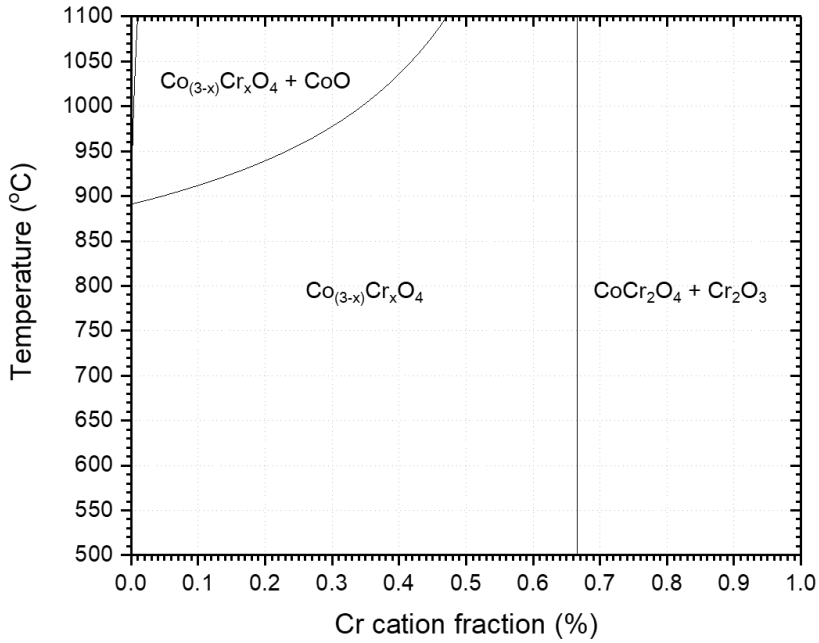

Fig. 5.12. Co-Cr-O phase diagram calculated by FactSage using FactPS and FTOxid database. A level of pO2 was fixed at 0.2 atm.

5.2.2 Fast Mn diffusion in Co oxide

Although the nominal Mn content of the alloy is only 0.441 wt. %, complete oxidation of Co_3O_4 to CMO is shown to be realizable as described in Section 5.1. This section addresses the plausible origins of the phenomenon in light of both thermodynamics and kinetics.

Thermodynamically, strong oxygen affinity of Mn over Cr and Fe is *a priori* the most significant driving force for the outward diffusion of Mn and, hence, outermost formation of CMO. Furthermore, no occurrence of stable Co-dominant $(Co,Cr)_3O_4$ (i.e. $CrCo_2O_4$) intimates that Co spinel oxide is capable of accommodating more Cr as a solid solution than Mn, preserving its crystallographic integrity. The finding from XRD further encourages our notion in that it showed the coexistence of CMO with Co_3O_4 incorporated with solid solution Cr, Fe, or Mn. In the case of Fe, the above speculation is improper because $FeCo_2O_4$ is one of the well-known equilibrium phases. Accordingly, it is presumed that the threshold Fe content cuing the phase transformation could not be attained because of the intermediate Cr_2O_3 layer, a diffusion obstacle for Fe.

The predominance of Mn should partly arise from fast diffusivity of Mn in the crystal structures found in this study. In several former studies, Mn in Cr_2O_3 has been found to diffuse faster than Cr and Fe by one or two orders of magnitude [110, 132, 133]. The tendency is upheld whether polycrystalline Cr_2O_3 is separately made or grown on Ni-Cr alloy, α-, or γ-Fe base alloy. The temperature range used in these references covers the present experimental condition while the oxygen partial pressure ranges from 10^{-4} to 10^{-25} atm. Sabioni et al. claimed that the diffusivity of Cr in Cr_2O_3 was independent from the oxygen partial pressure [134]. Based on the fact that Cr_2O_3 is a p-type metal deficit oxide, it is regarded as legitimate using Ref. [29], [30], and [31] to justify the fast Mn diffusion in Cr_2O_3.

Should information on the self- or impurity diffusivity of Mn and Cr in Co_3O_4 and CMO be available, a solid conclusion based on direct quantitative comparison would likely be drawn. Unfortunately, there are no available diffusivity data. Given the fact that Mn diffuses at a faster rate than Cr and Fe in cubic spinel $MnCr_2O_4$ [111], our best hypothesis is that Mn diffusion would be also prevailing over Cr and Fe diffusion in the spinel Co oxide system.

As a complement to the above hypothesis, the energy-based approach in an atomistic level is contemplated to suggest the theoretical base for the fast Mn diffusion in cubic spinel oxides. Cox et al. proposed the lattice diffusion model to explain partitioning of the oxides formed on Cr-containing Fe base alloy [135]. Their model basically makes two assumptions:

1) The alternating array of octahedral and tetrahedral sites is the most energetically favored diffusion path for metal cations in a spinel oxide, according to Azároff [94] and Sun [96]
2) the activation energy required for diffusion along this path in spinel oxides is largely a summation of strain energy (E_s) and potential energy (E_p), which can be written as

$$D = D_O \, exp\left[-\left(\frac{E_s + E_p}{RT}\right)\right] \tag{5.4}$$

E_s denotes the energy associated with crystal lattice distortion required for each diffusion path and E_p the energy difference between a cation in octahedral and tetrahedral coordination.

For the sake of simplicity, let us imagine the impurity diffusion of only Mn and Cr, two most fluctuating minor cations, through Co_3O_4 crystal lattice, so only E_p is to be sensitive to types of migrating cations. Quantitative evaluation of E_p is enabled by introducing octahedral site preference energy (OSPE) devised for generalized

understanding of cation distribution and degree of inversion occurring in spinel oxides. The cation with high OSPE prefers to occupy an octahedral site; in other words, its displacement necessitates high energy. Despite difference in the methodologies and, hence, the result values, all the former studies by Dunitz and Orgel [136], McClure [137], Miller [138] and Navrotsky and Kleppa [139] have appointed Cr^{3+} as the cation of the strongest OSPE in the first row transition metal group. Readers are referred to Table 5.2 reported by Dunitz and Orger [136] for the snapshot of the OSPE for the cations of interest. Cr^{3+}, on this account, demands the highest E_p for its transfer between octahedral and tetrahedral sites, decelerating the impurity diffusion of Cr through the lattice. Both Mn [140-143] and Cr [144, 145] have been known to exist in trivalent state when incorporated with Co in binary spinel oxide. Therefore, the concept of OSPE remains practical in elucidating the faster transport of Mn than Cr through the spinel Co oxide lattice. This OSPE based approach does not explain the low Fe level in the oxide since OSPE is ascending in the order of Fe^{3+} ~ Mn^{2+}, Fe^{2+}, Mn^{3+}, and Cr^{3+}. It is likely that such disagreement results from the intermediate Cr_2O_3 layer which disrupts Fe ingress from the substrate beforehand.

	A	*B*	*C*	*D*	*E*
Mn^{2+}			0	0	0
Fe^{2+}	10400	10400	11·9	7·9	4·0
Co^{2+}	9700	9700	22·2*	14·8	7·4
Ni^{2+}	8500	8500	29·2	8·6*	20·6
Cu^{2+}	12600	12600	21·6	6·4	15·2
Ti^{3+}	20300	18300	20·9	14·0	6·9
V^{3+}	18600	16700	38·3*	25·5	12·8
Cr^{3+}	17400	15700	53·7	16·0*	37·7
Mn^{3+}	21000	18900	32·4	9·6	22·8
Fe^{3+}			0	0	0

A $\Delta(cm^{-1})$ in hydrates
B $\Delta(cm^{-1})$ in oxides
C Octahedral Stabilization (kcal/mole)
D Tetrahedral Stabilization (kcal/mole)
E Excess Octahedral Stabilization (kcal/mole).

Table 5.2. Crystal field stabilizations for the first-row transition metal oxides [136].

5.2.3 Interpretation of Cr evaporation behavior

According to the first measurements (50 h), the Cr release from the coated sample is primarily suppressed by an order of magnitude in comparison to that of the bare one. It is readily deducible that such physical suppression mainly results from the rapid oxidation of the electroplated metallic Co to Co_3O_4, which drastically suppresses the Cr containing reaction at the surface area exposed to the oxidants. However, such macroscopic interpretation cannot yet provide adequate elucidation for the secondary reduction mechanism for the coated sample particularly between 50 and 200 h.

The overall Cr evaporation process consists of the supply of oxidants, O_2 and H_2O, from the bulk gas, dissociation of water vapor, penetration of O_2 or H_2O through the oxide layer and outward diffusion of Cr from Cr_2O_3 or the substrate. To confirm that the solid-state diffusion process occurring in the oxide layer is the most crucial rate-determining step for Cr evaporation, the mass transfer flux of O_2 and H_2O and dissociation rate of water vapor were computed and compared to the experimental Cr evaporation rate (mass flux). The mass flux of certain gas from the bulk gas mixture to a flat surface through a boundary layer can be calculated as [57, 58]

$$\mathrm{J} = \frac{k_m M_{O_2\ or\ H_2O}}{RT}\left(p^{bulk}_{O_2\ or\ H_2O} - p^{surface}_{O_2\ or\ H_2O}\right) \tag{5.5}$$

where k_m is the mass transfer coefficient of gas, M is the molar mass and p^{bulk} and $p^{surface}$ is the partial pressure of O_2 or H_2O in the bulk gas and at the surface, respectively. Under the present experimental condition, $p^{surface}$ is assumed to be zero. Eq. (5.5) is valid when the Schmidt number (Sc) ranges from 0.6 to 50. The mass transfer coefficient can be expressed as

$$k_m = 0.664\left(\frac{D_{AB}^4}{v_g}\right)^{1/6}\left(\frac{v}{L}\right)^{1/2} \tag{5.6}$$

where D_{AB} is the inter-diffusion coefficient of O_2 or H_2O in air, v_g is the kinematic viscosity, v is the gas velocity, and L is the sample length in the gas flow direction. The calculation of D_{AB} and v_g is facilitated by the Chapman-Enskog equation [146]. The Lennard-Jones parameters and collision integrals required for the calculation is obtainable from other literatures [146, 147]. The dissociation rate of H_2O is in the first order relation with p_{H_2O}, given by [148, 149]

$$J_{H_2O}^{Dissociation} = k\left(p_{H_2O}^{bulk} - p_{H_2O}^{eqiilibrium}\right) \tag{5.7}$$

where k is the dissociation rate constant and $p^{equilibrium}$ is the equilibrium partial pressure of H_2O for the dissociation reaction, which is assumed to be zero. According to Nagasaki and Fruehen, the following is the dissociation rate constant of H_2O over pure liquid Fe as a function of temperature [148]

$$\log k = -\frac{4860}{T} + 0.57 \quad (mol \cdot cm^{-2} \cdot sec^{-1} \cdot atm^{-1}) \tag{5.8}$$

The result of the calculation is tabulated in Table 5.3. The Sc of O_2 and H_2O in the present experimental setting meets the aforementioned criterion, indicating the reliability of Eq. (5.5). The calculated mass transfer fluxes of the oxidants from the bulk gas are, at least, one order of magnitude greater than the maximum $J_{Cr\ species}$ of the coated sample. The dissociation of H_2O is also much faster than $J_{Cr\ species}$. Based on the calculation with regard to the gas-phase mass transfer of the oxidants, it is conceivable that the oxidants are sufficiently supplemented onto the oxide

surface and that solid-state diffusion of either the oxidants or Cr through the oxide layer is most likely to be rate-determining for the overall Cr evaporation process. Because the information on the diffusivities of the oxidants and Cr in the Co oxide system has not been properly reported, precise quantitative comparison is unavailable. Nonetheless, note that it is now compelling to rule out the influence of the gas-phase mass transfer on the Cr evaporation kinetics under the present experimental condition.

When the rate-determining step of Cr evaporation is transport of volatile Cr species in the boundary layer over an flat oxide plate, a Cr evaporation rate is proportional to a partial pressure of gaseous Cr species as follows [150]

$$k_{evaporation} \propto \left(\frac{v^{0.5}}{P^{0.5}}\right) p_{H_2O}\, p_{O_2}\, exp\left(-\frac{\Delta G}{RT}\right) = \left(\frac{v^{0.5}}{P^{0.5}}\right) p_{Cr\ species} \qquad (5.9)$$

where v is linear gas velocity, P is total pressure, and $p_{Cr\ species}$ is the partial pressure of gaseous Cr species. The exponents of v and P can be corrected to 0.8 and 0.2, respectively, for turbulent flow conditions when the Reynolds number is greater than 3×10^5. This relationship enables one to compare the evaporation rates of Cr species over different types of Cr-dominant oxide layers as far as their thermodynamic data is given. Holcomb and Alma [151] and Stanislowski et al. [36] well exemplified the thermodynamic approach to account for a time-dependent reduction in the Cr evaporation rate of the bare sample where formation of two different Cr-dominant oxides, Cr_2O_3 and $MnCr_2O_4$, is evident. In contrast, such interpretation is not suited to understanding the phenomena of the coated sample where the vigorous transport of the minor cations destabilizes the chemical composition of the Co oxide during the period of our interest.

On the basis of the overall observation by TEM, we attempted to come up with the correlation between Cr evaporation from the coated sample and time-dependent compositional change of the oxide. At first, it was speculated that types of outermost oxides and its composition would most substantially govern the Cr evaporation behavior. However, such interrelationship turns out to be inadequate for the coated sample because the Co oxide was not only incompletely transformed into CMO but also superficially incorporated with Cr even at the stabilization period (200 h). That is, there must be a more fundamental factor which contributes to the secondary reduction in the Cr release from the coated sample.

The surface of the Co oxide is to be envisaged as the most intense reaction site for Cr evaporation. Indeed, the Cr incorporation around the surface area is remarkably pronounced as seen in Fig. 5.9 a). The Co spinel D (Cr > Mn) had taken up a large fraction of the Co oxide, particularly the surface, at 10 h and, afterward, turned into the Co spinel B and C (Mn > Cr, intermediate Cr content) with increasing time, accompanied by reduction in Cr release. It is highly believed that the formation of the continuous Cr containing oxide layer results from fast Cr transport *via* surface diffusion [59, 152]. Subsequent lattice out-diffusion of Cr from both adjacent GBs and surfaces allows the diffusion fringes to overlap, producing the continuous Cr containing oxide layer. The configuration of the Cr incorporated areas (lattice diffusion fringes) at the surfaces changes from Harrison classification type A to type B [106, 153]. This is mainly owing to oxide grain growth which makes the spacing between the diffusion origins greater than the diffusion length ($\sqrt{D_{Cr}^{lattice}t}$). It should be also noted that the time-dependent decrease of the surface and GB Cr content signifies the Cr flux ($J_{Cr}^{lattice}$) from those two regions being reduced along with a diminished Cr concentration gradient, contributing to the transition to Type B. For a

comprehensive grasp of the overall phenomena described above, the reader is referred to the schematic diagram presented in Fig. 5.13.

Qualitative observations by TEM in Fig. 5.9 illustrate that GBs of the Co oxide are the preferential outward diffusion path for Cr during the period from 10 to 200 h. This is manifested by the Cr and Mn content in the Co oxide lattice, especially, at 10 h; the relatively low Cr and high Mn content indicate that the interference of Mn in the lattice transport of Cr commences even in the early phase of the present experiment. According to the Co-O phase diagram in Fig. 5.8 and other literature [154], the dissociation oxygen partial pressure of Co_3O_4 at 800 °C is on the order of 10^{-3} atm. No Co monoxide being detected, the oxygen partial pressure through the Co oxide layer must be sustained high enough to provoke Cr evaporation. This assumption is further supported by Horita et al. who observed the fast oxygen penetration through $MnCo_2O_4$ [155]. It is, therefore, reasonable to state that the GB regions act as reaction sites to which the initial Cr evaporation behavior is partly attributed. These reaction sites, however, are compromised as the GB diffusion of Cr is drastically suppressed upon the stabilization of CMO. Simultaneously, the Cr supply from the Cr reservoir to the surface also ceases while the Cr depletion by evaporation continues on. It is asserted from those observations that the most obvious cause for the secondary suppression is formation of the enhanced Cr diffusion barrier, CMO, interrupting the GB Cr supply, the rate-determining step for the evaporation process.

$Max.J_{Cr\ species}$ (10^{-11})	J_{O_2} (10^{-8})	J_{H_2O} (10^{-10})	$J_{H_2O}^{Diss.}$ (10^{-4})	Sc
Uncoated: 31.97 Coated: 5.541	1.080	6.297	3.595	O_2: 0.765 H_2O: 0.882

Table 5.3. Result of the mass transfer calculation for the Cr evaporation process. The flux is in a unit of $kg \cdot m^{-2} \cdot sec^{-1}$.

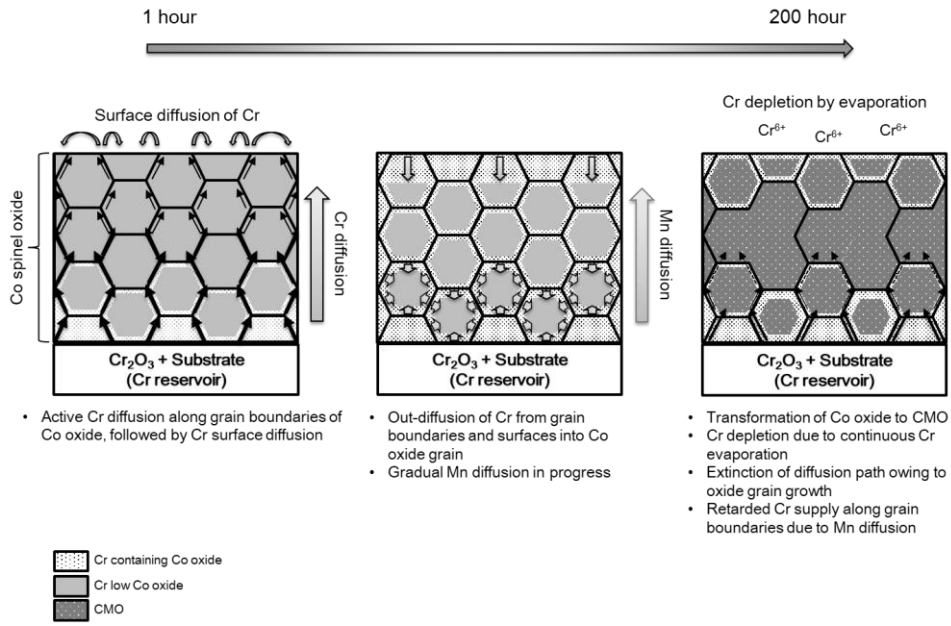

Fig. 5.13. Schematic diagram which illustrates the overall transport phenomena occurring in the Co spinel oxide during the transient period.

Chapter 6.

Summary and Conclusion

6.1 Effect of alloy grain size on oxidation behavior

Two specimens of Crofer22 APU with different grain size were oxidized at 800 ºC in humid air (2% H_2O) in order to study the effect of alloy GBs on oxidation behavior. The EBSD analysis revealed that the grain size of two specimens differed by a factor of 25. The specimen with larger grain size exhibited improved oxidation resistance (i.e. a reduction of 30% in k_w). The microstructure of the oxidized specimens was investigated employing SEM, EBSD, TKD and TEM to discover the primary cause of the improved oxidation resistance. In addition to the microstructure analysis, the pO_2 map pertaining to the observed oxide scales was drawn by virtue of thermodynamic calculation. The key findings are summarized below.

1. Both specimens formed the duplex oxide layer which consists of Cr_2O_3 overlaid by $MnCr_2O_4$. The preferential internal oxidation occurred along the GB of the alloy (i.e. intergranular oxidation). The intergranular oxide scale was characterized as $MnCr_2O_4$ compositionally and structurally comparable to the surface one.
2. The surface scale ridge was observed to emerge from the alloy GB characterized as a high angle random GB (< 15º). The formation of such ridge appears to result from volumetric compensation for intergranular $MnCr_2O_4$ as well as, to some extent, fast metal supply from the alloy GB.
3. The pO_2 across the oxide layer was speculated to range from 0.2 atm (top) to 10^{-28} atm (Cr_2O_3-alloy interface). The presence of the Ti oxide particles

dispersed in the alloy matrix below Cr_2O_3 implies that the pO_2 in the alloy matrix is maintained below 10^{-28} atm.

4. The thickness of the intragranular oxide layers differed by only 3%, equivalent to a difference of 5% in k_w. Furthermore, the difference in the grain size of outer $MnCr_2O_4$ was measured merely 7%. These findings clarify intergranular oxidation being the most dominant factor contributing to the different oxidation behavior in the present study.

In terms of practical SOFC application, surface roughening by ridge formation imposes a potential hazard on the structural integrity of an oxide layer. The scale ridge may become an area where local stress concentration occurs and, thus, a crack or spallation originates, especially, during repetitive cycles of cooling and heating. In conclusion, it is highly believed that increasing the grain size of Crofer22 APU is beneficial to not only improving oxidation resistance but retaining structural stability.

6.2 Suppression of Cr evaporation by Co electroplating

The Cr evaporation behavior of the high Cr containing ferritic stainless steel with and without Co electroplating was investigated by the transpiration method. A tenfold reduction in the accumulative Cr release amount was achieved by surface modification using Co DC pulse electroplating. The plot of the Cr evaporation rate to time indicated that the primary reduction occurred during the first measurement period (50 h), followed by gradual secondary reduction until 200 h. Simple oxide characterization showed that the primary reduction arose from the oxidation of the Co layer to Co spinel oxide, acting as an effective diffusion barrier hindering the direct exposure of the Cr evaporation sources (Cr_2O_3 or alloy) to the oxidants.

To understand the underlying mechanism of the secondary reduction, both microstructural and compositional evolution of the oxide layer on the coated sample were thoroughly observed by sequential XRD and TEM analysis. At the very beginning of the oxidation, the deposited Co layer was oxidized to Co_3O_4; simultaneously, the migration of Fe, Cr, and Mn commenced, leading to the gradual lattice expansion of Co_3O_4. The incorporation of Mn was observed to be most predominant among the three minor cations. This facilitated the phase transformation of Co_3O_4 to $Mn_xCo_{3-x}O_4$ ($0.6 < x < 0.8$). The compositional analysis demonstrated the presence of Cr diffusion fringes adjacent to the GBs of the Co spinel oxide, which indicates that GB diffusion is a dominant transport mechanism for Cr in the Co spinel oxide. The Cr diffusion fringes disappeared as the phase transformation of the Co spinel oxide progressed with increasing Mn content. Considering that Cr supply was a rate-determining step for overall Cr evaporation process under our experimental conditions, the suspension of Cr transport due to the phase transformation was concluded to play a decisive role for the secondary reduction.

Chapter 7.

References

[1] S.C. Singhal, Science and technology of solid-oxide fuel cells, MRS bulletin 25(03) (2000) 16-21.

[2] W.Z. Zhu, S.C. Deevi, Development of interconnect materials for solid oxide fuel cells, Mater. Sci. Eng. A 348(1–2) (2003) 227-243.

[3] Z. Yang, Recent advances in metallic interconnects for solid oxide fuel cells, International Materials Reviews 53(1) (2008) 39-54.

[4] S. de Souza, S.J. Visco, L.C. De Jonghe, Thin-film solid oxide fuel cell with high performance at low-temperature, Solid State Ion. 98(1–2) (1997) 57-61.

[5] S.C. Singhal, Solid oxide fuel cells for stationary, mobile, and military applications, Solid State Ion. 152–153(0) (2002) 405-410.

[6] K. Huang, R.S. Tichy, J.B. Goodenough, Superior Perovskite Oxide-Ion Conductor; Strontium- and Magnesium-Doped $LaGaO_3$: I, Phase Relationships and Electrical Properties, J. Am. Ceram. Soc 81(10) (1998) 2565-2575.

[7] T. Ishihara, H. Matsuda, Y. Takita, Doped $LaGaO_3$ Perovskite Type Oxide as a New Oxide Ionic Conductor, J. Am. Chem. Soc 116(9) (1994) 3801-3803.

[8] W.J. Quadakkers, J. Piron-Abellan, V. Shemet, L. Singheiser, Metallic interconnectors for solid oxide fuel cells - a review, Mater. High Temp. 20(2) (2003) 115-127.

[9] J.W. Fergus, Metallic interconnects for solid oxide fuel cells, Mater. Sci. Eng. A 397(1–2) (2005) 271-283.

[10] Z. Yang, K.S. Weil, D.M. Paxton, J.W. Stevenson, Selection and Evaluation of Heat-Resistant Alloys for SOFC Interconnect Applications, J. Electrochem. Soc. 150(9) (2003) A1188-A1201.

[11] W. Huang, S. Gopalan, U.B. Pal, S.N. Basu, Evaluation of Electrophoretically

Deposited $CuMn_{1.8}O_4$ Spinel Coatings on Crofer 22 APU for Solid Oxide Fuel Cell Interconnects, J. Electrochem. Soc. 155(11) (2008) B1161-B1167.

[12] W.N. Liu, X. Sun, E. Stephens, M.A. Khaleel, Life prediction of coated and uncoated metallic interconnect for solid oxide fuel cell applications, J. Power Sources 189(2) (2009) 1044-1050.

[13] I. Kaur, Y. Mishin, W. Gust, Fundamentals of grain and interphase boundary diffusion, John Wiley & Sons, Chichester, New York, 1995.

[14] J.H. Kim, D.-I. Kim, S. Suwas, E. Fleury, K.-W. Yi, Grain-Size Effects on the High-Temperature Oxidation of Modified 304 Austenitic Stainless Steel, Oxid. Met. (2012) 1-9.

[15] G.J. Yurek, D. Eisen, A. Garratt-Reed, Oxidation behavior of a fine-grained rapidly solidified 18-8 stainless steel, Metall. Trans. A 13(3) (1982) 473-485.

[16] S.N. Basu, G.J. Yurek, Effect of alloy grain size and silicon content on the oxidation of austenitic Fe-Cr-Ni-Mn-Si alloys in pure O2, Oxid. Met. 36(3-4) (1991) 281-315.

[17] R.K. Singh Raman, A.S. Khanna, R.K. Tiwari, J.B. Gnanamoorthy, Influence of grain size on the oxidation resistance of 2 4 1 Cr-1Mo steel, Oxid. Met. 37(1) (1992) 1-12.

[18] V. Trindade, H.-J. Christ, U. Krupp, Grain-Size Effects on the High-Temperature Oxidation Behaviour of Chromium Steels, Oxid. Met. 73(5) (2010) 551-563.

[19] P. Pérez, Influence of the alloy grain size on the oxidation behaviour of PM2000 alloy, Corros. Sci. 44(8) (2002) 1793-1808.

[20] Y. Lin, D.E. Laughlin, J. Zhu, A study of the determination of grain boundary diffusivity and energy through the thermally grown oxide ridges on a Fe-22Cr alloy surface, Philos. Mag. 97(8) (2017) 535-548.

[21] M.P. Phaniraj, D.-I. Kim, Y.W. Cho, Effect of grain boundary characteristics on the oxidation behavior of ferritic stainless steel, Corros. Sci. 53(12) (2011) 4124-4130.

[22] J. Zhu, L.M.F. Diaz, G.R. Holcomb, P.D. Jablonski, C.J. Cowen, D.E. Laughlin, D. Alman, S. Sridhar, On the Relation Between Oxide Ridge Evolution and Alloy Surface Grain Boundary Disorientation in Fe–22 wt % Cr Alloys, J. Electrochem. Soc. 157(5) (2010) B655-B664.

[23] N.J. Magdefrau, L. Chen, E.Y. Sun, M. Aindow, Effects of alloy heat treatment on oxidation kinetics and scale morphology for Crofer 22 APU, J. Power Sources 241 (2013) 756-767.

[24] J. Froitzheim, G.H. Meier, L. Niewolak, P.J. Ennis, H. Hattendorf, L. Singheiser, W.J. Quadakkers, Development of high strength ferritic steel for interconnect application in SOFCs, J. Power Sources 178(1) (2008) 163-173.

[25] Z. Żurek, A. Jaroń, M. Homa, Morphology Analysis of the Scale Formed on Crofer 22APU Steel in Atmospheres Containing SO2, Oxid. Met. 76(3) (2011) 273-285.

[26] N. Shaigan, W. Qu, D.G. Ivey, W. Chen, A review of recent progress in coatings, surface modifications and alloy developments for solid oxide fuel cell ferritic stainless steel interconnects, J. Power Sources 195(6) (2010) 1529-1542.

[27] C. Gindorf, L. Singheiser, K. Hilpert, Vaporisation of chromia in humid air, J. Phys. Chem. Solids 66(2–4) (2005) 384-387.

[28] E. Opila, N. Jacobson, D. Myers, E. Copland, Predicting oxide stability in high-temperature water vapor, JOM-J. Min. Met. Mat. S. 58(1) (2006) 22-28.

[29] S. Taniguchi, M. Kadowaki, H. Kawamura, T. Yasuo, Y. Akiyama, Y. Miyake, T. Saitoh, Degradation phenomena in the cathode of a solid oxide fuel cell with an alloy separator, J. Power Sources 55(1) (1995) 73-79.

[30] S.P. Jiang, J.P. Zhang, X.G. Zheng, A comparative investigation of chromium deposition at air electrodes of solid oxide fuel cells, J. Eur. Ceram. Soc. 22(3) (2002) 361-373.

[31] S.P.S. Badwal, R. Deller, K. Foger, Y. Ramprakash, J.P. Zhang, Interaction between chromia forming alloy interconnects and air electrode of solid oxide fuel cells, Solid State Ion. 99(3–4) (1997) 297-310.

[32] S.P. Simner, M.D. Anderson, G.-G. Xia, Z. Yang, L.R. Pederson, J.W. Stevenson,

SOFC Performance with Fe-Cr-Mn Alloy Interconnect, J. Electrochem. Soc. 152(4) (2005) A740-A745.

[33] K. Hilpert, D. Das, M. Miller, D.H. Peck, R. Weiß, Chromium Vapor Species over Solid Oxide Fuel Cell Interconnect Materials and Their Potential for Degradation Processes, J. Electrochem. Soc. 143(11) (1996) 3642-3647.

[34] Z. Yang, J.W. Stevenson, K.D. Meinhardt, Chemical interactions of barium–calcium–aluminosilicate-based sealing glasses with oxidation resistant alloys, Solid State Ion. 160(3–4) (2003) 213-225.

[35] M. Stanislowski, E. Wessel, K. Hilpert, T. Markus, L. Singheiser, Chromium Vaporization from High-Temperature Alloys: I. Chromia-Forming Steels and the Influence of Outer Oxide Layers, J. Electrochem. Soc. 154(4) (2007) A295-A306.

[36] M. Stanislowski, J. Froitzheim, L. Niewolak, W.J. Quadakkers, K. Hilpert, T. Markus, L. Singheiser, Reduction of chromium vaporization from SOFC interconnectors by highly effective coatings, J. Power Sources 164(2) (2007) 578-589.

[37] A.N. Hansson, S. Linderoth, M. Mogensen, M.A.J. Somers, Inter-diffusion between Co_3O_4 coatings and the oxide scale on Fe-22Cr, J. Alloy. Compd. 433(1–2) (2007) 193-201.

[38] H. Ebrahimifar, M. Zandrahimi, Oxidation and Electrical Behavior of Mn-Co-Coated Crofer 22 APU Steel Produced by a Pack Cementation Method for SOFC Interconnect Applications, Oxid. Met. 84(1) (2015) 129-149.

[39] H. Ebrahimifar, M. Zandrahimi, Oxidation and Electrical Behavior of a Ferritic Stainless Steel with a Mn–Co-Based Coating for SOFC Interconnect Applications, Oxid. Met. 84(3) (2015) 329-344.

[40] H. Ebrahimifar, M. Zandrahimi, Evaluation of the Parabolic Rate Constant During Different Types of Oxidation Tests for Spinel Coated Fe–17%Cr Alloy, Oxid. Met. 75(3-4) (2011) 125-141.

[41] A.M. Dayaghi, M. Askari, P. Gannon, Pre-treatment and oxidation behavior of sol–gel Co coating on 430 steel in 750°C air with thermal cycling, Surf. Coat. Technol. 206(16) (2012) 3495-3500.

[42] A. Petric, H. Ling, Electrical Conductivity and Thermal Expansion of Spinels at Elevated Temperatures, J. Am. Ceram. Soc 90(5) (2007) 1515-1520.

[43] C. Collins, J. Lucas, T.L. Buchanan, M. Kopczyk, A. Kayani, P.E. Gannon, M.C. Deibert, R.J. Smith, D.S. Choi, V.I. Gorokhovsky, Chromium volatility of coated and uncoated steel interconnects for SOFCs, Surf. Coat. Technol. 201(7) (2006) 4467-4470.

[44] J. Froitzheim, S. Canovic, M. Nikumaa, R. Sachitanand, L.G. Johansson, J.E. Svensson, Long term study of Cr evaporation and high temperature corrosion behaviour of Co coated ferritic steel for solid oxide fuel cell interconnects, J. Power Sources 220 (2012) 217-227.

[45] V.I. Gorokhovsky, P.E. Gannon, M.C. Deibert, R.J. Smith, A. Kayani, M. Kopczyk, D. VanVorous, Z. Yang, J.W. Stevenson, S. Visco, C. Jacobson, H. Kurokawa, S.W. Sofie, Deposition and Evaluation of Protective PVD Coatings on Ferritic Stainless Steel SOFC Interconnects, J. Electrochem. Soc. 153(10) (2006) A1886-A1893.

[46] H. Kurokawa, C.P. Jacobson, L.C. DeJonghe, S.J. Visco, Chromium vaporization of bare and of coated iron–chromium alloys at 1073 K, Solid State Ion. 178(3–4) (2007) 287-296.

[47] T. Uehara, N. Yasuda, M. Okamoto, Y. Baba, Effect of Mn–Co spinel coating for Fe–Cr ferritic alloys ZMG232L and 232J3 for solid oxide fuel cell interconnects on oxidation behavior and Cr-evaporation, J. Power Sources 196(17) (2011) 7251-7256.

[48] Z. Yang, G. Xia, J.W. Stevenson, $Mn_{1.5}Co_{1.5}O_4$ Spinel Protection Layers on Ferritic Stainless Steels for SOFC Interconnect Applications, Electrochem. Solid State Lett. 8(3) (2005) A168-A170.

[49] Q. Fu, F. Tietz, D. Sebold, E. Wessel, H.-P. Buchkremer, Magnetron-sputtered cobalt-based protective coatings on ferritic steels for solid oxide fuel cell interconnect applications, Corros. Sci. 54(0) (2012) 68-76.

[50] N.V. Gavrilov, V.V. Ivanov, A.S. Kamenetskikh, A.V. Nikonov, Investigations of Mn–Co–O and Mn–Co–Y–O coatings deposited by the magnetron sputtering on ferritic stainless steels, Surf. Coat. Technol. 206(6) (2011) 1252-1258.

[51] S.J. Han, Z. Pala, S. Sampath, Plasma sprayed manganese–cobalt spinel coatings: Process sensitivity on phase, electrical and protective performance, J. Power Sources 304 (2016) 234-243.

[52] J. Wu, C.D. Johnson, R.S. Gemmen, X. Liu, The performance of solid oxide fuel cells with Mn–Co electroplated interconnect as cathode current collector, J. Power Sources 189(2) (2009) 1106-1113.

[53] J. Wu, C.D. Johnson, Y. Jiang, R.S. Gemmen, X. Liu, Pulse plating of Mn–Co alloys for SOFC interconnect applications, Electrochim. Acta 54(2) (2008) 793-800.

[54] J. Wu, Y. Jiang, C. Johnson, X. Liu, DC electrodeposition of Mn–Co alloys on stainless steels for SOFC interconnect application, J. Power Sources 177(2) (2008) 376-385.

[55] X. Yang, H. Tu, Q. Yu, Fabrication of Co_3O_4 and $La_{0.6}Sr_{0.4}CoO_{3-\delta}$–$Ce_{0.8}Gd_{0.2}O_{2-\delta}$ dual layer coatings on SUS430 steel by in-situ phase formation for solid oxide fuel cell interconnects, Int. J. Hydrogen Energ. 40(1) (2015) 607-614.

[56] Q.X. Fu, D. Sebold, F. Tietz, H.P. Buchkremer, Electrodeposited cobalt coating on Crofer22APU steels for interconnect applications in solid oxide fuel cells, Solid State Ion. 192(1) (2011) 376-382.

[57] D.J. Young, High temperature oxidation and corrosion of metals, Elsevier2008.

[58] N. Birks, G.H. Meier, F.S. Pettit, Introduction to the high temperature oxidation of metals, Cambridge University Press2006.

[59] P. Kofstad, High temperature oxidation of metals, Wiley1966.

[60] R.E. Bedworth, N.B. Pilling, The oxidation of metals at high temperatures, J. Inst. Met. 29(3) (1923) 529-582.

[61] K. Hauffe, H. Pfeiffer, Über die Mitwirkung von Phasengrenzreaktionen bei der Oxydation von Metallen und Legierungen bei höheren Temperaturen, Zeitschrift für Elektrochemie, Berichte der Bunsengesellschaft für physikalische Chemie 56(4) (1952) 390-398.

[62] F. Pettit, R. Yinger, J.B. Wagner, The mechanism of oxidation of iron in carbon monoxide-carbon dioxide mixtures, Acta Metall. 8(9) (1960) 617-623.

[63] C. Wagner, Oxidation of Alloys Involving Noble Metals, J. Electrochem. Soc. 103(10) (1956) 571-580.

[64] N.G. Eror, J.B. Wagner, Electrical conductivity and thermogravimetric studies of single crystalline cobaltous oxide, J. Phys. Chem. Solids 29(9) (1968) 1597-1611.

[65] B. Fisher, D.S. Tannhauser, Electrical Properties of Cobalt Monoxide, J. Chem. Phys. 44(4) (1966) 1663-1672.

[66] R. Dieckmann, Point defects and transport properties of binary and ternary oxides, Solid State Ion. 12 (1984) 1-22.

[67] B.B. Ebbinghaus, Thermodynamics of gas phase chromium species: The chromium oxides, the chromium oxyhydroxides, and volatility calculations in waste incineration processes, Combust. Flame 93(1–2) (1993) 119-137.

[68] C. Gindorf, L. Singheiser, K. Hilpert, Chromium vaporisation from Fe,Cr base alloys used as interconnect in fuel cells, Steel Research 72(11-12) (2001) 528-533.

[69] D. Caplan, M. Cohen, The Volatilization of Chromium Oxide, J. Electrochem. Soc. 108(5) (1961) 438-442.

[70] Y.W. Kim, G.R. Belton, The thermodynamics of volatilization of chromic oxide: Part I. the species CrO3 and CrO2 OH, Metallurgical Transactions 5(8) (1974) 1811-1816.

[71] E.J. Opila, D.L. Myers, N.S. Jacobson, I.M.B. Nielsen, D.F. Johnson, J.K. Olminsky, M.D. Allendorf, Theoretical and Experimental Investigation of the Thermochemistry of $CrO_2(OH)_2(g)$, The Journal of Physical Chemistry A 111(10) (2007) 1971-1980.

[72] G. Holcomb, D. Alman, Effect of manganese addition on reactive evaporation of chromium in Ni-Cr alloys, J. Mater. Eng. Perform. 15(4) (2006) 394-398.

[73] J.W. Fergus, Effect of cathode and electrolyte transport properties on chromium poisoning in solid oxide fuel cells, Int. J. Hydrogen Energ. 32(16) (2007) 3664-3671.

[74] G.V. Belov, V.S. Iorish, V.S. Yungman, IVTANTHERMO for Windows — database on thermodynamic properties and related software, Calphad 23(2) (1999) 173-180.

[75] H. Asteman, J.E. Svensson, L.G. Johansson, M. Norell, Indication of Chromium Oxide Hydroxide Evaporation During Oxidation of 304L at 873 K in the Presence of 10% Water Vapor, Oxid. Met. 52(1) (1999) 95-111.

[76] J.H. Hirschenhofer, D.B. Stauffer, R.R. Engleman, M.G. Klett, Fuel Cell Handbook Forth Edition, U.S. Department of Energy1998.

[77] C.K. Lin, T.T. Chen, Y.P. Chyou, L.K. Chiang, Thermal stress analysis of a planar SOFC stack, J. Power Sources 164(1) (2007) 238-251.

[78] R.D. Weir, T.W. De Loos, Measurement of the thermodynamic properties of multiple phases, Gulf Professional Publishing2005.

[79] D. Kulikov, S.P. Verevkin, A. Heintz, Enthalpies of vaporization of a series of aliphatic alcohols: Experimental results and values predicted by the ERAS-model, Fluid Phase Equilibria 192(1–2) (2001) 187-207.

[80] S.P. Verevkin, V.N. Emel'yanenko, Transpiration method: Vapor pressures and enthalpies of vaporization of some low-boiling esters, Fluid Phase Equilibria 266(1–2) (2008) 64-75.

[81] M. Stanislowski, U. Seeling, D.-H. Peck, S.-K. Woo, L. Singheiser, K. Hilpert, Vaporization study of doped lanthanum gallates and Ga_2O_3(s) in H_2/H_2O atmospheres by the transpiration method, Solid State Ion. 176(35–36) (2005) 2523-2533.

[82] S.R.J. Saunders, M. Monteiro, F. Rizzo, The oxidation behaviour of metals and alloys at high temperatures in atmospheres containing water vapour: A review, Progress in Materials Science 53(5) (2008) 775-837.

[83] A. Vesel, M. Mozetič, A. Zalar, Oxidation of AISI 304L stainless steel surface with atomic oxygen, Appl. Surf. Sci. 200(1) (2002) 94-103.

[84] X. Deng, P. Wei, M.R. Bateni, A. Petric, Cobalt plating of high temperature stainless steel interconnects, J. Power Sources 160(2) (2006) 1225-1229.

[85] X. Chen, P.Y. Hou, C.P. Jacobson, S.J. Visco, L.C. De Jonghe, Protective coating on stainless steel interconnect for SOFCs: oxidation kinetics and electrical properties, Solid State Ion. 176(5–6) (2005) 425-433.

[86] Y. Larring, T. Norby, Spinel and Perovskite Functional Layers Between Plansee Metallic Interconnect (Cr-5 wt % Fe-1 wt % Y_2O_3) and Ceramic $(La_{0.85}Sr_{0.15})_{0.91}MnO_3$ Cathode Materials for Solid Oxide Fuel Cells, J. Electrochem. Soc. 147(9) (2000) 3251-3256.

[87] J.H. Park, K. Natesan, Electronic transport in thermally grown Cr_2O_3, Oxid. Met. 33(1) (1990) 31-54.

[88] A. Holt, P. Kofstad, Electrical conductivity and defect structure of Cr_2O_3. I. High temperatures (>~1000°C), Solid State Ion. 69(2) (1994) 127-136.

[89] J.S. Park, H.G. Kim, Electrical Conductivity and Defect Models of MgO-Doped Cr_2O_3, J. Am. Ceram. Soc 71(3) (1988) 173-176.

[90] H. Nagai, T. Fujikawa, K.-i. Shoji, Electrical Conductivity of Cr_2O_3 doped with La_2O_3, Y_2O_3 and NiO, Transactions of the Japan Institute of Metals 24(8) (1983) 581-588.

[91] A. Holt, P. Kofstad, Electrical conductivity and defect structure of Cr_2O_3. II. Reduced temperatures (<~1000°C), Solid State Ion. 69(2) (1994) 137-143.

[92] Z. Lu, J. Zhu, E. Andrew Payzant, M.P. Paranthaman, Electrical Conductivity of the Manganese Chromite Spinel Solid Solution, J. Am. Ceram. Soc 88(4) (2005) 1050-1053.

[93] P. Huczkowski, N. Christiansen, V. Shemet, L. Niewolak, J. Piron-Abellan, L. Singheiser, W.J. Quadakkers, Growth Mechanisms and Electrical Conductivity of Oxide Scales on Ferritic Steels Proposed as Interconnect Materials for SOFC's, Fuel Cells 6(2) (2006) 93-99.

[94] L.V. Azároff, Role of Crystal Structure in Diffusion. I. Diffusion Paths in Closest-Packed Crystals, J. Appl. Phys. 32(9) (1961) 1658-1662.

[95] M. Martin, Diffusion in Oxides, in: P. Heitjans, J. Kärger (Eds.), Diffusion in Condensed Matter, Springer Berlin Heidelberg2005, pp. 209-247.

[96] R. Sun, Diffusion of Cobalt and Chromium in Chromite Spinel, J. Chem. Phys. 28(2) (1958) 290-293.

[97] R. Trebbels, T. Markus, L. Singheiser, Investigation of Chromium Vaporization from Interconnector Steels with Spinel Coatings, J. Electrochem. Soc. 157(4) (2010) B490-B495.

[98] S.-C. Kwak, B.K. Kim, D.-I. Kim, Y.W. Cho, Pulsed Electrodeposition of Thin Cobalt Coating Layer on Ferritic Stainless Steel for SOFC Interconnects, Korean J. Met. Mater. 55(11) (2017) 768-776.

[99] E. Konysheva, H. Penkalla, E. Wessel, J. Mertens, U. Seeling, L. Singheiser, K. Hilpert, Chromium Poisoning of Perovskite Cathodes by the ODS Alloy $Cr_5Fe_1Y_2O_3$ and the High Chromium Ferritic Steel Crofer22APU, J. Electrochem. Soc. 153(4) (2006) A765-A773.

[100] J.H. Kim, D.I. Kim, J.H. Shim, K.W. Yi, Investigation into the high temperature oxidation of Cu-bearing austenitic stainless steel using simultaneous electron backscatter diffraction-energy dispersive spectroscopy analysis, Corros. Sci. 77(0) (2013) 397-402.

[101] M. Abbasi, D.-I. Kim, H.-U. Guim, M. Hosseini, H. Danesh-Manesh, M. Abbasi, Application of Transmitted Kikuchi Diffraction in Studying Nano-oxide and Ultrafine Metallic Grains, ACS Nano 9(11) (2015) 10991-11002.

[102] C.W. Bale, P. Chartrand, S.A. Degterov, G. Eriksson, K. Hack, R. Ben Mahfoud, J. Melançon, A.D. Pelton, S. Petersen, FactSage thermochemical software and databases, Calphad 26(2) (2002) 189-228.

[103] C.W. Bale, E. Bélisle, P. Chartrand, S.A. Decterov, G. Eriksson, K. Hack, I.H. Jung, Y.B. Kang, J. Melançon, A.D. Pelton, C. Robelin, S. Petersen, FactSage thermochemical software and databases - recent developments, Calphad 33(2) (2009) 295-311.

[104] T. Salge, R. Neumann, A. C., M. Patzschke, Advanced mineral classification using Feature analysis and spectrum imaging with EDS, in: I.B. Celik, M.G. Kilic (Eds.) 23rd International Mining Congress and Exhibition of Turkey, Antalya, Turkey, 2013, pp. 357-367.

[105] D.G. Brandon, The structure of high-angle grain boundaries, Acta Metall. 14(11) (1966) 1479-1484.

[106] C. Herzig, Y. Mishin, Grain Boundary Diffusion in Metals, in: P. Heitjans, J.

Kärger (Eds.), Diffusion in Condensed Matter, Springer Berlin Heidelberg2005, pp. 337-366.

[107] C. Thorning, S. Sridhar, Grain boundary ridge formation during initial high temperature oxidation of Mn/Al TRIP steel, Philos. Mag. 87(23) (2007) 3479-3499.

[108] S.C. Tsai, A.M. Huntz, C. Dolin, Diffusion of ^{18}O in massive Cr_2O_3 and in Cr_2O_3 scales at 900°C and its relation to the oxidation kinetics of chromia forming alloys, Oxid. Met. 43(5) (1995) 581-596.

[109] S.C. Tsai, A.M. Huntz, C. Dolin, Growth mechanism of Cr_2O_3 scales: oxygen and chromium diffusion, oxidation kinetics and effect of yttrium, Mater. Sci. Eng. A 212(1) (1996) 6-13.

[110] A.C.S. Sabioni, A.M. Huntz, L.C. Borges, F. Jomard, First study of manganese diffusion in Cr_2O_3 polycrystals and thin films by SIMS, Philos. Mag. 87(12) (2007) 1921-1937.

[111] G.W. Jolanta, D. Joanna, Ż. Zbigniew, H. Marta, L. Jerzy, W. Marcin, Diffusion of chromium, manganese, and iron in $MnCr_2O_4$ spinel, J. Phase Equilib. Diff. 26(5) (2005) 561-564.

[112] I. Saeki, H. Konno, R. Furuichi, Initial oxidation of type 430 stainless steels with 0.09–0.9 Mn in O2-N2 atmosphere at 1273 K, Corros. Sci. 38(9) (1996) 1595-1612.

[113] I. Saeki, H. Konno, R. Furuichi, T. Nakamura, K. Mabuchi, M. Itoh, The effect of the oxidation atmosphere on the initial oxidation of type 430 stainless steel at 1273 K, Corros. Sci. 40(2) (1998) 191-200.

[114] C. Leung, M. Weinert, P.B. Allen, R.M. Wentzcovitch, First-principles study of titanium oxides, Physical Review B 54(11) (1996) 7857-7864.

[115] D. Watanabe, J.R. Castles, A. Jostsons, A.S. Malin, The ordered structure of TiO, Acta Crystallographica 23(2) (1967) 307-313.

[116] G. Lu, S.L. Bernasek, J. Schwartz, Oxidation of a polycrystalline titanium surface by oxygen and water, Surf. Sci. 458(1) (2000) 80-90.

[117] S.J. Laney, Ph.D Thesis, Modifying ferritic stainless steels for solid oxide fuel

cell applications, University of Pittsburgh, (2007).

[118] D.R. Lide, CRC Handbook of Chemistry and Physics, 84th Edition, Taylor & Francis2003.

[119] G.C. Allen, K.R. Hallam, J.A. Jutson, X-ray diffraction studies of solid solutions of Cr-, Mn-, Fe-, Co-, and Ni-containing transition metal spinel oxides, Powder Diffr. 10(03) (1995) 214-220.

[120] A.N. Hansson, S. Linderoth, M. Mogensen, M.A.J. Somers, X-ray diffraction investigation of phase stability in the Co–Cr–O and the Fe–Co–Cr–O systems in air at 1323K, J. Alloy. Compd. 402(1–2) (2005) 194-200.

[121] H. Bordeneuve, S. Guillemet-Fritsch, A. Rousset, S. Schuurman, V. Poulain, Structure and electrical properties of single-phase cobalt manganese oxide spinels $Mn_{3-x}Co_xO_4$ sintered classically and by spark plasma sintering (SPS), J. Solid State Chem. 182(2) (2009) 396-401.

[122] P.L. Meena, R. Kumar, K. Sreenivas, Rietveld refinement and FTIR analysis of bulk ceramic $Co_{3-x}Mn_xO_4$ compositions, AIP Conf. Proc. 1512(1) (2013) 1204-1205.

[123] E. Aukrust, A. Muan, Phase Relations in the System Cobalt Oxide–Manganese Oxide in Air, J. Am. Ceram. Soc 46(10) (1963) 511-511.

[124] E. Aukrust, A. Muan, Thermodynamic properties of solid solutions with spinel-type structure. I, The system Co_3O_4-Mn_3O_4, Trans. Metall. Soc. AIME 230 (1964) 378-382.

[125] I. Aoki, Tetragonal Distortion of the Oxide Spinels Containing Cobalt and Manganese, J. Phys. Soc. Jpn. 17(1) (1962) 53-61.

[126] Y.V. Golikov, S.Y. Tubin, V.P. Barkhatov, V.F. Balakirev, Phase diagrams of the Co-Mn-O system in air, J. Phys. Chem. Solids 46(5) (1985) 539-544.

[127] P.L. Meena, R. Kumar, K. Sreenivas, Rietveld Refinement and Spectroscopic Analysis of $Co_{3-x}Mn_xO_4$ ($0.1<x<1.0$) Ceramic Compositions, Int. J. Phys. Chem. Math. Sci. 3(1) (2014) 7-17.

[128] D.G. Wickham, W.J. Croft, Crystallographic and magnetic properties of

several spinels containing trivalent ja-1044 manganese, J. Phys. Chem. Solids 7(4) (1958) 351-360.

[129] Z.Y. Tian, P.H. Tchoua Ngamou, V. Vannier, K. Kohse-Höinghaus, N. Bahlawane, Catalytic oxidation of VOCs over mixed Co-Mn oxides, Appl. Catal., B 117–118 (2012) 125-134.

[130] H.S.C. O'Neill, The influence of next nearest neighbours on cation radii in spinels: the example of the Co_3O_4–$CoCr_2O_4$ solid solution, Mineral. Mag. 67(3) (2003) 547-554.

[131] T.A.S. Ferreira, J.C. Waerenborgh, M.H.R.M. Mendonça, M.R. Nunes, F.M. Costa, Structural and morphological characterization of $FeCo_2O_4$ and $CoFe_2O_4$ spinels prepared by a coprecipitation method, Solid State Sci. 5(2) (2003) 383-392.

[132] R.K. Wild, High temperature oxidation of austenitic stainless steel in low oxygen pressure, Corros. Sci. 17(2) (1977) 87-104.

[133] R.E. Lobnig, H.P. Schmidt, K. Hennesen, H.J. Grabke, Diffusion of cations in chromia layers grown on iron-base alloys, Oxid. Met. 37(1-2) (1992) 81-93.

[134] A.C.S. Sabioni, A.M. Huntz, J. Philibert, B. Lesage, C. Monty, Relation between the oxidation growth rate of chromia scales and self-diffusion in Cr_2O_3, J. Mater. Sci. 27(17) (1992) 4782-4790.

[135] M.G.C. Cox, B. McEnaney, V.D. Scott, A chemical diffusion model for partitioning of transition elements in oxide scales on alloys, Philos. Mag. 26(4) (1972) 839-851.

[136] J.D. Dunitz, L.E. Orgel, Electronic properties of transition-metal oxides-II: Cation distribution amongst octahedral and tetrahedral sites, J. Phys. Chem. Solids 3(3–4) (1957) 318-323.

[137] D.S. McClure, The distribution of transition metal cations in spinels, J. Phys. Chem. Solids 3(3–4) (1957) 311-317.

[138] A. Miller, Distribution of Cations in Spinels, J. Appl. Phys. 30(4) (1959) S24-S25.

[139] A. Navrotsky, O.J. Kleppa, The thermodynamics of cation distributions in

simple spinels, J. Inorg. Nucl. Chem. 29(11) (1967) 2701-2714.

[140] Y. Li, M.S. Wu, C.Y. Ouyang, The structural and electronic properties of spinel $MnCo_2O_4$ bulk and low-index surfaces: From first principles studies, Appl. Surf. Sci. 349(0) (2015) 510-515.

[141] H. Zhang, Z. Zhan, X. Liu, Electrophoretic deposition of $(Mn,Co)_3O_4$ spinel coating for solid oxide fuel cell interconnects, J. Power Sources 196(19) (2011) 8041-8047.

[142] J.L. Gautier, E. Rios, M. Gracia, J.F. Marco, J.R. Gancedo, Characterisation by X-ray photoelectron spectroscopy of thin $MnxCo_{3-x}O_4(1\geq x\geq 0)$ spinel films prepared by low-temperature spray pyrolysis, Thin Solid Films 311(1–2) (1997) 51-57.

[143] K. Kim, J. Heo, Electronic structure and optical properties of inverse-spinel $MnCo_2O_4$ thin films, J. Korean Phys. Soc. 60(9) (2012) 1376-1380.

[144] S.A. Hosseini, M.C. Alvarez-Galvan, J.L.G. Fierro, A. Niaei, D. Salari, MCr_2O_4 (M=Co, Cu, and Zn) nanospinels for 2-propanol combustion: Correlation of structural properties with catalytic performance and stability, Ceram. Int. 39(8) (2013) 9253-9261.

[145] X. Liu, M. Kareev, Y. Cao, J. Liu, S. Middey, D. Meyers, J.W. Freeland, J. Chakhalian, Electronic and magnetic properties of (1 1 1)-oriented $CoCr_2O_4$ epitaxial thin film, Appl. Phys. Lett. 105(4) (2014) 042401.

[146] D. Gaskell, An introduction to transport phenomena in materials engineering, Macmillan, New York, 1992.

[147] R.A. Svehla, Estimated viscosities and thermal conductivities of gases at high temperatures, Other Information: Orig. Receipt Date: 31-DEC-62, 1962, p. Medium: X; Size: Pages: 141.

[148] T. Nagasaka, R.J. Fruehan, Kinetics of the reaction of H_2O gas with liquid iron, Metall. Mater. Trans. B 25(2) (1994) 245-253.

[149] R.J. Fruehan, G.R. Belton, F.J. Mannion, Y. Sasaki, Rate of decarburization of Fe-Csat melts by H_2O at 1523 and 1873 K, Metall. Trans. B 23(1) (1992) 45-51.

[150] E.J. Opila, Volatility of Common Protective Oxides in High-Temperature Water Vapor: Current Understanding and Unanswered Questions, Mater. Sci. Forum 461-464 (2004) 765-774.

[151] G.R. Holcomb, D.E. Alman, The effect of manganese additions on the reactive evaporation of chromium in Ni–Cr alloys, Scr. Mater. 54(10) (2006) 1821-1825.

[152] J.C. Fisher, Calculation of Diffusion Penetration Curves for Surface and Grain Boundary Diffusion, J. Appl. Phys. 22(1) (1951) 74-77.

[153] L.G. Harrison, Influence of dislocations on diffusion kinetics in solids with particular reference to the alkali halides, Trans. Faraday Soc. 57(0) (1961) 1191-1199.

[154] A. Kaczmarska, Z. Grzesik, S. Mrowec, On the Defect Structure and Transport Properties of Co_3O_4 Spinel Oxide, High. Temp. Mater. Proc 31(4-5) (2012) 371.

[155] T. Horita, H. Kishimoto, K. Yamaji, Y. Xiong, M.E. Brito, H. Yokokawa, Y. Baba, K. Ogasawara, H. Kameda, Y. Matsuzaki, S. Yamashita, N. Yasuda, T. Uehara, Diffusion of oxygen in the scales of Fe-Cr alloy interconnects and oxide coating layer for solid oxide fuel cells, Solid State Ion. 179(38) (2008) 2216-2221.

국문초록

연료전지는 기본적으로 수소를 포함한 연료 기체와 산소 또는 다른 산화재들의 전기화학적 반응을 통해 전기 에너지를 생성하는 친환경 에너지 생성 장치이다. 현재 고안된 다양한 종류의 연료 전지 중 고체산화물연료전지 (solid oxide fuel cell, SOFC) 는 700 ~ 1000 도 사이에서 가동되기 때문에 고온용 연료전지로 분류되고 있다.

친환경 고효율의 SOFC 가 상용화되기 위해서는 제조비용의 획기적인 절감 및 생산성이 확보되어야 한다. 현재 연료전지의 가동온도가 기존의 1000 도 부근에서 600~800 도 구간으로 낮춰지며 분리판용 소재로 사용되던 기존 세라믹 소재를 금속 소재로 대체할 수 있게 되었다. 기존의 세라믹 분리판은 SOFC 의 제조단가에 큰 부분을 차지하였기 때문에 이를 금속으로 대체한다는 것은 가격경쟁력 확보 차원에서 매우 의미 있는 일이며 이러한 요구에 부흥하기 위해 금속 분리판용 소재에 대한 연구가 활발히 진행되고 있다. 여러 금속 합금 중 Co, Ni, Fe 계 스테인리스강들이 후보재료로 선정되었는데 이 중 고 Cr 페라이트계 스테인리스강이 가격, 내산화성, 열팽창계수 등의 기술적 요구 특성을 고려하였을 때 적당한 분리판 재료인 것으로 알려져 있다.

SOFC 의 출력 향상을 위해선 SOFC 단전지를 연속적으로 연결하여 스택 (stack) 을 형성하게 된다. 이 때 각각의 단전지 사이에 물리적 차단막과 전기 연결체 역할을 하는 금속 분리판이 위치하게 된다. SOFC 는 앞서 언급한 것과 같이 고온에서 가동되기 때문에 분리판 소재의 고온 내산화성이 재료 선정 시 고려해야 할 가장 중요한 재료

물성이다. 따라서 Fe 계 스테인리스강의 내산화성 향상을 위해 23 wt. % 이상의 Cr 이 함유된 새로운 강종이 독일의 ThyssenKrupp 사에 의해 개발 및 상용화되었다. 하지만 고 Cr 을 함유하기 때문에 필연적으로 Cr 휘발이 일어나게 되는데 이는 SOFC 의 장기적 안정성 관점에서 필수적으로 해결되야 하는 과제이다. 따라서 본 연구에서 저자는 SOFC 분리판 소재용 고 Cr 페라이트계 스테인리스강의 내산화성 향상과 Cr 휘발 억제를 두 가지 방식을 이용해 시도하여 보았다.

우선 연구의 첫 번째 부분에서는 금속의 결정립 크기가 고온 산화 특성에 미치는 영향에 대해서 연구를 진행하였다. 내산화 특성 평가 및 비교를 위해서 2 mm 와 20 mm 두께를 가지는 두 종류의 고 Cr 페라이트계 스테인리스강 상용판재를 이용하였다. 내산화 특성 평가는 일반적 SOFC 가동온도인 800 도에서 진행하였으며 SOFC 양극 환경을 모사하기 위해 공기 + 2 % H_2O 의 기체를 지속적으로 주입하였다. 사용된 두 종류의 시료의 평균 결정립 크기는 각각 ~25 μm 와 ~500 μm 로 측정되었다. 내산화 특성 비교 결과 20 mm 판재가 약 30 % 감소된 무게 증가량을 나타냈다. 이러한 차이는 시료의 결정립 크기 차이에 영향을 받는 총 입계 길이의 차이에 의해 초래된 것으로 판단된다. 본 연구의 실험 조건 하에서 금속기질의 입계는 입계 산화가 활발하게 일어나는 우선적 반응 장소로 작용하게 된다. 기질의 입계부는 금속과 산소 원자의 확산 속도가 빠르기 때문에 상대적으로 기질의 입내 표면과 다른 산화 거동 양상을 띠게 된다. 기질의 입계에서 추가적 입계 산화가 일어나면서 입계 산화물을 감싸고 있는 기질의 변형이 일어나게 되고 이는 결과적으로 산등성이 (ridge) 형태의 표면 음각으로 나타나게 된다. 결과적으로 이러한 기질 입계의 추가적 산화가 앞서 언급된 30 %

의 무게 증가량 차이를 일으키는 주된 원인으로 작용한다. 첫 번째 연구의 주된 목적은 고 Cr 페라이트계 스테인리스강의 입계 산화가 직접적으로 산화 거동에 어떤 영향을 주는지 밝혀내는 것이다. 이외에도 미세조직 분석을 통해 생성된 산화물의 상 및 성분 분석을 수행하고 이를 기반으로 열역학적 관점에서 산화물의 생성에 따른 평형 산소 분압 변화를 예측하였다.

본 연구의 두 번째 부분에서는 Co 전기도금을 이용한 표면처리를 통해 Cr 휘발 제어를 시도하였다. SOFC 의 가동온도가 600 ~ 800 도 정도로 낮춰졌다고는 하지만 가동온도 내에서 형성되는 Cr 계 산화물은 전지 효율 및 구조적 안정성에 문제를 야기할 수 있는 기상 육가 Cr 의 주 반응원으로 작용한다. 따라서 본 연구에서는 펄스 전기도금을 이용해 표면에 육방정계의 Co 를 코팅한 후 이러한 표면 처리가 Cr 휘발에 어떤 영향을 줄 수 있는지 확인하여 보았다. 통기포화법을 통해 도금재와 비도금재의 시간에 따른 Cr 휘발량을 정량적으로 비교하였으며 평가 결과 표면 처리를 통해 Cr 휘발량을 약 10 배 정도 감소시킬 수 있는 것을 확인하였다. 이 후 다양한 미세조직 분석 방법을 이용하여 500 시간 실험 환경에 노출된 도금재에 생성된 산화막의 상분석 작업을 진행하였다. 분석 결과 AB_2O_4 구조를 가지는 스피넬 구조의 Co-Mn 산화막 (CMO) 이 생성된 것을 확인하였으며 이러한 CMO 생성이 Cr 휘발 반응에 필요한 산화막 내 Cr 의 이동을 효과적으로 억제한 것을 알 수 있었다. 이외에도 열역학적 측면에서 해석이 불가능한 도금재 Cr 휘발 초기의 휘발율 변화 현상의 원인을 규명하기 위해 미세조직 및 동역학 측면에서 고찰하여 보았다. 고찰 결과 실험 초기에 생성된 Co 스피넬 산화물 내에서 Cr 의 외부 확산이

산화물의 결정립계를 따라 가능하였으나 이 후 점차적인 Mn 의 확산에 따른 CMO 상변태 후 Cr 의 결정립계 확산이 크게 억제되게 되었다. 이러한 상변태 현상이 도금재 초기 Cr 휘발율 변화에 가장 크게 기여하는 것으로 판단되었다.

주요어 : 페라이트계 스테인리스강, 고체산화물연료전지, 금속분리판, Cr 휘발, 고온 산화, 결정립 크기 효과, 산화물 분석

학번 : 2012-30154